Copyright

by

Babak Fallahazad

2015

The Dissertation Committee for Babak Fallahazad certifies that this is the approved version of the following dissertation:

Dielectric-Graphene Integration and Electron Transport in Graphene Hybrid Structures

Committee:

Emanuel Tutuc, Supervisor

Sanjay K. Banerjee

Allan H. MacDonald

Leonard F. Register

Seth Bank

Dielectric-Graphene Integration and Electron Transport in Graphene Hybrid Structures

by

Babak Fallahazad, B.E.; M.S.

Dissertation

Presented to the Faculty of the Graduate School of

The University of Texas at Austin

in Partial Fulfillment

of the Requirements

for the Degree of

Doctor of Philosophy

The University of Texas at Austin

May, 2015

Dedication

To my mother, father, and wife for their endless love and support

Acknowledgements

First and foremost, I would like to express my sincere gratitude to my adviser, Prof. Emanuel Tutuc, for his continuous support to conduct research at the highest levels. I would also like to thank the other members of my dissertation committee Prof. Sanjay K. Banerjee, Prof. Leonard F. Register, Prof. Allan MacDonald, and Prof. Seth Bank for their support.

I was fortunate to work with a group of talented people at the University of Texas at Austin. I would like to thank Kayoung Lee, Seyoung Kim, Junghyo Nah, En-Shao Liu, and Davood Shahrjerdi for their extensive support and help both inside and outside the Microelectronics Research Center (MRC) cleanroom. I would like to thank Kyounghwan Kim, Stefano Larentis, Sangwoo Kang, Jiamin Xue, Micah Points, Christopher Corbet, David Dillen, Jaehyun Ahn, Domingo Ferrer, Yufeng Hao, and Luigi Colombo for their contribution to my research at various levels.

I would like to acknowledge the MRC administrative and technical staff, Christine Wood, Jean Toll, Joyce Kokes, Jackie Srnensky, Marylene Palard, Jesse James, Bill Ostler, Ricardo Garcia, Gerlinde Sehne, Darren Robbins, and James Hiltzfelder.

My life has been blessed with my wife who has been an endless source of love and encouragement. I am very thankful to her for her patience and support. Lastly, my deepest gratitude goes to my mother and father without whom I could not be where I am today. Their love and support propel me in every aspect of life.

Dielectric-Graphene Integration and Electron Transport in Graphene Hybrid Structures

Babak Fallahazad, Ph. D.

The University of Texas at Austin, 2015

Supervisor: Emanuel Tutuc

Dielectrics have been an integral part of the electron devices and will likely resume playing a significant role in the future of nanoelectronics. An important step in assessing graphene potential as an alternative channel material for future electron devices is to benchmark its transport characteristics when integrated with dielectrics. Using back-gated and dual gated graphene field-effect transistors with top high-k metal-oxide dielectric, we study the dielectric thickness dependence of the carrier mobility. We show the carrier mobility decreases after deposition of metal-oxide dielectrics by atomic layer deposition (ALD) thanks to the Coulomb scattering by charged point defects in the dielectric. We investigate a novel method for the ALD of metal-oxide dielectrics on graphene, using an ultrathin nucleation layer that enables the realization of graphene field-effect transistors with aggressively scaled gate dielectric thickness. We show the nucleation layer significantly affects the quality of the subsequently deposited dielectric. In the second section, we study the transport characteristics of double layer systems. We demonstrate heterostructures consisting of two rotationally aligned bilayer graphene with an ultra-thin hexagonal boron nitride dielectric in between fabricated using advanced layer-by-layer transfer as well as layer pickup techniques. We show that double bilayer graphene devices possess negative differential resistance and resonant tunneling in their

interlayer current-voltage characteristics in a wide range of temperatures. We show the resonant tunneling occurs either when the charge neutrality points of the two bilayer graphene are energetically aligned or when the lower conduction sub-band of one layer is aligned with the upper conduction sub-band of the opposite layer. Finally, we study the Raman spectra and the magneto-transport characteristics of A-B stacked and rotationally misaligned bilayer graphene deposited by chemical-vapor-deposition (CVD) on Cu. We show that the quantum Hall states (QHSs) sequence of the CVD grown A-B stacked bilayer graphene is consistent with that of natural bilayer graphene, while the sequence of the QHSs in the CVD grown rotationally misaligned bilayer graphene is a superposition of monolayer graphene QHSs. From the magnetotransport measurements in rotationally misaligned CVD-grown bilayer we determine the layer densities and the interlayer capacitance.

Table of Contents

List of Tables xi

List of Figures xii

CHAPTER 1: INTRODUCTION **1**

1.1 Electronic properties of graphene 3

1.1.1 Band structure 4

1.1.1.1 Monolayer graphene 4

1.1.1.2 Bilayer graphene 6

1.2 Transport characteristics 8

1.2.1 Boltzmann transport equation 9

1.2.2 Electrical conductivity 13

1.2.3 Relaxation time 14

1.2.4 Coupling constant 15

1.2.5 Long-range scattering 16

1.2.6 Screened short-range scattering 17

1.3 Raman Spectrum 18

1.3.1 Raman scattering..18

1.3.2 Raman signatures of monolayer and bilayer graphene 20

1.4 Two-dimensional electron gas in magnetic field 24

1.4.1 Quantum Hall effect in monolayer graphene............................25

1.4.2 Quantum Hall effect in bilayer graphene...................................26

1.5 Chapter organization 27

CHAPTER 2: GRAPHENE FIELD-EFFECT TRANSISTOR WITH METAL OXIDE TOP DIELECTRIC **28**

2.1 Introduction...29

2.2 Atomic layer deposition of metal-oxide dielectrics on graphene 33

2.3 Device fabrication..34

2.4 Dependence of the mobility on top metal-oxide dielectric thickness 37

2.4.1 Conductivity and carrier mobility 37

2.4.2 Temperature dependence 40
2.4.3 Origin of the fixed charge impurities..41
2.5 Scaling of the top metal-oxide dielectric 43
2.5.1 Top gate capacitance measurement 44
2.5.2 Graphene topography after nucleation layer deposition 44
2.5.3 Effect of nucleation layer on dielectric constant........................46
2.5.4 Al_2O_3 structure 48
2.6 Summary 52

CHAPTER 3: RESONANT TUNNELING IN DOUBLE BILAYER GRAPHENE HETEROSTRUCTURES 53

3.1 2D-2D resonant tunneling..53
3.1.1 2D-2D tunneling formalism..56
3.2 2D-2D tunneling in double bilayer graphene heterostructures 59
3.2.1 Van der Waals heterostructures 59
3.2.2 Realization of double bilayer graphene heterostructures 61
3.2.2.1 Fabrication: dry layer transfer method...........................61
3.2.2.2 Fabrication: layer pickup method 62
3.2.2.3 Rotational alignment...65
3.2.2.4 Tunnel junction uniformity 65
3.3 Electrical characterization..66
3.3.1 Layer resistivity measurement 66
3.3.2 Capacitances and chemical potential measurement...................67
3.3.3 Interlayer current-voltage characteristics..................................72
3.3.4 Thickness dependence of interlayer resistance and capacitance.74
3.3.5 Energy band alignment at resonant tunneling............................76
3.3.6 Carrier densities at resonant tunneling......................................78
3.3.7 Resonant tunneling at large interlayer bias 79
3.3.8 Temperature dependence 82
3.3.9 Transverse electric field across the individual bilayers 83
3.4 Broadening of the resonant tunneling peaks 85

3.4.1 Temperature dependence 88
3.4.2 Interlayer tunneling with an in-plane magnetic field 89
3.5 Summary 91

CHAPTER 4: QUANTUM HALL EFFECT IN BERNAL STACKED AND ROTATIONALLY MISALIGNED CVD BILAYER GRAPHENE **92**

4.1 Introduction 92
4.2 Realization of back-gated bilayer graphene field effect transistor 103
4.2.1 Chemical vapor deposition of bilayer graphene 103
4.2.2 Raman spectra 103
4.2.3 Device fabrication 105
4.3 Characterization 107
4.3.1 Conductivity measurement and carrier mobility.......................107
4.3.2 Quantum Hall effect in CVD-grown bilayer graphene 108
4.3.2.1 A-B stacked bilayer graphene 108
4.3.2.2 Rotationally misaligned bilayer graphene 111
4.4 Summary 116

APPENDIX: LIST OF PUBLICATIONS **117**

REFRENCES **119**

List of Tables

Table 3.1: List of the key devices presented in this chapter. 64

Table 3.2: Fitting parameter values obtained by fitting a polynomial of degree five to the μ vs. n data of Fig. 3.8. 70

List of Figures

Figure 1.1: Atomic structures of carbon allotropes (Figure adapted from Ref. [3]).2

Figure 1.2: Monolayer graphene lattice. Basis atomic sites A and B are marked by blue and red respectively. a_1 and a_2 are primitive lattice vectors, $a_0 = 1.42$ Å is the C-C bond length, and $a = 2.46$ Å is the lattice constant. 4

Figure 1.3: Energy-momentum dispersion of monolayer graphene (in units of γ_0) calculated using tight binding method with $\gamma_0 = 2.7$ eV. The magnified view of the energy bands shows the energy-momentum dispersion is linear close to the Dirac point (Figure and caption adapted from ref. [4]). 5

Figure 1.4: (a) schematic of the bilayer graphene lattice containing four carbon atoms in the unit cell: A, B, A, and B (atom B of the top bilayer is directly on top of the atom A of the bottom bilayer graphene). The coupling between the carbon atoms of the opposing layers are marked by dashed lines. (b) Energy-momentum dispersion of bilayer graphene close to the K point and in the presence of a finite layer asymmetry $u = \Delta$ (right panel adapted from Ref. [9]). 7

Figure 1.5: Graphene conductivity (σ) vs. gate voltage (Vg) measured in a back-gated graphene field effect transistor at $T = 10$ K. σ shows a linear dependence on Vg away from the charge neutrality point (Figure and caption adapted from Ref. [10]). 9

Figure 1.6 Rayleigh and Raman Scattering. (a) Stokes Raman scattering: an incident photon creates an electron-hole pair which subsequently decay into a phonon Ω and another electron-hole pair e-h'. A photon with frequency ωsc is emitted when the secondary electron-hole recombine (b) Anti-Stokes Raman scattering: similar to the Stokes except that the phonon is absorbed by the electron-hole pair. (c) Comparison of the Rayleigh and Raman scatterings. 19
Figure 1.7: (a) The first Brillion zone of monolayer graphene with $\Gamma, \mathrm{K}, \mathrm{K}'$, and M points marked. (b) monolayer graphene phonon dispersion calculated by DFT (Figure and caption adapted from Refs. [23], [24]). 21
Figure 1.8: Raman spectra of graphene, bilayer graphene, and graphite measured using a green laser ($\lambda = 532$ nm). The signature G (~ 1580 cm^{-1}) and 2D (~ 2700 cm^{-1}) peaks are mark. 22
Figure 1.9: Raman processes in (a) monolayer graphene (b) bilayer graphene. Solid lines present energy-momentum dispersion, blue (red) arrows present intraband transitions by absorption (emission) of photons, dashed arrows present interband transitions accompanied by phonon emission/absorption, and dotted arrows present electrons scattered by defects. 23
Figure 1.10: Schematic illustration of (a) integer quantum Hall effect in a 2DEG with parabolic energy-momentum dispersion. (b) Landau levels of an ideal 2DEG (c) Landau levels of a disordered 2DEG (Left panel adapted from Ref. [25])..25

Figure 1.11: Schematic illustration of integer quantum Hall effect in (a) monolayer graphene with conductivity plateaus at $\nu = \pm 4M + 12$ (b) bilayer graphene with conductivity plateaus at $\nu = \pm 4M + 1$ (Figure adapted from Ref. [25]). 27

Figure 2.1: Temperature dependence of mobility in graphene and graphite on SiO_2/Si substrate. The experimental mobility values are measured at carrier density $n = 1 \times 10^{12}$ cm^{-2}. Three scattering mechanisms limiting mobility in graphene: scattering by LA phonons (dark red solid line), remote interfacial phonon scattering (green dashed line), and impurity scattering (red and blue dashed lines). The calculated net mobility values for two samples are marked by red and blue solid lines (Figure and caption adapted from Ref. [33]).. 30

Figure 2.2: Mobility vs. number of ice layers deposited on top of a back-gated graphene FET measured at 77 K. ≅ 30% mobility increase observed after ice deposition (Figure adapted from Ref. [34]). 32

Figure 2.3: Schematic view of (a) device type 1: a back-gated graphene FET with a 285-nm thick SiO_2 bottom dielectric, and a top dielectric stack consisting of an oxidized Al layer and ALD HfO_2 (b) device type 2: dual-gated graphene FET with a top dielectric stack consisting of an oxidized Al or Ti layer and ALD Al_2O_3. 34

Figure 2.4: Optical micrographs of (a) natural graphite flakes (b) natural graphite flakes on polyethylene tape (c) 285 nm-thick thermally grown SiO_2 on Si substrate with Pt/Cr alignment marks 200 μm apart and ready for graphene exfoliation (d) as exfoliated monolayer and multilayer graphene on SiO_2/Si substrate (e) a back-gated graphene FET (f) a dual-gated graphene FET. The contacts (top gates) are marked in light (dark) color. The scale bar in panels (a) and (b) are the same and defined by the width of the tape which is 1 inch. 36

Figure 2.5: σ vs. VBG, determined using four-point measurements, for different top dielectric stack thicknesses (t_{stack}). V_{BG} values of x-axis are offset by the charge neutrality voltage ($V_{BG\text{-}CNP}$), at which the graphene conductivity is minimum. 37

Figure 2.6: μ vs. t_{stack} for four monolayer and one bilayer graphene samples measured at room temperature. The mobility decreases steeply after the first 2-4 nm of oxide deposition, and remains constant for thicker dielectric films. 38

Figure 2.7: (a) σ vs. V_{BG} measured at different temperatures (T) for a graphene device with a 11 nm HfO_2 top dielectric. The V_{BG} value is offset by the back gate voltage at the charge neutrality point ($V_{BG\text{-}CNP}$) (b) μ vs. T for the same device. The relatively weak T-dependence suggests that phonons are not the mobility limiting factor in these devices.........................40

Figure 2.8: Band diagram schematic for a structure consisting of metal-oxide deposited on graphene. The oxygen vacancies, inherent for dielectrics deposited at low temperatures become ionized in the proximity of the interface, creating fixed charged impurities, which in turn reduce the mobility (Reproduced from Ref. [55]). (b) n_{imp} vs. t_{stack} data for four graphene monolayers. 41

Figure 2.9: R_{2pt} vs. V_{TG} measured in a dual-gated graphene FET at different VBG. The 2 nm-thick Al_2O_3 top dielectric was deposited by ALD using a 0.6 nm Ti nucleation layer. (b) $V_{TG\text{-}CNP}$ vs. V_{BG}, measured from the R_{2pt} vs. V_{TG} traces at different back-gate biases. The C_{BG}/C_{TG} ratio is equal to the slope of the fitted line. 43

Figure 2.10: Topography of graphene flakes after the nucleation layer deposition. The top (bottom) panel represents data for a graphene flake with a 1.5 nm thick Al (0.6 nm thick Ti) film. The measured surface roughness values are 0.52 nm for Al, and 0.24 nm for Ti nucleation layers. The smoother surface of the graphene with Ti film suggests that Ti covers the entire graphene surface at a lower thickness..45

Figure 2.11: (a) C_{TG} vs. $t_{Al_2O_3}$ for dual-gated graphene FETs with Ti and Al nucleation layers (b) C_{TG}^{-1} vs. $t_{Al_2O_3}$ of same devices. For both interfacial layers, C_{TG}^{-1} has a linear dependence on $t_{Al_2O_3}$ The *k* values for ALD Al_2O_3 deposited on Ti and Al nucleation layers are 12.7 and 5.5, respectively (c) Dual-gated graphene FET schematic, with the top gate capacitance consisting of interface capacitance (C_{int}) and Al_2O_3 capacitance ($C_{Al_2O_3}$), in series..47

Figure 2.12: μ vs. tstack for graphene FETs with the top ALD Al_2O_3 dielectric deposited on Ti. The shaded area represents the interfacial layer thickness. The dashed line is a guide to the eye. 48

Figure 2.13: Leakage current density (J) as a function of vertical electric field (E) for different top dielectric thicknesses. The gate resistance for devices with 2.6 nm top dielectric stack is ~1 MΩ. 50

Figure 2.14: TEM cross section micrographs of ALD Al_2O_3 on graphene, grown using Al (a), and Ti (b) nucleation layers. Panel (b) inset: Fast Fourier Transform corresponding to the grain marked by the dashed line. (c) Compositional maps of oxygen, carbon, titanium, and aluminum determined from EELS measurements on an Al_2O_3/TiO_x/graphene stack. (d) Concentration profiles of C (K-edge), Al (L-edge), O (K-edge), Si (L-edge), and Ti (L-edge) obtained from EELS line scans of Al_2O_3/TiO_x/graphene stack. 51

Figure 3.1: (a) Schematic of a dual-gated double quantum well tunneling transistor based on GaAs/AlGaAs heterostructure. The individual quantum wells are independently contacted. A sketch of the energy band diagram is shown at left. The energy-momentum dispersion of two layers when (b) energetically misaligned (c) energetically aligned with identical carrier density (d) energetically aligned with different carrier densities. (e) Interlayer current-voltage characteristics showing gate-tunable resonant tunneling and NDR (Figures and captions adapted from refs. [65], [66]). 55

Figure 3.2: Conduction band of two 2DEGs. μ_B (μ_T) is the chemical potential in bottom (top) layer and E_{B0} (E_{T0}) is the conduction band edge energy of bottom (top) layer. 57

Figure 3.3: G vs. Vint of a 2D-2D electron system measured at various temperatures in a sample with equal carrier densities in both top and bottom layers ($n = 1.6 \times 1011$ cm^{-2}). Insets show the energy band alignment at resonance and off resonance (Figure and caption adapted from Ref. [69])..59

Figure 3.4: (a) Schematic of the double bilayer graphene device. (b) Optical micrograph of the top and bottom graphene flakes illustrating the alignment of straight edges. The red (yellow) lines mark the boundaries of the bottom (top) bilayer graphene. (c) Optical micrograph of the device. The red (yellow) dashed lines mark the bottom (top) bilayer graphene. 60

Figure 3.5: Fabrication of back-gated double bilayer graphene heterostructure using dry transfer technique. (a) Transfer of bottom bilayer graphene onto bottom hBN. (b) Trimming of bottom bilayer in O_2 plasma using PMMA mask. (c) transfer of thin interlayer hBN flake. (d) Transfer of top bilayer graphene. (e) Trimming of top bilayer in O_2 plasma using PMMA mask. (f) Final device after definition of metal contacts. The black arrows in panels (a) and (d) point to the reference straight edges used for the alignment of the two layers. 63

Figure 3.6: Device #1 bottom [panel (a)] and top [panel (b)] bilayer graphene resistivity contour plots measured as a function of V_{BG} and V_{TL} at T = 1.4 K. The charge neutrality points in both panels are marked by black dashed lines. 67

Figure 3.7: Capacitance and chemical potential measurement in device #1 (a) Contour plot of ρ_T measured as a function of V_{BG} and V_{TL}, at B = 13 T and T = 1.5 K in Device #1. The bottom bilayer graphene LL filling factors are marked. (b) V_{BG}-V_{TL} vs. ν of the bottom bilayer showing a linear dependence; the C_{BG} value is determined from the slope. 71

Figure 3.8: μ_B vs. n_B for Devices #1 and #4. The dashed line is the polynomial fit to the experimental data. 72

Figure 3.9: Interlayer current-voltage characteristics and resonant tunneling. I_{int} vs. V_{TL} of (a) Device #1 measured at T = 10 K, and (b) Device #2 measured at room temperature. (c) Device #3 measured at room temperature. The right axes show the interlayer current normalized by the active area.73

Figure 3.10: (a) Normalized interlayer resistance vs. number of hBN layers measured in multiple devices and at a low temperature of T = 1.4 – 20 K and at room temperature. (b) C_{int} vs. number of hBN layers. (c) $R_c \times C_{int}$ (delay time) vs. number of hBN layers. The dashed lines in panels (a) and (b) are guides to the eye. 74

Figure 3.11: Energy band diagram of the double bilayer graphene device when charge neutrality points of top and bottom bilayers are aligned..................77

Figure 3.12: V_{TL} vs. V_{BG} of Devices #1 and #2 at tunneling resonance (circles) and when charge neutrality points are aligned (solid line) 78

Figure 3.13: n_T vs. n_B of Devices #1 and #2 at tunneling resonance...................79

Figure 3.14: (a) I_{int} vs. V_{TL} of Devices #2 measured at room temperature, and at V_{BG} = -40, 0, 40 V. In addition to the resonant tunneling centered around V_{TL} = 0 V, there are two additional sets of resonant tunneling occurr at V_{TL} = 0.5 - 0.6 V. (b) dI_{int}/dV_{TL} vs. V_{ES} corresponding to the data of panel (a) measured at room temperature, and at V_{BG} = -40, 0, 40 V. (c-e) The schematic presentation of the energy band alignment in double bilayer graphene at (a) V_{ES} = - 0.4 V (b) V_{ES} = 0 V (c) V_{ES} = 0.4 V. In panels (c) and (e) the lower conduction band of one bilayer is aligned with the upper conduction band of the opposite bilayer. In panel (b), the charge neutrality points of the two bilayers are aligned (Figure and caption adopted from ref. [91])...81
Figure 3.15: I_{int} vs. V_{TL} of device #2 measured at V_{BG} = -40, 0, 40 V and at temperatures ranging between T = 1.5 K and room temperature. The temperature dependence of the background tunneling current is relatively weak. 82
Figure 3.16: (a) Device #1 ρ_B contour plot vs. V_{BG} and V_{TL}, measured at T = 1.4 K. The CNL of the top bilayer graphene is added to mark the DNP. E_T and E_B in (b) Device #1, and (c) Device #2, calculated at the tunneling resonance...85
Figure 3.17: Energy band diagram of rotationally misaligned bilayers. (a) Brillouin zone boundaries of two hexagonal lattices rotationally misaligned by θ° in real space. K_B (K_T) is the valley minimum the bottom (top) bilayer graphene. (b) A rotational misalignment by a small angle θ translates into valley separation in momentum space by $\Delta k \cong K\theta$.................86

Figure 3.18: (a) I_{int}/V_{TL} vs. V_{ES} for Device #2 at V_{BG} = 40 V and at T = 297 K (solid line), along with a Lorentzian fit to the experimental data (dashed line). (b) Temperature dependence of Γ measured in Device #2 and at V_{BG} = -40, -20, 20, 40 V. (Right panel adapted from Ref. [91]) 88

Figure 3.19: I_{int} vs. V_{TL} of Device #2 measured at in-plane magnetic fields $B_{||}$ = 0, 14 T and at (a) V_{BG} = -40 V and (b) V_{BG} = -40 V. 90

Figure 4.1: Lattice structure of rotationally misaligned bilayer graphene at θ = 3.89°, with super-lattice primitive vectors T_1 and T_2. The points α, β, and γ correspond to A-B, B-A, and A-A stacked sites respectively. The unit cell of the super-lattice is marked with the yellow rhombus. The inset illustrates three hopping processes in the interlayer Hamiltonian (Figure and caption adapted from Ref. [94]). 94

Figure 4.2: Brillouin zones of the fixed and rotated monolayer graphene, as well as the Brillouin zone of the commensurate, rotationally misaligned bilayer graphene for θ = 13.17°. In this Figure A_1 and A_2 are the reciprocal lattice vectors of the fixed layer, $A_1^{'}$ and $A_2^{'}$ the reciprocal lattice vectors of the rotated layer, and G_1, G_2 the reciprocal lattice vectors of the super-lattice (Figure and caption adapted from ref. [94]). 95

Figure 4.3: (a) The first Brillion zone of rotationally misaligned bilayer centered midpoint between the charge neutrality points of the two monolayers (marked with ⊗). G_1 and G_2 are the reciprocal lattice vectors of the super-lattice. (b) Energy-momentum dispersion of rotationally misaligned bilayer graphene with rotational misalignment $\theta = 3.9°$ (c) Rotationally misaligned bilayer Fermi velocity normalized by monolayer Fermi velocity vs. θ calculated by continuum model. (d) Same as panel (b) but in the presence of a potential difference V = 0.3 V. The potential difference between two layers does not lead to band gap opening (Figures and caption adapted from Refs. [5], [6]). 97

Figure 4.4: (a) Raman spectra of rotationally misaligned bilayer graphene and monolayer graphene measured with a λ = 633 nm laser. (b) Energy bands of rotationally misaligned bilayer graphene. Van Hove singularities are induced by overlap of individual layer energy bands. (c) The energy dependence of rotationally misaligned bilayer graphene density of states (DOS) without (blue) and with (red) interlayer interactions. DOS exhibit distortions from the interlayer interactions showing Van Hove singularities [97]. 99

Figure 4.5: (a) Experimental (black symbols) and theoretically calculated (red symbol) rotationally misaligned bilayer graphene 2D band FWHM vs. rotational misalignment angle θ. The horizontal line represents the 2D band FWHM of monolayer graphene. The grey and red lines are guides to the eye. (b) Intervalley 2D Raman scattering processes for rotationally misaligned bilayer graphene in which the laser excitation energy is smaller (blue lines) or larger (black lines) than the energy difference between conduction and valence Van Hove singularities (Figure and caption adapted from Ref. [97])...101

Figure 4.6: Optical micrograph of a CVD-grown multi-layer graphene sample after transfer onto a 285-nm thick SiO_2 on Si substrate. Monolayer, bilayer, and trilayer regions are marked..102

Figure 4.7: (a) 2D band FWHM spatial map reveals the bilayer is a mixture of domains with either wide (45 - 54 cm^{-1}) or narrow (27 – 33 cm^{-1}) 2D band. Dashed lines mark the boundaries of the bilayer domains and the dotted line marks a Hall bar subsequently fabricated to probe electron transport in individual bilayer regions. (b) Raman spectra acquired at three different positions, as marked in panel (a) show the G (≃ 1580 cm^{-1}) and 2D (≃ 2700 cm^{-1}) bands. (c) Histogram of the 2D band FWHM on a bilayer domain with wide 2D band. The average 2D FWHM is 53 ± 2 cm-1. (d) Example of a 2D band spectrum (black line) acquired on a A-B stacked bilayer domain. A fit (red) using four Lorentzian functions (green) provide a very good match to the experimental data..........106

Figure 4.8: (a) Optical micrograph of a back-gated Hall bar fabricated on bilayer graphene. An example of conductivity vs. V_{BG} of (b) A-B stacked bilayer (c) rotationally misaligned bilayer graphene measured at room temperature. 107

Figure 4.9: (a) ρ_{xx} and ρ_{xy} vs. V_{BG}, measured at $B = 25$ T, and $T = 0.3$ K. The data shows QHSs, marked by vanishing ρxx and quantized ρxy at filling factors $\nu = \pm 4$ and $\nu = -8$. (b) ρxx vs. ν measured at $T = 0.3$ K, and at different B-field values, illustrating the emergence of QHSs at integer filling factors multiple of four with increasing the B-field. 109

Figure 4.10: (a) ρ_{xx} vs. V_{BG} measured at different temperatures, and at $B = 25$ T. Inset: ρ_{xx} vs. T^{-1} at $\nu = -4$ on a log-lin scale, measured at $B = 15$ T (□), 20 T (○), 25 T (▽), 30 T (◇). (b) Δ vs. B, for $\nu = -4$ and $\nu = -8$ QHSs. The solid lines are guide to the eye. 110

Figure 4.11: (a) ρ_{xx} and ρ_{xy} vs. B measured at $n = -9.7 \times 10^{12}$ cm^{-2} and at $T = 0.3$ K. The SdH oscillations stem from a QHSs superposition of the two decoupled graphene monolayers. (b) Fourier transform of ρ_{xx} vs. B^{-1} data. The two peaks represent the layer densities, up to a factor 4e/h. (c) Top layer, bottom layer, and total carrier densities of the rotationally misaligned bilayer graphene vs. V_{BG}. The symbols (lines) represent experimental data (calculations). 112

Figure 4.12: (a) rotationally misaligned bilayer ρxx contour plot as a function of V_{BG} and B. The red (black) lines are the calculated position of $\nu = \pm 0, 4, 8, 12$ ... LLs of the top (bottom) layer. The layer filling factors $\nu T, \nu B$ are indicated for each QHS (b) Landau level fan diagram of the top (blue), and bottom (red) graphene layers as a function of *B*. The black line shows the chemical potential of the bilayer device at V_{BG}-$V_{BG\text{-}CNP} =$ -50 V. Each step in the chemical potential marks a quantum Hall state. 115

CHAPTER 1: INTRODUCTION

Monolayer graphene, a single layer of carbon atoms arranged in a honeycomb lattice, was first experimentally isolated from graphite in 2004 by Andrew Geim and Konstantin Novoselov [1] decades after it was theoretically predicted to be physically unstable in its free standing form [2]. Soon after its isolation, graphene attracted attention within scientific community for its interesting characteristics that set it apart from other two-dimensional (2D) electron systems. First, monolayer graphene is the first truly two-dimensional electron gas (2DEG) compared to the other conventional 2DEGs with parabolic energy-momentum dispersion formed at the interface of heterostructures (e.g. GaAa-based heterostructures); and second, monolayer graphene possesses superior transport characteristics such as high carrier mobility even at the room temperature ($\cong 10{,}000\ cm^2/V \cdot s$) which makes it promising for device applications.

Bilayer graphene, consisting of two graphene monolayers stacked on top of each other, has also unique electronic properties that makes it equally interesting. Besides high carrier mobility, bilayer graphene possesses a tunable band gap and energy-momentum dispersion that can be controlled by applying a transverse electric field (E-field). In this dissertation, we study various topics related to the electronic properties of both monolayer and bilayer graphene. To familiarize readers with the concepts that are often discussed in the upcoming chapters, we review the basic physical properties and characteristics of monolayer and bilayer graphene in this chapter. We first discuss the

energy band structure of monolayer and bilayer graphene and briefly go over the band structure calculation using the tight binding method. Then we discuss the carrier transport properties of monolayer graphene using the semi-classical Drude-Boltmann formalism. We show the effect of the long-range and screened short-range scatterers on the carrier transport in monolayer graphene. We continue with the Raman spectra of monolayer and bilayer graphene as well as graphite and discuss Raman spectroscopy as a powerful non-destructive method to determine various quantities associated with graphene such as the number of layers, edge orientation, doping, etc. Finally, we review the basic magnetotransport properties of monolayer and bilayer graphene and compare the quantum Hall effect (QHE) in monolayer and bilayer graphene with that of a conventional 2DEG with parabolic energy-momentum dispersion.

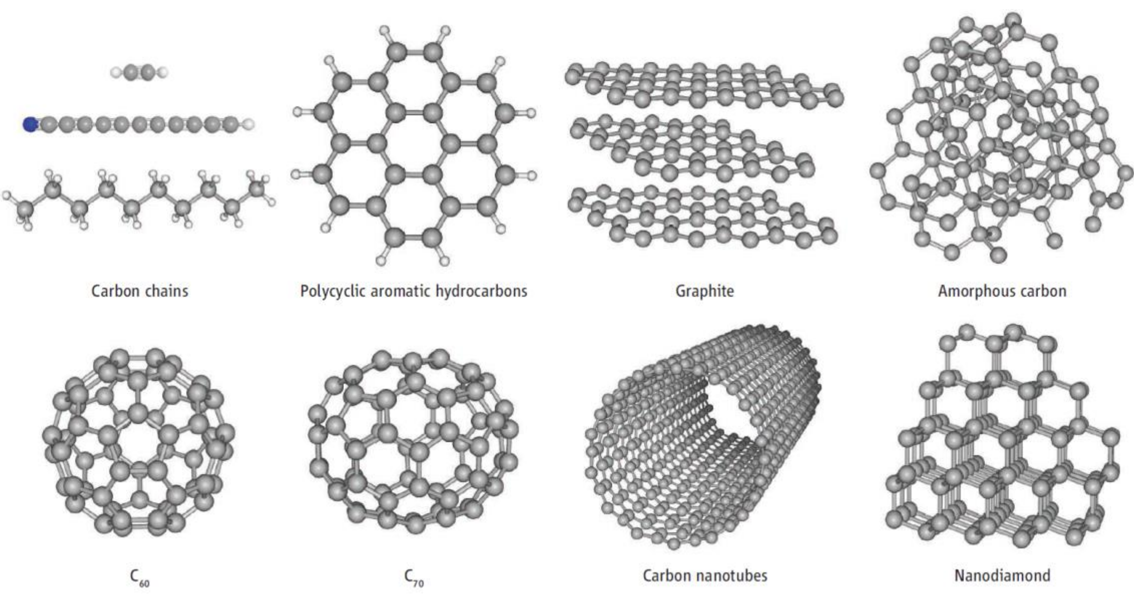

Figure 1.1: Atomic structures of carbon allotropes (Figure adapted from Ref. [3]).

1.1 ELECTRONIC PROPERTIES OF GRAPHENE

The electron configuration of carbon atom is $1s^2 2s^2 2p^2$. Carbon naturally exists in variety of forms (allotropes) ranging from zero dimensional (0D) fullerene to three dimensional (3D) diamond. Figure 1.1 shows the atomic structure of a few carbon allotropes. One of the most common allotropes of carbon is graphite, a stack of atomically thin two-dimensional layers, known as monolayer graphene, bonded to each other by Van der Waals force. The carbon atoms in monolayer graphene form three sp^2 hybridized orbitals and one p_z orbital orthogonal to the graphene plane. Each carbon atom forms three σ bonds with the neighbor carbon atoms via sp^2 orbitals that are separated 120 degrees in x-y plane and form a hexagonal lattice structure (Fig. 1.2). The fourth electron, in the p_z orbital, contributes to the π bonding.

The hexagonal lattice of monolayer graphene can be considered as a Bravais lattice with two-atom basis. Although all carbon atoms in monolayer graphene are identical, they are often labeled as A and B to differentiate the two basis atoms. The lattice constant and the distance between the closest neighbor atoms in monolayer graphene are $a = 2.46$ Å and $a_0 = 1.42$ Å, respectively, and the primitive lattice vectors are:

$$a_1 = a\left(\frac{\sqrt{3}}{2}, \frac{1}{2}\right), a_2 = a\left(\frac{\sqrt{3}}{2}, -\frac{1}{2}\right)$$

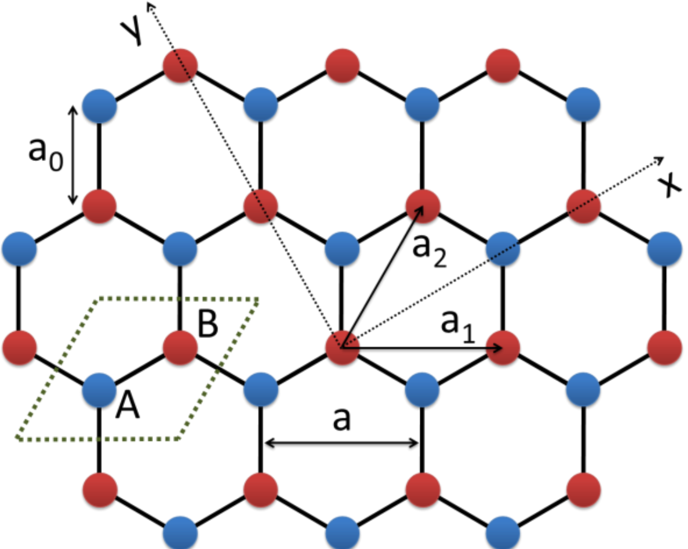

Figure 1.2: Monolayer graphene lattice. Basis atomic sites A and B are marked by blue and red respectively. a_1 and a_2 are primitive lattice vectors, $a_0 = 1.42$ Å is the C-C bond length, and $a = 2.46$ Å is the lattice constant.

1.1.1 Band structure

1.1.1.1 *Monolayer graphene*

Electrons of σ bond form deep fully occupied valence bands that do not contribute to the charge conduction, therefore the conduction in monolayer graphene occurs solely through the electrons of the π bond. The p_z orbitals that form π bond are only slightly perturbed by the neighboring atoms so the band structure of monolayer graphene can be calculated using the tight binding model. The energy-momentum dispersion of monolayer graphene calculated using tight binding method by considering interactions only with the nearest neighbors is:

$$E = \pm\gamma_0 \sqrt{1 + 4cos\left(\frac{\sqrt{3}a}{2}k_x\right)cos\left(\frac{a}{2}k_y\right) + 4cos^2\left(\frac{a}{2}k_y\right)} \qquad (1.1)$$

here γ_0 is the nearest neighbor hopping energy, and k_x and k_y are the momentum components. The energy band diagram of the monolayer graphene is shown in Fig. 1.3. Monolayer graphene has a hexagonal Brillion zone and the conduction and valence band cones, known as Dirac cones, meet at the corners of the first Brillion zone, namely K and K' points. The low-energy band of monolayer graphene can be described by $E = \pm\hbar v|\boldsymbol{k}|$, where $\hbar$ is the reduced Planck constant, $v_F = (\sqrt{3}/2)\, a\gamma_0/\hbar$ is the Fermi velocity, and $\boldsymbol{k}$ is the momentum referenced with respect to K or K' points.

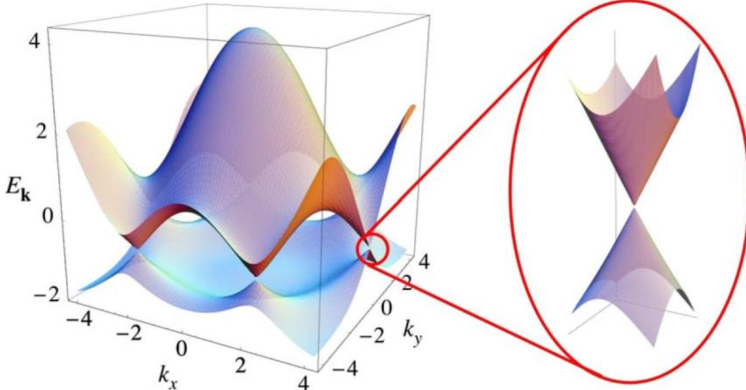

Figure 1.3: Energy-momentum dispersion of monolayer graphene (in units of $\boldsymbol{\gamma_0}$) calculated using tight binding method with $\gamma_0 = 2.7$ eV. The magnified view of the energy bands shows the energy-momentum dispersion is linear close to the Dirac point (Figure and caption adapted from ref. [4]).

1.1.1.2 *Bilayer graphene*

Bilayer graphene is a close relative of monolayer graphene and consists of two graphene monolayers stacked on top of each other. The electronic properties of bilayer graphene strongly depend on the relative alignment of the two graphene monolayers. A-B (Bernal) stacked bilayer is the most common form of the bilayer graphene where atom A of one layer is aligned with the atom B of the opposite layer ($\tilde{B}$) [Fig. 1.4(a)]. Rotationally misaligned bilayer is the other form of the bilayer graphene where one graphene monolayer is rotated with respect to the other one; the electronic properties of rotationally misaligned bilayer graphene depend on the rotational angle and is usually similar to that of monolayer graphene due to the weak interlayer coupling [5]–[7]. For the convenience, in the rest of this dissertation the term “bilayer graphene” is exclusively used for the A-B stacked bilayer graphene unless otherwise stated. Even though monolayer and bilayer graphene share similar properties (e.g. excellent mechanical and chemical stability, high carrier mobility, etc.), there is one striking property that sets bilayer graphene apart from monolayer and that is the possession of a tunable band gap. The energy-momentum dispersion of the bilayer graphene calculated using the tight binding model at a zero magnetic field is [8]:

$$\varepsilon_\alpha^2 = \frac{\gamma_1^2}{2} + \frac{u^2}{2} + \left(v_F^2 + \frac{v_3^2}{2}\right) k^2 + (-1)^\alpha \sqrt{\Gamma} \tag{1.2}$$

$$\Gamma = \frac{1}{4}(\gamma_1^2 - v_3^2 k^2)^2 + (\gamma_1^2 + u^2 + v_3^2 k^2) v_F^2 k^2 + 2\xi \gamma_1 v_3 v_F^2 k^3 cos 3\varphi$$

$$v_3 = \left(\sqrt{3}/2\right) a \gamma_3 / \hbar$$

here, $\alpha = 1, 2$ correspond to the lower- and higher-energy bands in the four degenerate valleys of the bilayer graphene, $\gamma_1$is the interlayer coupling (between $\tilde{A}$ and B), u is the difference between the on-site energies in the two layers, γ_3 is the weak A - $\tilde{B}$ coupling, k is the magnitude of the momentum referenced with respect to K or K' points, and $\varphi = tan^{-1}(k_y/k_x)$ is a phase factor. Figure 1.4(b) illustrates the energy band diagram of the bilayer graphene calculated using the tight binding method assuming a finite layer asymmetry $u = \Delta$.

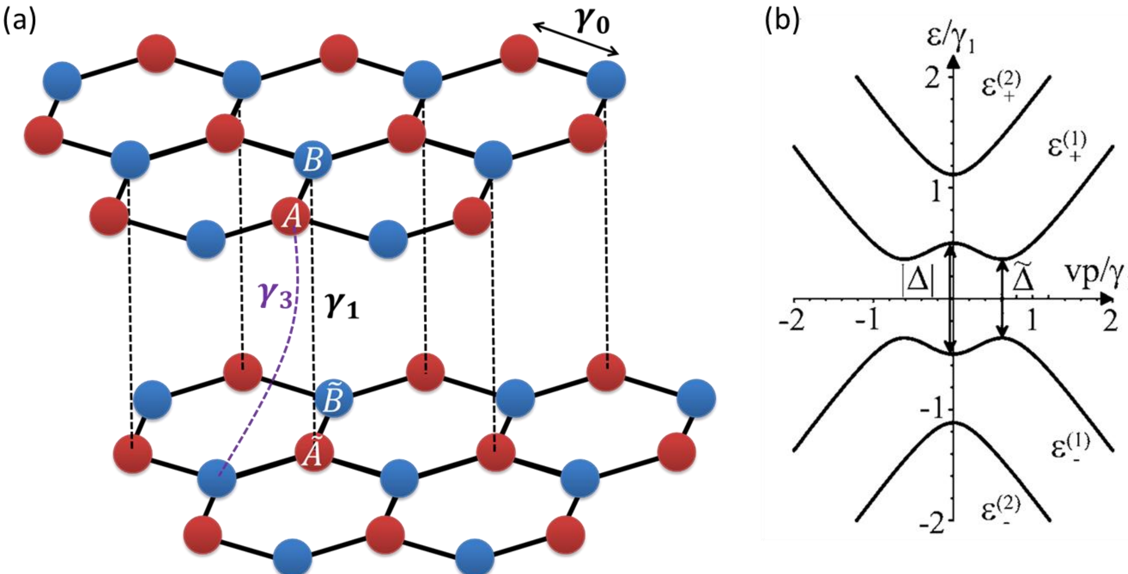

Figure 1.4: (a) schematic of the bilayer graphene lattice containing four carbon atoms in the unit cell: A, B, $\tilde{A}$, and $\tilde{B}$ (atom B of the top bilayer is directly on top of the atom $\tilde{A}$ of the bottom bilayer graphene). The coupling between the carbon atoms of the opposing layers are marked by dashed lines. (b) Energy-momentum dispersion of bilayer graphene close to the K point and in the presence of a finite layer asymmetry $u = \Delta$ (right panel adapted from Ref. [9]).

1.2 TRANSPORT CHARACTERISTICS

Since the early days of monolayer graphene isolation, experimentalists have revealed interesting features in its transport characteristics such as the linear dependence of the conductivity on the carrier density and the possession of a finite minimum conductivity value at the charge neutrality point (Fig. 1.5) [1], [10]. The inconsistency of the experimental observations with prior theoretical predictions initiated a new wave of theoretical efforts to shed light on the physics of the carrier transport in graphene [11]–[15]. In this section, we review the theory of the carrier transport in monolayer graphene. We start with the derivation of the linear Boltzamnn transport equation and continue to solve it in monolayer graphene using relaxation time approximation within the theoretical framework of refs. [16]–[20], which provides a complete transport picture both at low and high carrier densities. Within this framework, we drive the conductivity associated with the long-range Coulomb scattering and the screened short range scattering and show the overall conductivity is consistent with the experimental observations.

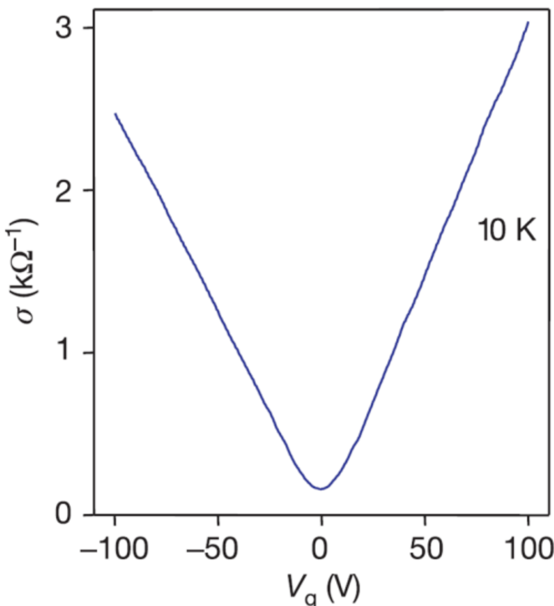

Figure 1.5: Graphene conductivity (σ) vs. gate voltage (V_g) measured in a back-gated graphene field effect transistor at $T = 10\,K$. σ shows a linear dependence on V_g away from the charge neutrality point (Figure and caption adapted from Ref. [10]).

1.2.1 Boltzmann transport equation

The carriers in metals and semiconductors can be affected by external magnetic field, electric field, and temperature gradients as well as scattering from lattice ions, impurities, etc. The state of the carriers in a semiconductor is often described by a distribution function $f(\boldsymbol{k}, \boldsymbol{r}, t)$ which is the probability of finding a particle with the momentum $\boldsymbol{k}$, at the position $\boldsymbol{r}$, and at the time t. Since the distribution function carries information about the state of the particles, it can be used to calculate quantities such as

carrier density and current density. In equilibrium, the distribution function of fermionic quasi-particles is given by Fermi-Dirac distribution:

$$f_0(\boldsymbol{k}, \boldsymbol{r}, t) = \frac{1}{1 + e^{(\epsilon_k - \mu(r))/k_B T(r)}} \qquad (1.3)$$

where μ is the chemical potential, k_B is the Boltzmann constant and T is temperature. In the following, we derive an equation that controls the spatial and temporal evolution of $f(\boldsymbol{k}, \boldsymbol{r}, t)$ known as the Boltzamnn transport equation.

In the absence of any collision, at the time $t + dt$, the distribution function is $f(\boldsymbol{r}', \boldsymbol{k}', t + dt)$ where $\boldsymbol{r}' = \boldsymbol{r} + \dot{\boldsymbol{r}}dt$ and $\boldsymbol{k}' = \boldsymbol{k} + \dot{\boldsymbol{k}}dt$. Assuming the number of particles in the system remains the same:

$$f(\boldsymbol{r}, \boldsymbol{k}, t) d\boldsymbol{r} d\boldsymbol{k} = f\left(\boldsymbol{r} + \dot{\boldsymbol{r}}dt, \boldsymbol{k} + \dot{\boldsymbol{k}}dt, t + dt\right) d\boldsymbol{r}' d\boldsymbol{k}' \qquad (1.4)$$

Based on the Liouville's theorem, the phase-space of the system during the motion remains constant (i.e. $d\boldsymbol{r}d\boldsymbol{k} = d\boldsymbol{r}'d\boldsymbol{k}'$) therefore:

$$f(\boldsymbol{r}, \boldsymbol{k}, t) = f(\boldsymbol{r} + \dot{\boldsymbol{r}}dt, \boldsymbol{k} + \dot{\boldsymbol{k}}dt, t + dt) \qquad (1.5)$$

When collision occurs in the system, an additional term should be added to the eq. 1.5 to account for the collision:

$$f\left(\boldsymbol{r} + \dot{\boldsymbol{r}}dt, \boldsymbol{k} + \dot{\boldsymbol{k}}dt, t + dt\right) = f(\boldsymbol{r}, \boldsymbol{k}, t) + \left(\frac{\partial f(\boldsymbol{r}, \boldsymbol{k}, t)}{\partial t}\right)_{Coll} dt \qquad (1.6)$$

For small time differences, linear expansion of the eq. 1.6 yields:

$$\frac{\partial f}{\partial t} + \dot{\boldsymbol{r}} \cdot \frac{\partial f}{\partial \boldsymbol{r}} + \dot{\boldsymbol{k}} \cdot \frac{\partial f}{\partial \boldsymbol{k}} = \left(\frac{\partial f}{\partial t}\right)_{Coll} \qquad (1.7)$$

Equation 1.7 is the Boltzmann equation. In the semi-classical approximation, we have:

$$\dot{\boldsymbol{r}} = \boldsymbol{v}_k = \frac{1}{\hbar}\frac{\partial \epsilon_k}{\partial \boldsymbol{k}} \qquad (1.8)$$

$$\hbar\dot{\boldsymbol{k}} = -e(\boldsymbol{E} + \boldsymbol{v}_k \times \boldsymbol{B}) \qquad (1.9)$$

where $\boldsymbol{E}$ and $\boldsymbol{B}$ are external electric and magnetic fields, respectively. By inserting $\dot{\boldsymbol{r}}$ and $\dot{\boldsymbol{k}}$ of eqs. 1.8 and 1.9 back into eq. 1.7, we obtain the stationary Boltzmann equation:

$$\boldsymbol{v}_k \cdot \frac{\partial f}{\partial \mathbf{r}} - \frac{e}{\hbar}(\boldsymbol{E} + \boldsymbol{v}_k \times \boldsymbol{B}) \cdot \frac{\partial f}{\partial \mathbf{k}} = \left(\frac{\partial f}{\partial t}\right)_{Coll} \qquad (1.10)$$

There is no analytical solution for the Boltzmann equation in its general form, therefore, we use approximations to find a solution for eq. 1.10. Assuming the solution of eq. 1.10 is only slightly different from the equilibrium distribution (f_0) then we can write the distribution function as:

$$f = f_0 + \delta f \qquad (1.11)$$

where δf is small compared to f_0. Inserting f from eq. 1.11 back into the Boltzmann equation (eq. 1.10) yields:

$$\boldsymbol{v}_k \cdot \frac{\partial f_0}{\partial \mathbf{r}} - \frac{e}{\hbar}(\boldsymbol{E} + \boldsymbol{v}_k \times \boldsymbol{B}) \cdot \frac{\partial f_0}{\partial \mathbf{k}}$$
$$= \left(\frac{\partial f}{\partial t}\right)_{Coll} - \boldsymbol{v}_k \cdot \frac{\partial \delta f}{\partial \mathbf{r}} + \frac{e}{\hbar}(E + \boldsymbol{v}_k \times B) \cdot \frac{\partial \delta f}{\partial \mathbf{k}} \qquad (1.12)$$

As shown in eq. 1.3, the dependence of the distribution function f_0 on the wave and position vectors is through the chemical potential and temperature. Therefore, the left hand side of eq. 1.12 can be written as:

$$\boldsymbol{v}_k \cdot \frac{\partial f_0}{\partial \mathbf{r}} - \frac{e}{\hbar}(\boldsymbol{E} + \boldsymbol{v}_k \times \boldsymbol{B}) \cdot \frac{\partial f_0}{\partial \mathbf{k}}$$

$$= \boldsymbol{v}_k \cdot \frac{\partial f_0}{\partial \epsilon_k} \cdot \left[-\mathrm{e}\left(E + \frac{\nabla_r \mu}{e}\right) - \left(\frac{\epsilon_k - \mu}{T}\right) \nabla_r T \right] \qquad (1.13)$$

Replacing left hand side of eq. 1.12 by eq. 1.13 and keeping only linear in E-field terms yields:

$$\frac{\partial f_0}{\partial \epsilon_k} \boldsymbol{v}_k \cdot \left[\left(-\frac{\epsilon_k - \mu}{T}\right) \nabla_r T - e\left(E + \frac{1}{e} \nabla_r \mu\right) \right]$$

$$= \left(\frac{\partial f}{\partial t}\right)_{Coll} - \boldsymbol{v}_k \cdot \nabla_r \delta f + \frac{e}{\hbar}(\boldsymbol{v}_k \times B) \cdot \nabla_k \delta f \qquad (1.14)$$

It is worth to mention δf is proportional to the applied E- field so in equation 1.14 we neglect terms including product of δf and E as they eventually lead to higher order terms. Solving eq. 1.14 for f is still challenging as the distribution function f appears in the collision term. To simplify the collision term, we use relaxation time approximation:

$$\left(\frac{\partial f}{\partial t}\right)_{Coll} = -\frac{\delta f}{\tau} \qquad (1.15)$$

here, relaxation time τ is the average of the particle collisions time. We will discuss the form of the relaxation time in monolayer graphene in the next section. Using the relaxation time approximation and in the absence of an external magnetic field (i.e. $B = 0$), the solution of the linear Boltzmann equation (eq. 1.14) is:

$$f(k) = f_0(k) + \left(-\frac{\partial f_0}{\partial \epsilon_k}\right) \tau(\epsilon_k) v_k \cdot \left[\left(-\frac{\epsilon_k - \mu}{T}\right) \nabla_r T - e\left(E + \frac{1}{e} \nabla_r \mu\right) \right] \qquad (1.16)$$

At a constant E-field and in the absence of a temperature gradient, the distribution function can be simplified to:

$$f(k) = f_0(k) - e(\boldsymbol{E} \cdot \boldsymbol{v_k})\tau(\epsilon_k)\left(-\frac{\partial f_0}{\partial \epsilon_k}\right) \qquad (1.17)$$

1.2.2 Electrical conductivity

Knowing the distribution function, the current density can be obtained from:

$$\boldsymbol{j} = -e\int \frac{d\boldsymbol{k}}{4\pi^2}\boldsymbol{v}_k[f(\boldsymbol{k}) - f_0(\boldsymbol{k})] \qquad (1.18)$$

By isolating the terms proportional to the E-field, and by assuming current is carried only by electrons close to the Fermi energy, the general form of the conductivity is:

$$\sigma = e^2\tau(\epsilon_F)\int \frac{d\boldsymbol{k}}{4\pi^2}\frac{1}{\hbar}\frac{\partial v_k}{\partial k}\delta f(\epsilon_k) \qquad (1.19)$$

For monolayer graphene with linear energy-momentum dispersion ($E = \pm v_f \hbar |k|$) eq. 1.19 becomes:

$$\sigma = \frac{2e^2}{h}k_F v_F \tau \qquad (1.20)$$

The general form of the graphene conductivity (eq. 1.20) obtained from the linearized Boltzmann transport equation using relaxation time approximation is proportional to τ which is yet to be determined. In the next section we address the calculation of the relaxation time.

1.2.3 Relaxation time

The general form of the relaxation time derived from the scattering by impurities is [17], [20]:

$$\tau(\epsilon_k)^{-1} = \frac{2\pi}{\hbar}\sum_a \int dz n_i^{(a)}(z) \int \frac{d^2k'}{(2\pi)^2} \left|\langle V_{k,k'}(z)\rangle\right|^2$$

$$\times [1 - cos\theta_{kk'}]\delta(\epsilon_k - \epsilon_{k'}) \qquad (1.21)$$

where $\theta_{kk'}$ is the scattering angle, $n_i^{(a)}(z)$ is the density of the ath kind of impurity, z is the coordination in the normal direction, and $\langle V_{k,k'}(z)\rangle$ is the matrix element of the scattering potential associated with impurities and is determined by the configuration of the 2D system and the spatial distribution of the impurities. Calculation of the relaxation time requires knowledge about the spatial distribution of the scattering sites. While calculating the precise value of the relaxation time for randomly distributed impurities in three dimensions is complicated, for simplicity, we assume the impurities are randomly scattered in a 2D plane parallel to the graphene at $z = d$. As a result, the term associated with the matrix element of the scattering potential becomes:

$$\int dz n_i^{(a)}(z)\left|\langle V_{k,k'}(z)\rangle\right|^2 = n_i \left|\frac{v_i(|k - k'|)}{\varepsilon(k - k')}\right|^2 F(|k - k'|) \qquad (1.22)$$

where n_i is the density of the impurities, $F(|k - k'|)$ is the form factor associated with the wave function of the carriers, $v_i(q) = 2\pi e^2/(\kappa q)e^{-qd}$ is the Fourier transform of the Coulomb potential in an effective lattice dielectric constant k, and $\varepsilon(q)$ is the 2D static Random-Phase-Approximation (RPA) dielectric function given by:

$$\varepsilon(q,T) = 1 + V^C(q)\Pi(q,T) \qquad (1.23)$$

where $V^C(q)$ is the Coulomb interaction and $\Pi(q,T)$ is the polarizability function.

The exact form of the dielectric function through Random-Phase-Approximation (RPA) is known [21], however, for simplicity we use the following approximation for dielectric function:

$$\varepsilon(q) = \begin{cases} 1 + \dfrac{4k_F r_s}{q} & if\ q < 2k_F \\ 1 + \dfrac{\pi r_s}{2} & if\ q > 2k_F \end{cases} \qquad (1.24)$$

With the matrix element of the scattering potential given in eq. 1.22 and the dielectric function given in eq. 1.24, the corresponding relaxation time and therefore conductivity can be calculated. Before continuing with the calculation of the monolayer graphene conductivity, it is worth to mention that carriers in monolayer graphene are confined to a one-atom thick layer. As a result, the effect of surrounding environment on the electronic properties of monolayer graphene can be more pronounced than other 2DEGs. In the following, we define the coupling constant for monolayer graphene to address the effect of environment on charge carriers.

1.2.4 Coupling constant

The coupling constant α is defined as the ratio between the Coulomb potential energy and the kinetic energy of an electron system and is a measure of the electron-electron interaction strength in such system. For a monolayer graphene sandwiched

between two different environments with dielectric constants k_1 and k_2, the coupling constant is:

$$\alpha = \frac{2e^2}{(k_1 + k_2) v_F \hbar} \qquad (1.25)$$

The dimensionless coupling constant of graphene is independent of the carrier density owing to its linear energy-momentum dispersion. Consequently, in monolayer graphene, Coulomb potential of impurities is renormalized by screening and directly affects the transport characteristics.

1.2.5 Long-range scattering

Now we turn to the calculation of the monolayer graphene conductivity. The relaxation time associated with the Coulomb scattering can be obtained using the dielectric function of eq. 1.24. Monolayer graphene conductivity associate with the long-range Coulomb scattering is:

$$\sigma_l = \frac{2e^2}{h} \frac{n}{n_{imp}} \frac{1}{F_l(\alpha)} \qquad (1.26)$$

where n is the carrier density, n_{imp} is the density of charged impurities, and $F_l(\alpha)$ is:

$$F_l(\alpha) = \pi\alpha^2 + 24\alpha^3(1 - \pi\alpha) + \frac{16\alpha^3(6\alpha^2 - 1)\arccos(1/2\alpha)}{\sqrt{4\alpha^2 - 1}} \qquad (1.27)$$

Equation 1.26 shows the monolayer graphene conductivity associated with the long-rang Coulomb scattering has a linear dependence on the carrier density consistent with the experimentally measured graphene conductivity [1], [10] which suggests that

Coulomb scattering is the dominant scattering mechanism away from the charge neutrality point.

1.2.6 Screened short-range scattering

We also address the contribution of the screened short range scattering on monolayer graphene conductivity. For short-range disorder, the matrix element of the scattering potential is:

$$\int dz n_i^{(a)}(z) \left| \langle V_{k,k'}(z) \rangle \right|^2 = n_d V_0^2 \, F(|k-k'|) \qquad (1.28)$$

where n_d is 2D impurity density and V_0 is a constant representing the potential strength. The conductivity associated with the screened short range scattering is:

$$\sigma_s = \frac{\sigma_0}{F_s(\alpha)} \qquad (1.29)$$

where σ_0 is a constant and $F_s(\alpha)$ is given by:

$$F_s(\alpha) = \frac{\pi}{2} - \frac{32\alpha}{3} + 24\pi\alpha^2 + 320\alpha^3(1-\pi\alpha) + 256\alpha^3(5\alpha^2 - 1)\frac{\arccos(1/2\alpha)}{\sqrt{4\alpha^2 - 1}} \qquad (1.30)$$

Unlike σ_l, σ_s is independent of the carrier density. Combining the long-range and short-range conductivities from eqs. 1.26 and 1.29, the overall monolayer graphene conductivity is:

$$\sigma^{-1} = \sigma_l^{-1} + \sigma_s^{-1} \qquad (1.31)$$

1.3 Raman Spectrum

Raman spectroscopy is a powerful characterization tool that has been used for decades to study the structural and electronic properties of molecules and semiconductor materials. In particular, it has been an integral part of research on carbon allotropes in the past 40 years [22], and more recently it is widely used as a fast, high resolution, and non-destructive method to measure various quantities associated with graphene such as number and orientation of layers, edge chirality and purity, doping, strain, etc. In the following, we review the fundamentals of the Raman spectroscopy and introduce the Raman signatures of monolayer and bilayer graphene, and briefly discuss the origin of the signature bands.

1.3.1 Raman scattering

Raman spectroscopy utilizes Raman scattering to reveal the atomic structure and electronic properties of materials. In the interaction of photons with a medium, majority of photons get either reflected or transmitted through without carrying finger prints of the medium. This is due to the Rayleigh (elastic) scattering of photons and it occurs when electrons excited by incident photons return to their initial state by emitting photons similar to the incident photons. While most photons get elastically scattered, a small portion of them experience inelastic scattering by phonons which subsequently leads to the emission/absorption of phonons and emission of secondary (scattered) photons. The inelastic scattering of photon by phonons is called Raman scattering and is characterized

by the energy difference between the scattered and incident photons. Assuming k_{in} (k_{sc}) and ω_{in} (ω_{sc}) are the wave vector and frequency of the incident (scattered) photons, respectively, and q and Ω_q^ν are those of a phonon from branch ν, then from energy and momentum conservation we have:

$$\begin{cases} \omega_{in} = \omega_{sc} \pm \Omega_q^\nu \\ k_{in} = k_{sc} \pm q \end{cases} \qquad (1.32)$$

where plus (minus) sign corresponds to creation (absorption) of a phonon. Figure 1.6 schematically shows the Rayleigh and Raman scattering processes.

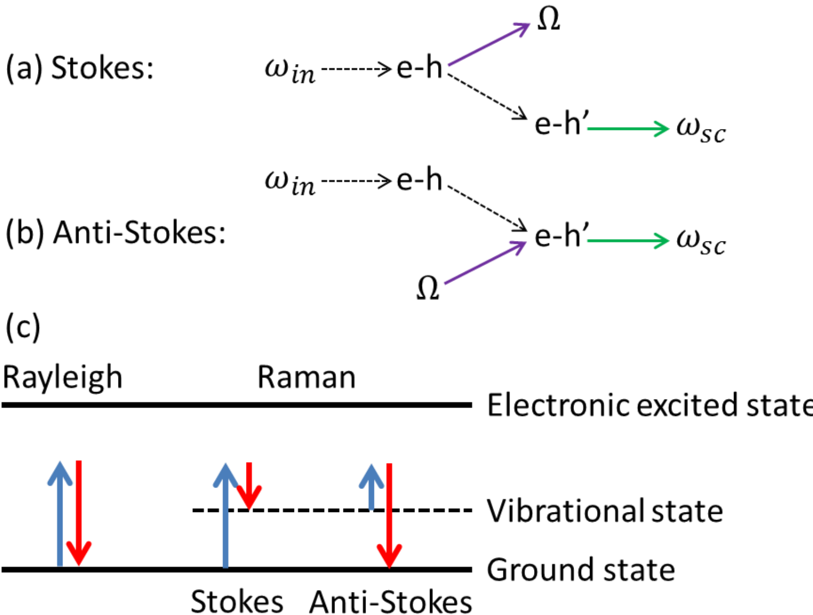

Figure 1.6 Rayleigh and Raman Scattering. (a) Stokes Raman scattering: an incident photon creates an electron-hole pair which subsequently decay into a phonon Ω and another electron-hole pair e-h'. A photon with frequency ω_{sc} is emitted when the secondary electron-hole recombine (b) Anti-Stokes Raman scattering: similar to the Stokes except that the phonon is absorbed by the electron-hole pair. (c) Comparison of the Rayleigh and Raman scatterings.

Since Raman scattering is closely related to the electrons, any change in the electronic properties of a medium, e.g. due to defects or doping, can affect the position, width, or intensity of the peaks in the Raman spectrum.

1.3.2 Raman signatures of monolayer and bilayer graphene

Raman scattering involves the emission or absorption of phonons, thus, to better understand the Raman spectrum of graphene it is instructive to start with its phonon dispersion. The Bravais lattice of monolayer graphene consists of two-atom basis that gives rise to six branches in the phonon dispersion: three optical (O) and three acoustic (A) braches. One branch of each group (acoustic and optical) originates from out of plane (o) vibrations of the carbon atoms and the remaining two branches originate from in-plane (i) longitudinal (L) and transverse (T) vibrations. Figure 1.7(a) shows the first Brillion zone of monolayer graphene where high symmetry points (i.e. Γ, K, K', M) are marked and Fig. 1.7(b) illustrates the phonon dispersion of monolayer graphene calculated using the density function theory (DFT) [23], [24].

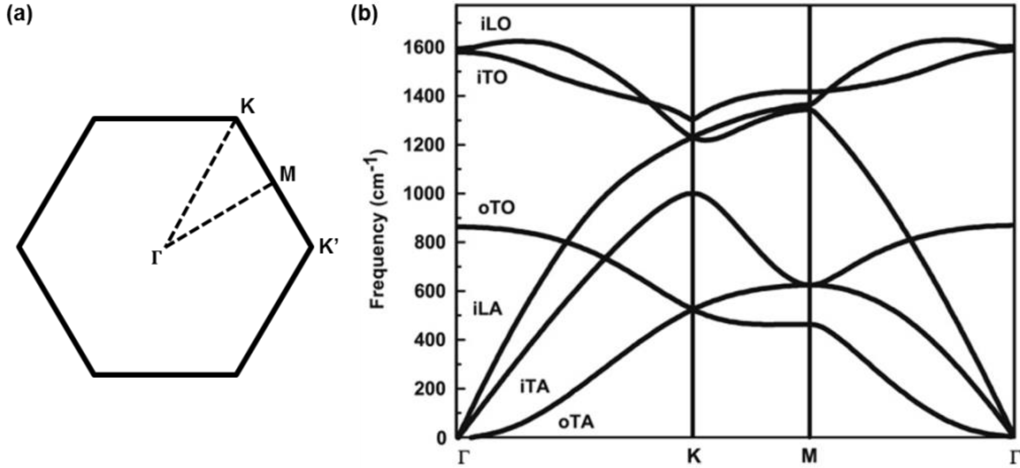

Figure 1.7: (a) The first Brillion zone of monolayer graphene with Γ, K, K', and M points marked. (b) monolayer graphene phonon dispersion calculated by DFT (Figure and caption adapted from Refs. [23], [24]).

Raman spectra of monolayer and bilayer graphene and graphite measured using a green laser ($\lambda = 532\ nm$) is shown in Fig. 1.8. There are two distinct peaks in the three Raman spectra labeled as G and 2D peaks. The G peak at the Raman shift $\sim 1580\ cm^{-1}$ stems from a first order Raman scattering process and is associated with doubly degenerate iTO and iLO phonon mode at the center of the Brillion zone Γ. The second peak is 2D peak at the Raman shift of $\sim 2700\ cm^{-1}$ which originates from a second-order Raman scattering process involving two iTO phonons close to the K point. In disordered graphene, another peak appears at the Raman shift of $1350\ cm^{-1}$ known as D peak. The D peak is also associated with a second-order Raman scattering but unlike 2D peak it involves one iTO phonon and a defect. Figure 1.9(a) schematically presents the Raman scatterings for D, G, and 2D peaks in monolayer graphene.

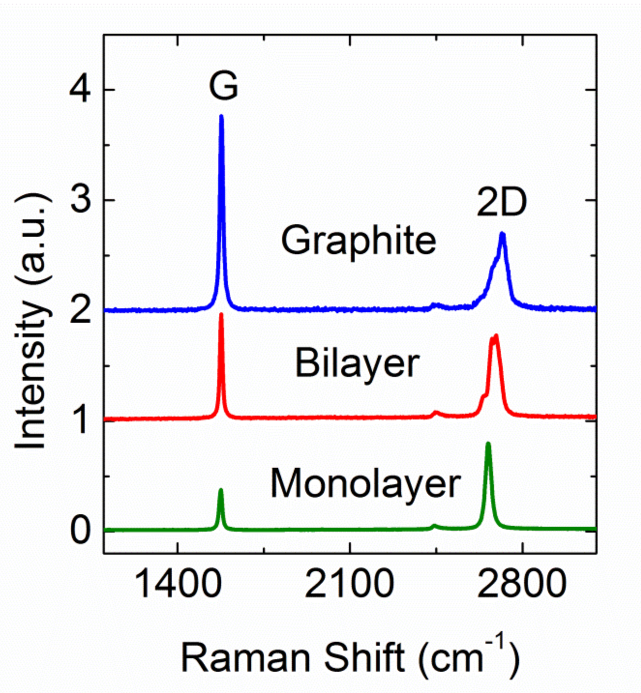

Figure 1.8: Raman spectra of graphene, bilayer graphene, and graphite measured using a green laser ($\lambda = 532\, nm$). The signature G ($\sim 1580\, cm^{-1}$) and 2D ($\sim 2700\, cm^{-1}$) peaks are mark.

The phonon dispersion of bilayer graphene is similar to that of monolayer graphene except that each branch splits into two branches corresponding to symmetric and antisymmetric vibrations of the atoms in the two layers. Similarity of the phonon dispersions especially close to the Γ point yields a G peak similar to that of monolayer graphene. However, a noticeable difference between the Raman spectrum of bilayer and monolayer graphene is in the shape and the width of the 2D peak. As shown in Fig. 1.9(b), the Raman scattering associated with the bilayer graphene 2D peak has four components, so the width of bilayer graphene 2D peak ($\sim 50\, cm^{-1}$) is wider than that of

monolayer ($\sim 25\ cm^{-1}$) and it can be used to unambiguously distinguish bilayer from monolayer graphene.

Figure 1.9: Raman processes in (a) monolayer graphene (b) bilayer graphene. Solid lines present energy-momentum dispersion, blue (red) arrows present intraband transitions by absorption (emission) of photons, dashed arrows present interband transitions accompanied by phonon emission/absorption, and dotted arrows present electrons scattered by defects.

1.4 TWO-DIMENSIONAL ELECTRON GAS IN MAGNETIC FIELD

Free electrons in a magnetic field (B) form cyclotron orbits. In three dimensional metals and semiconductors, the response of free electrons to a magnetic field leads to classical Hall effect. The response of a 2DEG to a perpendicular magnetic field is remarkably different. In the presence of a perpendicular magnetic field, the transverse (Hall) conductivity of a 2DEG shows quantized plateaus at $\sigma_{xy} = \nu\, e^2/h$ where ν is an integer number known as filling factor and given by $\nu = nh/eB$. Figure 1.10(a) shows the quantized σ_{xy} vs. ν of a conventional 2DEG with parabolic energy-momentum dispersion. The Hall conductivity plateaus are accompanied by vanishing longitudinal resistivity ($\rho_{xx} = 0$). The integer Quantum Hall effect (QHE) in a 2DEG can be explained by considering the effect of magnetic field on its band structure. Adding a vector potential term (associated with the applied magnetic field) to the Hamiltonian of a 2DEG system yields a Hamiltonian analogous to that of a quantum harmonic oscillator with discrete energy levels $E_N = \hbar\omega_c(N + 1/2)$ known as Landau levels (LLs) where N is the orbital index, $\omega_c = eB/m^*$ is the cyclotron frequency, and m^* is the carrier effective mass. Figures 1.10(b) and (c) show the quantized LLs of a 2DEG with no disorder and with low disorder, respectively. Electrons in a disordered 2DEGs and in a perpendicular magnetic field circulate and drift along the equipotential contours. Electrons close to the center of LLs occupy the extended states and contribute to the conduction while electrons at the tail of the LLs are localized by disorder potential. The population of these states limits the conduction to the edge of the medium where

chemical potential crosses the fully occupied LLs. In this condition, the conductivity of the medium is set by the edge states and remains constant while the localized states are populated. In addition, the conduction through one-dimensional edge states is dissipationless due to the absence of low energy states to scatter to which results in vanishing ρ_{xx}.

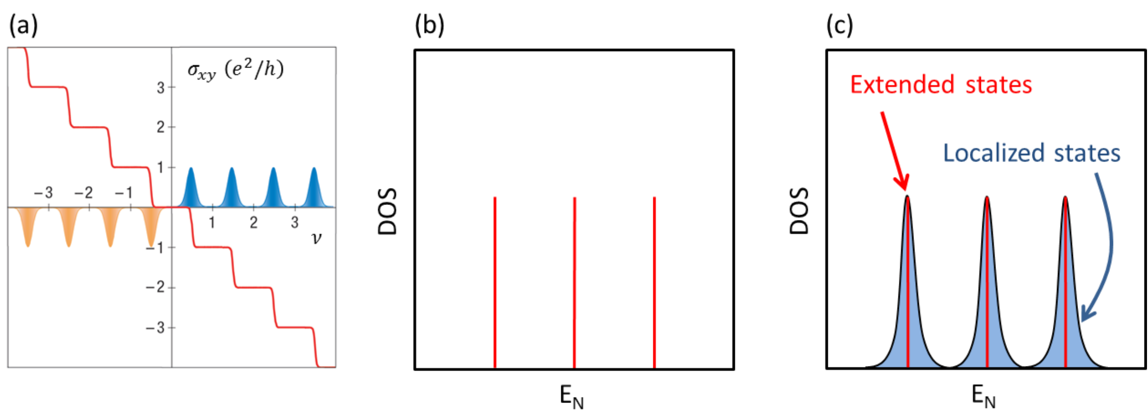

Figure 1.10: Schematic illustration of (a) integer quantum Hall effect in a 2DEG with parabolic energy-momentum dispersion. (b) Landau levels of an ideal 2DEG (c) Landau levels of a disordered 2DEG (Left panel adapted from Ref. [25]).

1.4.1 Quantum Hall effect in monolayer graphene

Although carriers in monolayer graphene form a 2DEG, the QHE in monolayer graphene presents unique features that are different from a conventional 2DEG with parabolic energy-momentum dispersion. Compared to a conventional 2DEG, the sequence of QHSs in monolayer graphene is shifted by a half integer and occur at the filling factors $\nu = \pm 4(M + 1/2)$ where M is an integer number [Fig. 1.11(a)].

Monolayer graphene LLs are four fold degenerate, two from spin degeneracy and two from valley degeneracies, with energies given by:

$$E_N = \pm v_F \sqrt{2e\hbar BN} \qquad (1.33)$$

Eq. 1.33 shows the spacing between the monolayer graphene LLs scales with $\sqrt{N}$ unlike a conventional 2DEG where the spacing is independent of the LL index.

Monolayer graphene possesses a distinctive LL at zero energy which stems from the particle-hole symmetry. As shown in Fig. 1.11(a), the zero energy LL consists of electron and hole states (with equal contribution) that leads to the half integer shift in the number of flux quanta required to fill a full integer LL. At zero energy, and at valley K or K', the wavefunctions reside entirely on one of the carbon sublattices, A or B, while for non-zero energies, there is an equal chance to find them on each sublattice.

1.4.2 Quantum Hall effect in bilayer graphene

The QHE in bilayer graphene differs from that of a conventional 2DEG and monolayer graphene. The Berry phase of 2π in bilayer graphene leads to the LL energies:

$$E_N = \hbar\omega_c \sqrt{N(N-1)} \qquad (1.34)$$

with filling factors $\nu = \pm 4(M+1)$, where M is an integer number. Fig. 1.11(b) shows the QHSs of bilayer graphene. Similar to the monolayer graphene LLs, bilayer graphene LLs are fourfold degenerate due to the spin and valley degeneracies, however, the lowest LL in bilayer graphene (i.e. at zero energy) includes both $N = 0$ and $N = 1$ orbitals with eight fold degeneracy.

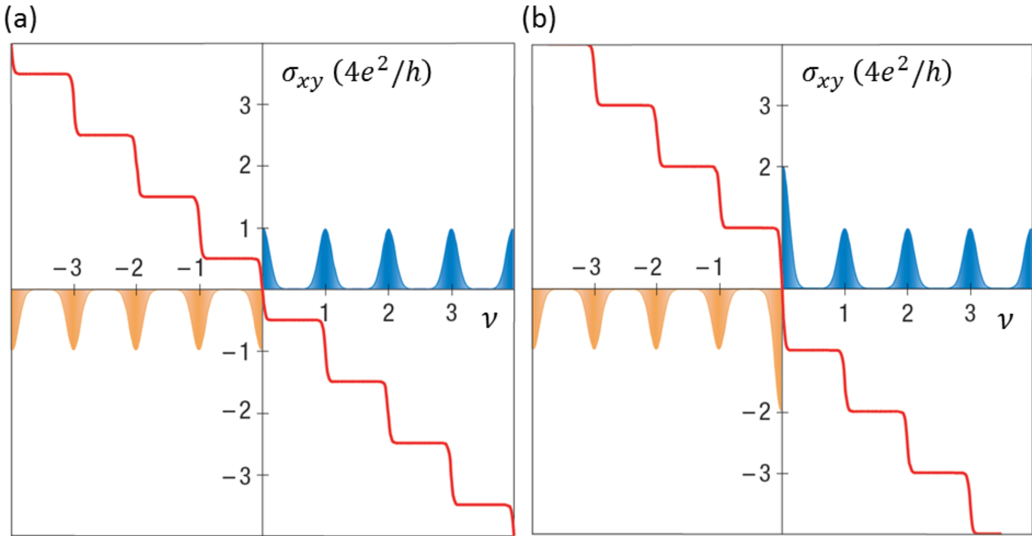

Figure 1.11: Schematic illustration of integer quantum Hall effect in (a) monolayer graphene with conductivity plateaus at $\nu = \pm 4(M + 1/2)$ (b) bilayer graphene with conductivity plateaus at $\nu = \pm 4(M + 1)$ (Figure adapted from Ref. [25]).

1.5 CHAPTER ORGANIZATION

In Chapter 2, we focus on the integration of metal-oxide dielectrics with monolayer and bilayer graphene and study carrier mobility in graphene in the presence of metal-oxide dielectrics as well as thickness scaling of top dielectric in dual-gated graphene field-effect transistors. In chapter 3, we study the 2D-2D tunneling in double bilayer graphene heterostructures and show resonant tunneling and negative differential resistance in their interlayer current-voltage characteristics. In chapter 4, we study the Raman spectrum and magneto-transport characteristics of A-B stacked and rotationally misaligned bilayer graphene grown by chemical-vapor-deposition (CVD).

CHAPTER 2: GRAPHENE FIELD-EFFECT TRANSISTOR WITH METAL OXIDE TOP DIELECTRIC

High-k dielectrics are an essential component of aggressively scaled complementary metal-oxide semiconductor (CMOS) devices [26] and will likely play a role for graphene based devices. Technological advances on the integration of high-*k* dielectrics and silicon FETs have paved the road for application of high-*k* dielectrics in electron devices with alternative channel materials such as graphene, nevertheless, despite the considerable progress in silicon devices, the incorporation of high-*k* dielectrics in graphene electron devices comes with its own unique challenges.

In this chapter, we study the integration of high-*k* dielectrics in monolayer and bilayer graphene FETs. We investigate the carrier mobility in back-gated monolayer and bilayer graphene FETs with a top HfO_2 dielectric (namely device type 1) as a function of the HfO_2 film thickness and temperature and show that the carrier mobility decreases during the deposition of the first 2-4 nm of top dielectric and remains constant for thicker layers. Our data strongly suggest that fixed charged impurities located in close proximity to the graphene are responsible for the mobility degradation.

In the second section, we study the thickness scaling of Al_2O_3 and HfO_2 dielectrics deposited by atomic layer deposition (ALD) on graphene using ultra-thin, oxidized evaporated Al and Ti nucleation layers and show because of a lower surface diffusion of Ti in comparison to Al, the minimum metal film thickness needed for full surface coverage is 0.6 nm for Ti and 1.2 nm for Al. We fabricated dual-gated graphene

FETs (namely device type 2) with top Al_2O_3 dielectric thicknesses down to 2 nm, using both Ti and Al nucleation layers. Our results show that the nucleation layer impacts the dielectric constant and morphology of the ALD Al_2O_3, and adds a series contribution to the top gate capacitance. Furthermore, transmission electron microscopy (TEM) reveals that the observed difference in the Al_2O_3 dielectric constant is a result of the structural difference between the two films, with the Al_2O_3 grown on Ti being partially crystalline and that on Al being amorphous.

2.1 INTRODUCTION

Graphene is considered as an alternative channel material and a promising candidate for nanoelectronic devices [27] owing to its high carrier mobility [28], chemical and mechanical stability [29], and the potential for scalability to nanometer dimensions. While the intrinsic carrier mobility in graphene is very high, with values of ≅ 200,000 $cm^2/V{\cdot}s$ reported in suspended graphene [30], scattering by charged impurities [31], surface roughness [32], and phonons [33] reduce the mobility in graphene devices integrated with dielectrics.

Graphene was first mechanically exfoliated and isolated on a 300 nm-thick SiO_2/Si substrate. The visibility of graphene on SiO_2, combined with the availability and the compatibility of SiO_2 with silicon fabrication processes made SiO_2/Si a widely used substrate for graphene. Consequently, majority of the graphene properties were first experimentally examined on SiO_2/Si substrate.

The mobility of graphene on SiO_2/Si is limited by three scattering mechanisms: longitudinal acoustic (LA) phonons, remote interfacial phonon, and impurity scattering. Figure 2.1 shows the carrier mobility (μ) vs. temperature (T) in graphite and graphene measured on SiO_2/Si substrate [33]. While theoretical calculations suggest the remote interfacial phonon scattering limits the room temperature mobility of graphene on SiO_2/Si to $\mu \cong 40{,}000$ $cm^2/V \cdot s$, in practice, the charged impurity scattering dominates the transport characteristics and limits the mobility to values lower than 10,000 $cm^2/V \cdot s$.

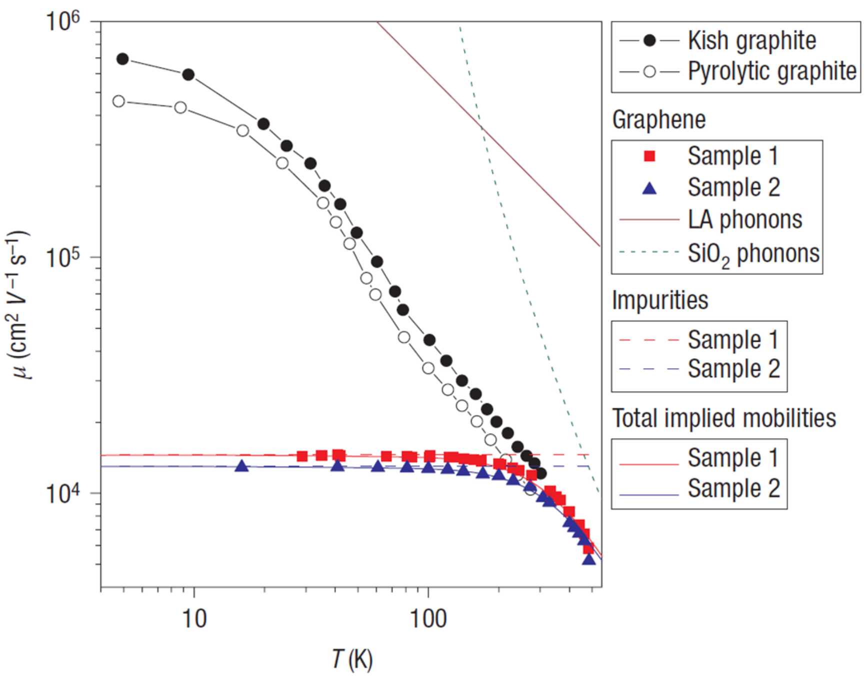

Figure 2.1: Temperature dependence of mobility in graphene and graphite on SiO_2/Si substrate. The experimental mobility values are measured at carrier density $n = 1 \times 10^{12}$ cm^{-2}. Three scattering mechanisms limiting mobility in graphene: scattering by LA phonons (dark red solid line), remote interfacial phonon scattering (green dashed line), and impurity scattering (red and blue dashed lines). The calculated net mobility values for two samples are marked by red and blue solid lines (Figure and caption adapted from Ref. [33]).

In chapter 1, an expression for the graphene conductivity (eq. 1.26) associated with the long-range Coulomb scattering was derived. The carrier mobility corresponding to eq. 1.26 is:

$$\mu = \frac{2e}{h} \frac{1}{n_{imp}} \frac{1}{F_l(\alpha)} \qquad (2.1)$$

where n_{imp} is the density of charged impurities, $\alpha = 2e^2/(k_1 + k_2)v_F\hbar$ is the coupling constant introduced in chapter 1, and $F_l(\alpha)$ is defined by eq. 1.27. In effect, using a high-k dielectric medium in the vicinity of graphene, yields a lower α with better screening of charged impurities located in proximity to graphene. Equation 2.1 and 1.27 combined, indicate a lower α yields a higher mobility in graphene. Consequently, one way to access higher mobilities in graphene is to use high-k dielectrics.

Several experimental studies have examined the impact of using a top medium- or high-k dielectric [34]–[37] on the carrier mobility in graphene. Figure 2.2 shows the mobility vs. number of ice layers deposited on top of a back-gated monolayer graphene FET measured at 77 K [34]. A gradual mobility increase (up to 30%) as a function of ice thickness is observed in monolayer graphene which can be explained by 30% decrease in α associated with the higher dielectric constant of ice ($k \cong 3.2$) compared to vacuum.

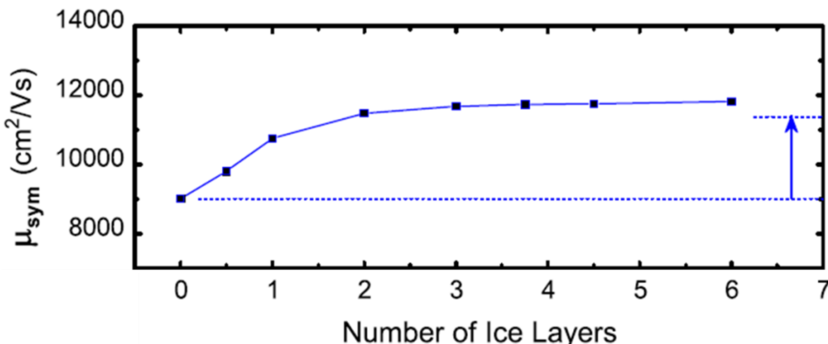

Figure 2.2: Mobility vs. number of ice layers deposited on top of a back-gated graphene FET measured at 77 K. ≅ 30% mobility increase observed after ice deposition (Figure adapted from Ref. [34]).

Chen *et al.* demonstrated a mobility enhancement (≅ 7×10^4 $cm^2/V\cdot s$) at room temperature with deposition of high dielectric constant liquids (k = 32-189) on graphene devices fabricated on SiO_2/Si substrates [35]. Ponomarenko *et al.* observed a mobility enhancement factor of 2 and 1.5 when covering graphene with glycerol ($k \cong 45$), and ethanol ($k \cong 25$) respectively [36].

The carrier mobility in graphene devices with conventional medium- or high-k metal-oxide dielectrics, such as Al_2O_3 or HfO_2 are typically lower than the mobility of back-gated graphene devices. Indeed, the highest reported mobility values in graphene devices with Al_2O_3 ($k \cong 6$) top dielectric is ≅ 8600 $cm^2/V\cdot s$ [37], and typical mobility values for graphene with HfO_2 top dielectric are below 5000 $cm^2/V\cdot s$ [38].

Understanding the impact of the dielectric on mobility in graphene is not only technologically relevant, but can shed light on the scattering mechanism in this material. Furthermore, examining the thickness scalability of the high-k dielectrics in graphene

devices is valuable as it can lead to assessment of graphene devices as a potential candidate for future nanoelectronics.

2.2 Atomic Layer Deposition of Metal-Oxide Dielectrics on Graphene

The deposition of ultra-thin high-k dielectrics on graphene is a key component for graphene FETs. The deposition of ultrathin films is particularly difficult because of chemical inactivity of the graphene surface. Both physical vapor deposition (PVD) and atomic layer deposition (ALD) have been used to deposit dielectrics on graphene, each technique possessing trade-offs. For example, direct deposition of dielectrics on exfoliated graphene by PVD methods, such as electron-beam evaporation [39], radio frequency (RF) sputtering [40], and pulsed laser deposition (PLD) [41] result in structural damage to graphene as confirmed by Raman spectroscopy and mobility measurements of top-gated graphene field-effect transistors [39]–[41]. Dielectric deposition on graphene by ALD, a method which possesses excellent conformality and film thickness control [42], [43], is stymied by the chemical inertness of the graphene surface [44], [45]. As such, the ALD of dielectrics on graphene requires a nucleation layer. A number of graphene surface treatments have been evaluated, such as exposure to NO_2 [46], [47] or ozone [48], spin coated polymers [49], molecular buffer layers [50], or the deposition of a thin metal film which is subsequently oxidized [37]. Desirably, the nucleation layer used to deposit the ALD dielectric should not add charged impurities, interface traps, and permit thickness scaling of the dielectric.

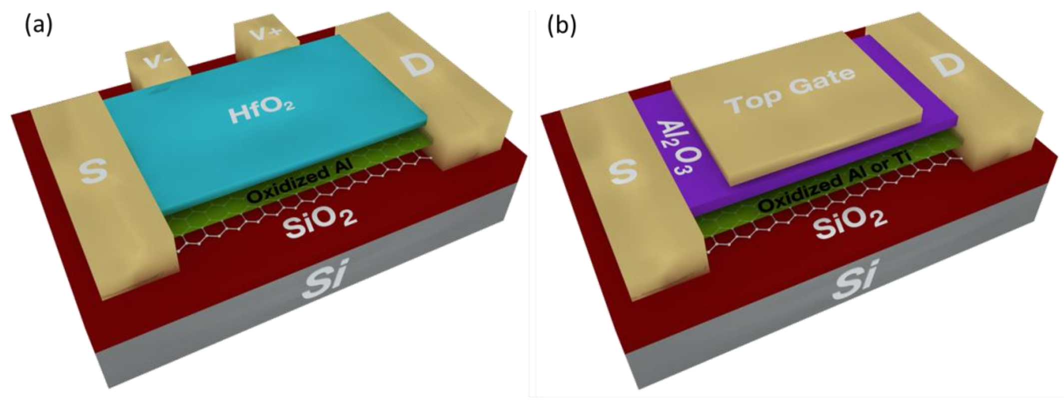

Figure 2.3: Schematic view of (a) device type 1: a back-gated graphene FET with a 285-nm thick SiO_2 bottom dielectric, and a top dielectric stack consisting of an oxidized Al layer and ALD HfO_2 (b) device type 2: dual-gated graphene FET with a top dielectric stack consisting of an oxidized Al or Ti layer and ALD Al_2O_3.

2.3 DEVICE FABRICATION

Figure 2.3 shows the schematic view of the devices type 1 and 2. Fabrication of both device types begins with the mechanical exfoliation of graphene from natural graphite ("Flaggy Flake" from NGS Natugraphit GmbH) using polyethylene tape (from UltraTape, part #1112) on 285 nm-thick SiO_2 thermally grown on highly-doped Si substrates (n-type, <100>, arsenic dopant, $N_D > 10^{20}$ cm^{-3}). Figures 2.4(a-c) show optical micrographs of natural graphite flakes [panel (a)], graphite flakes on a tinted blue polyethylene tape with acrylic adhesive [panel (b)], and a SiO_2/Si substrate with Pt/Cr alignment marks prepared for graphene exfoliation [panel (c)]. After mechanical exfoliation of graphene, monolayer and bilayer graphene flakes on SiO_2/Si substrates are identified by Raman spectroscopy [51] and optical contrast [Fig. 2.4(d)] [52]. After

isolation of monolayer and bilayer graphene flakes, the active regions (two-point, four-point, and Hall bar) are defined by electron-beam (e-beam) lithography, and the excess graphene is etched by oxygen plasma. Metal contacts to graphene are defined by e-beam lithography, 50-nm thick Ni deposition, and lift-off. Figure 2.4(e) shows an optical image of the back-gated graphene FET. From this point, the back-gated graphene FETs go through two different fabrication processes to yield devices type 1 and 2.

For device type 1, a back-gated graphene FET with top HfO_2 dielectric, prior to the HfO_2 deposition, a thin (1.5 ± 0.1 nm) pure Al film (99.999%) is deposited by e-beam evaporation to provide nucleation sites for the ALD process [26], [37]. The metal film is oxidized in the presence of residual O_2 during evaporation and ambient O_2 exposure after removal from the deposition chamber [53], [54] and forms a thin metal-oxide interface film. The sample is then transferred to the ALD chamber for successive, 1 ± 0.1 nm thick HfO_2 deposition cycles. The HfO_2 ALD was performed at a temperature of 200 °C using TEMAH and H_2O as precursors without post-deposition annealing.

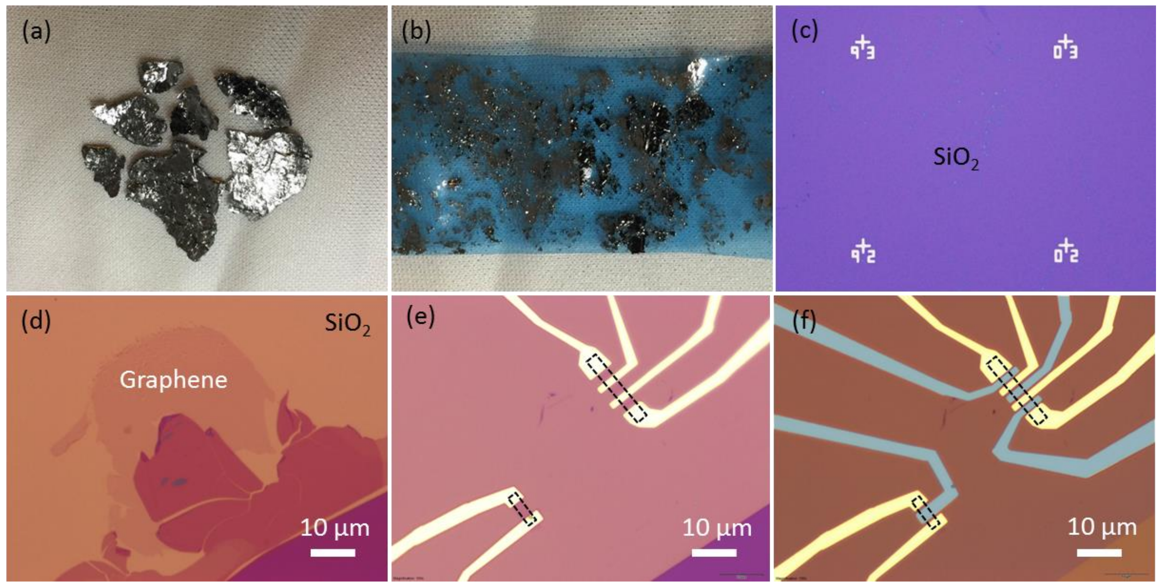

Figure 2.4: Optical micrographs of (a) natural graphite flakes (b) natural graphite flakes on polyethylene tape (c) 285 nm-thick thermally grown SiO_2 on Si substrate with Pt/Cr alignment marks 200 µm apart and ready for graphene exfoliation (d) as exfoliated monolayer and multilayer graphene on SiO_2/Si substrate (e) a back-gated graphene FET (f) a dual-gated graphene FET. The contacts (top gates) are marked in light (dark) color. The scale bar in panels (a) and (b) are the same and defined by the width of the tape which is 1 inch.

For device type 2, a thin metal film of either Ti (0.6 ± 0.1 nm) or Al (1.5 ± 0.1 nm) is deposited on the back-gated graphene FETs by e-beam evaporation. After removing from deposition chamber, the samples are loaded into the ALD chamber, where the Al_2O_3 top gate dielectric is deposited at 250 °C using trimethylaluminum (TMA) and water as precursors with no post deposition annealing. Lastly, the top gate is defined by e-beam lithography followed by metal (Ni) deposition, and lift off. An optical micrograph of device type 2, dual-gated graphene FET, is shown in Fig. 2.4(f).

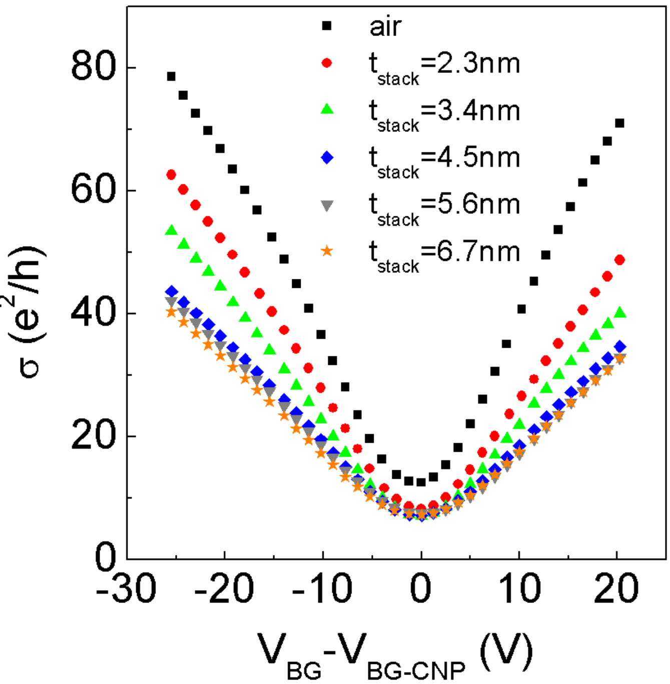

Figure 2.5: σ vs. V_{BG}, determined using four-point measurements, for different top dielectric stack thicknesses (t_{stack}). V_{BG} values of x-axis are offset by the charge neutrality voltage (V_{BG-CNP}), at which the graphene conductivity is minimum.

2.4 Dependence of the mobility on top metal-oxide dielectric thickness

2.4.1 Conductivity and carrier mobility

We first present characteristics of the device type 1. The four-point device conductivity (σ) measured as a function of the back-gate bias (V_{BG}), at room temperature, under vacuum, and for different total top dielectric thicknesses (t_{stack}) are shown in Fig. 2.3. The total top dielectric thicknesses (t_{stack}) includes the nucleation layer thickness and HFO_2 dielectric thickness. The data are measured before the dielectric deposition and

also after each incremental HfO_2 deposition. The measurement shows the minimum conductivity of the device at the charge neutrality point drops from $12e^2/h$ to $8e^2/h$ after deposition of the Al and first HfO_2 layer and is unchanged with the further HfO_2 depositions. Using the σ vs. V_{BG} data, the carrier mobility (μ) is extracted after each HfO_2 deposition which in turn provides us with the dielectric stack thickness (t_{stack}) dependence of the carrier mobility.

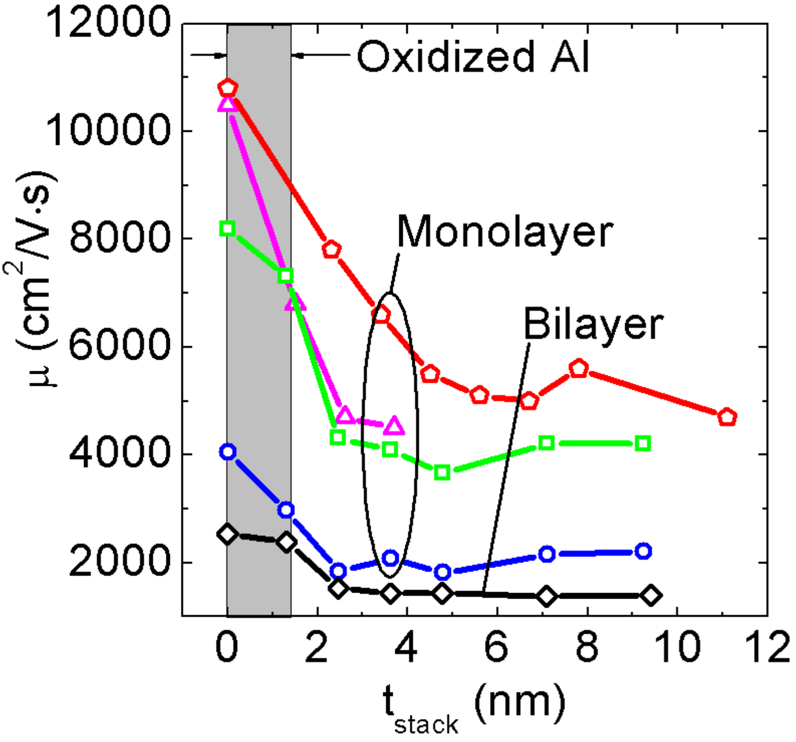

Figure 2.6: μ vs. t_{stack} for four monolayer and one bilayer graphene samples measured at room temperature. The mobility decreases steeply after the first 2-4 nm of oxide deposition, and remains constant for thicker dielectric films.

The carrier mobility of electrons and holes are calculated from the linear slope of σ vs. V_{BG} data, using:

$$\mu = \frac{1}{C_{BG}} \frac{d\sigma}{dV_{BG}} \qquad (2.1)$$

where $C_{ox} \cong 12$ nF/cm^2 is the SiO_2 bottom dielectric capacitance. To avoid the non-linearity around the minimum conductivity point when extracting the $d\sigma/dV_{BG}$, we exclude a 6 V voltage window centered at the charge neutrality point back-gate bias (V_{BG-CNP}), and average out the slopes of σ vs. V_{BG} over a 25 V V_{BG} window, on the electron and hole branches. We note that our approach of using the slope of σ vs. V_{BG} data to extract the mobility neglects short-range scattering, e.g. from neutral impurities [19]. Taking into account the effect of short-range scattering, the extracted mobility values in our samples would changes only slightly, by $\cong 10\%$.

The data in Fig. 2.6 shows the mobility (μ) vs. dielectric stack thickness (t_{stack}), measured for four monolayer and one bilayer device at room temperature. A mobility drop is observed after formation of the oxidized Al buffer layer, and also deposition of the first 1-2 nm of HfO_2.

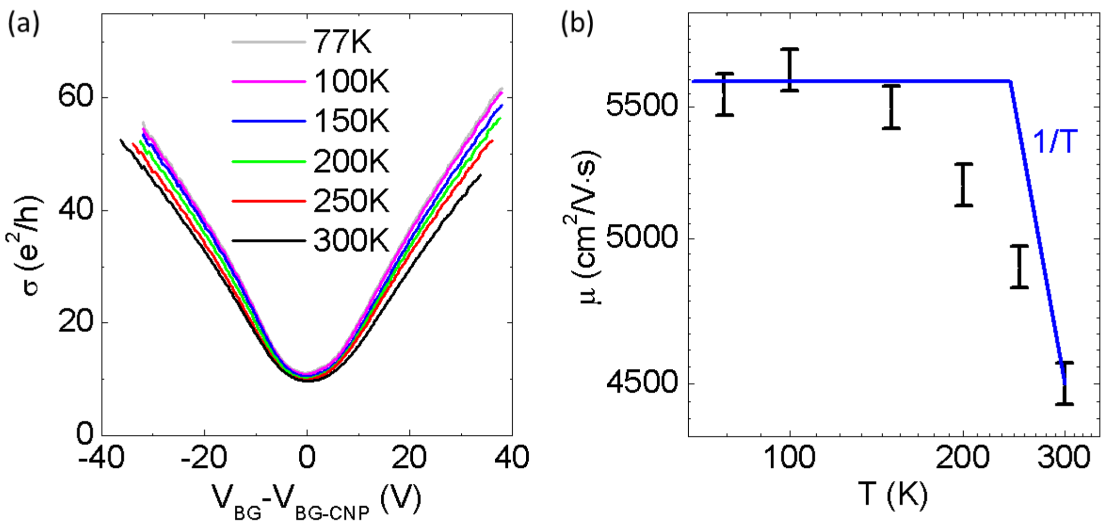

Figure 2.7: (a) σ vs. V_{BG} measured at different temperatures (T) for a graphene device with a 11 nm HfO_2 top dielectric. The V_{BG} value is offset by the back gate voltage at the charge neutrality point (V_{BG-CNP}) (b) μ vs. T for the same device. The relatively weak T-dependence suggests that phonons are not the mobility limiting factor in these devices.

2.4.2 Temperature dependence

To further investigate the scattering mechanism in graphene devices with a HfO_2 top dielectric we show in Fig. 2.7(a) σ vs. V_{BG} for a monolayer graphene with an 11 nm-thick HfO_2 top dielectric at different temperatures (T). The μ vs. T data shown in Fig. 2.7(b) shows a $\mu \propto 1/T$ dependence at higher T values, consistent with acoustic phonon scattering [33], followed by a saturation at the lowest T. These data reveal a weak temperature dependence which indicates that phonon scattering is not dominant in our devices. Since the surface roughness is not expected to change with the top dielectric

deposition, the μ vs. t_{stack} data of Fig. 2.6 combined with the μ vs. T of Fig. 2.7(b) strongly suggest that fixed charged impurities located in the high-k dielectric, and in close proximity to the graphene layer are responsible for the mobility degradation.

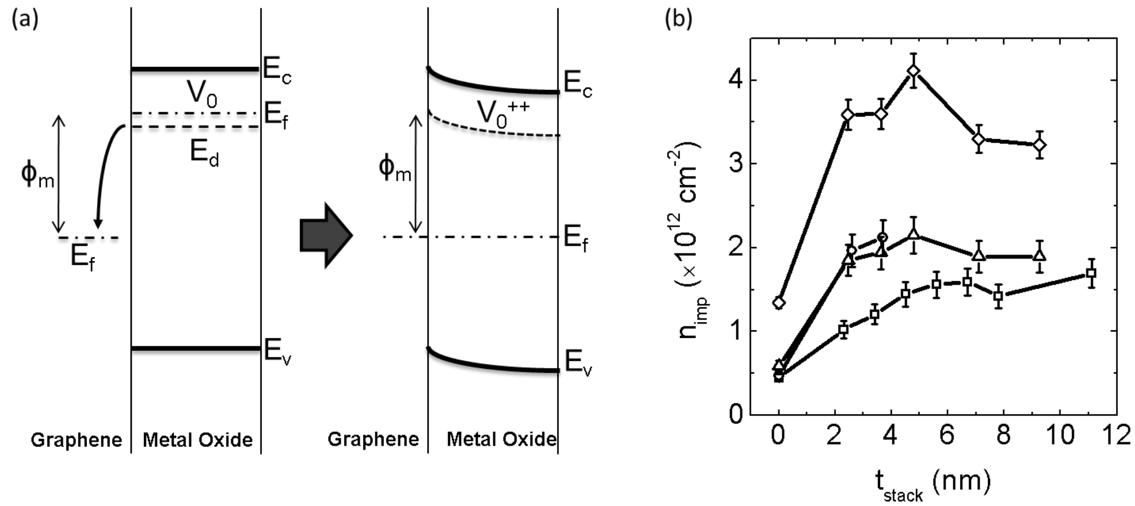

Figure 2.8: Band diagram schematic for a structure consisting of metal-oxide deposited on graphene. The oxygen vacancies, inherent for dielectrics deposited at low temperatures become ionized in the proximity of the interface, creating fixed charged impurities, which in turn reduce the mobility (Reproduced from Ref. [55]). (b) n_{imp} vs. t_{stack} data for four graphene monolayers.

2.4.3 Origin of the fixed charge impurities

Next we address the origin of these additional charged impurities that accompany the top dielectric deposition. The metal-oxide dielectrics, either Al_2O_3 or HfO_2, are deposited at room temperature or 200 °C respectively. Dielectrics deposited at low temperatures, such as the ALD process used here, are generally not stoichiometric, but oxygen deficient. We speculate that these charged impurities are point defects, such as

charged oxygen vacancies [55], [56]. Indeed, the oxygen vacancies form donor levels closer in energy to the HfO_2 conduction band, and higher than the graphene Fermi level. Similar to a metal-high-k dielectric stack [55], [56], the electrons tunnel out of the dielectric and into the graphene in order to bring in equilibrium the Fermi levels in graphene and HfO_2 [Fig. 2.8(a)], and the point defects in close proximity to the graphene layer become charged, which in turn reduces the carrier mobility.

To quantify the above argument, we employ the Boltzmann transport formalism where charged impurity screening is treated within the random phase approximation [16]. We use μ vs. t_{stack} data of Fig. 2.6 to estimate the charged impurity areal density (n_{imp}) from:

$$n_{imp} = \frac{2e}{h}\frac{1}{\mu}\frac{1}{F_l(\alpha)} \qquad (2.2)$$

where e is the electron charge, h is Planck's constant, α is the dimensionless coupling constant define by eq. 1.23:

$$\alpha = \frac{2e^2}{(k_1 + k_2)\hbar v_f}$$

v_F = 1.1×10^6 m/s is the graphene Fermi velocity, k_1 = 16 and k_2 = 3.9 are the dielectric constants of top and bottom oxides, and $F_l(\alpha)$ is given by eq. 1.25:

$$F_l(\alpha) = \pi\alpha^2 + 24\alpha^3(1-\pi\alpha) + \frac{16\alpha^3(6\alpha^2-1)\arccos(1/2\alpha)}{\sqrt{4\alpha^2-1}}$$

The stack relative dielectric constant ($k \cong 16$) is measured by adding a top metal gate and comparing the relative capacitance of the top and bottom gates as discussed in detail in section 2.5.1.

Figure 2.8(b) shows n_{imp} vs. t_{stack} for four monolayer graphene devices. These data suggest that the dielectric deposition increases the charged impurity concentration by $\cong 1.5 - 4 \times 10^{12}$ cm^{-2}. These values are in good agreement with previous studies which examined the thermochemistry of metal-oxide-semiconductor structures using HfO_2 on Si [55], [56].

2.5 Scaling of the top metal-oxide dielectric

Now we turn to the characteristics of the device type 2 where we study the scaling of the top metal-oxide dielectric in dual-gated graphene FETs.

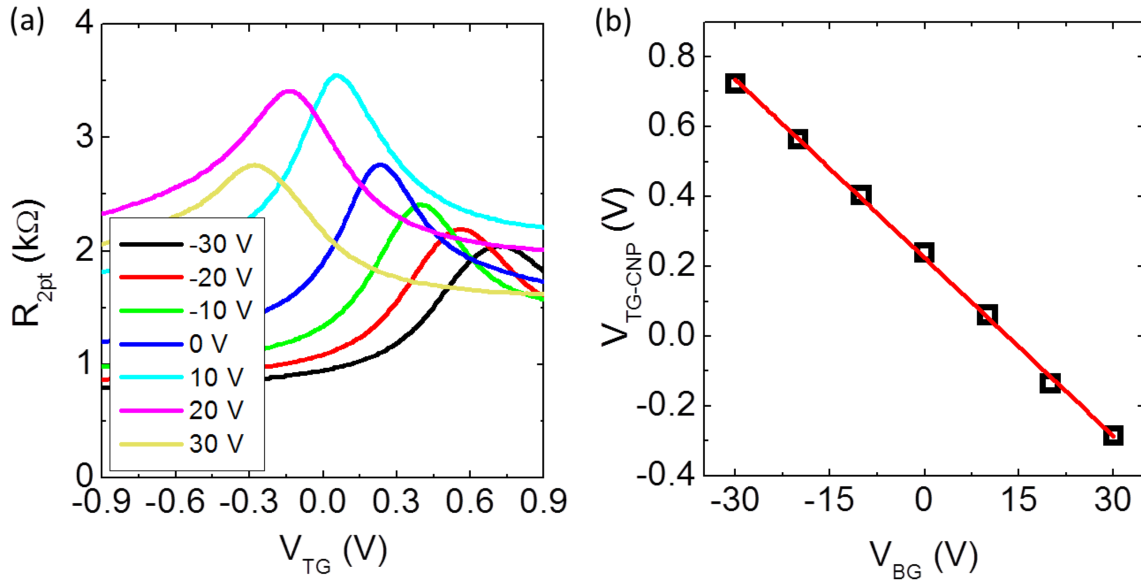

Figure 2.9: R_{2pt} vs. V_{TG} measured in a dual-gated graphene FET at different V_{BG}. The 2 nm-thick Al_2O_3 top dielectric was deposited by ALD using a 0.6 nm Ti nucleation layer. (b) V_{TG-CNP} vs. V_{BG}, measured from the R_{2pt} vs. V_{TG} traces at different back-gate biases. The C_{BG}/C_{TG} ratio is equal to the slope of the fitted line.

2.5.1 Top gate capacitance measurement

Fig. 2.9(a) shows an example of a dual-gated graphene FET resistance (R_{2pt}) measured as a function of the top gate voltage (V_{TG}), and at different back-gate voltages. The top Al_2O_3 dielectric is 2 nm-thick, and was deposited by ALD using a 0.6 nm-thick Ti nucleation layer. Each trace shows the ambipolar behavior characteristic of graphene FETs, with a charge neutrality which is back-gate dependent. The V_{TG} value at the charge neutrality point (V_{TG-CNP}) has a linear dependence on V_{BG} [Fig. 2.9(b)]. The slope of the V_{TG-CNP} vs. V_{BG} data is the ratio of the back-gate capacitance (C_{BG}) to top gate capacitance (C_{TG}). The bottom dielectric capacitance is measured using 100×100 μm^2 metal pads deposited on SiO_2 in close proximity to the graphene FETs. Using the measured C_{BG}/C_{TG} ratio and the measured value of the C_{BG}, the value of the C_{TG} is calculated for each dual-gated graphene FET. We note that the quantum capacitance does not contribute to the measured C_{TG} because the C_{BG}/C_{TG} is determined from the dependence of the charge neutrality point on V_{BG} and V_{TG}, where the Fermi energy remains zero.

2.5.2 Graphene topography after nucleation layer deposition

Figure 2.10 shows the topography of two graphene flakes probed by atomic force microscopy (AFM) after the deposition and subsequent oxidation of 1.5 nm of Al (top panel), and 0.6 nm of Ti (bottom panel). The graphene surface roughness after the Al

deposition/oxidation is 0.52 nm, compared to 0.24 nm for graphene with the oxidized Ti film. We attribute the larger surface roughness of oxidized Al on graphene to a higher surface mobility of Al [57], [58]. The surface diffusion of the metal atoms on graphene places a lower boundary on the nucleation layer thickness required for a full surface coverage, which in turn is required for the deposition of a pinhole-free top dielectric. Experimentally we find that 1.2 nm and 0.6 nm are the minimum nucleation layer thicknesses when using Al and Ti respectively. A lower nucleation layer thickness leads to severe gate leakage due to pinholes in the ALD Al_2O_3 dielectric.

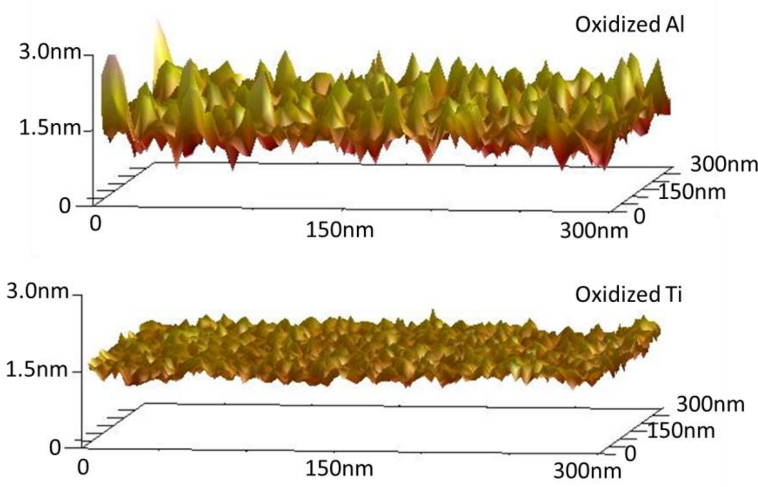

Figure 2.10: Topography of graphene flakes after the nucleation layer deposition. The top (bottom) panel represents data for a graphene flake with a 1.5 nm thick Al (0.6 nm thick Ti) film. The measured surface roughness values are 0.52 nm for Al, and 0.24 nm for Ti nucleation layers. The smoother surface of the graphene with Ti film suggests that Ti covers the entire graphene surface at a lower thickness.

2.5.3 Effect of nucleation layer on dielectric constant

Figure 2.11(a) shows C_{TG} vs. the ALD Al_2O_3 physical thickness ($t_{Al_2O_3}$). The data are extracted from multiple devices using Al and Ti nucleation layers for the Al_2O_3 ALD. We note at a given $t_{Al_2O_3}$ the C_{TG} values are higher when using Ti as a nucleation layer. Figure 2.11(b) shows the inverse of the capacitance per unit area (C_{TG}^{-1}) vs. $t_{Al_2O_3}$. For a given nucleation layer, C_{TG}^{-1} has a linear dependence on the $t_{Al_2O_3}$. The linear dependence of C_{TG}^{-1} vs. $t_{Al_2O_3}$ can be understood using a simple capacitor model [Fig. 2.11(c)], where the top dielectric stack capacitance consists of the ALD Al_2O_3 capacitance ($C_{Al_2O_3}$) in series with an interface capacitance (C_{int}):

$$C_{TG}^{-1} = C_{int}^{-1} + \frac{t_{Al_2O_3}}{k\varepsilon_0} \qquad (2.3)$$

here ε_0 is the vacuum dielectric permittivity and *k* represents the relative dielectric constant of the ALD Al_2O_3. The slope of the C_{TG}^{-1} vs. $t_{Al_2O_3}$ data yields the ALD Al_2O_3 *k*-value, and the y-axis intercept (C_{int}^{-1}) represents the interface capacitance. The extracted dielectric constant of Al_2O_3 deposited on the oxidized Al and Ti interfaces are 5.5 and 12.7, respectively, and the measured C_{int} is 1.6 ± 0.5 μF/cm2 for Al interface and 1.1 ± 0.3 μF/cm2 for the Ti interface. We note that C_{int} can originate from both the dielectric formed by the oxidized metal layer, as well as interface traps. The difference in *k*-values extracted for Al_2O_3 deposited on Al and Ti is surprising, and demonstrates that the nucleation layer plays a key role in the subsequent ALD growth of Al_2O_3 on graphene.

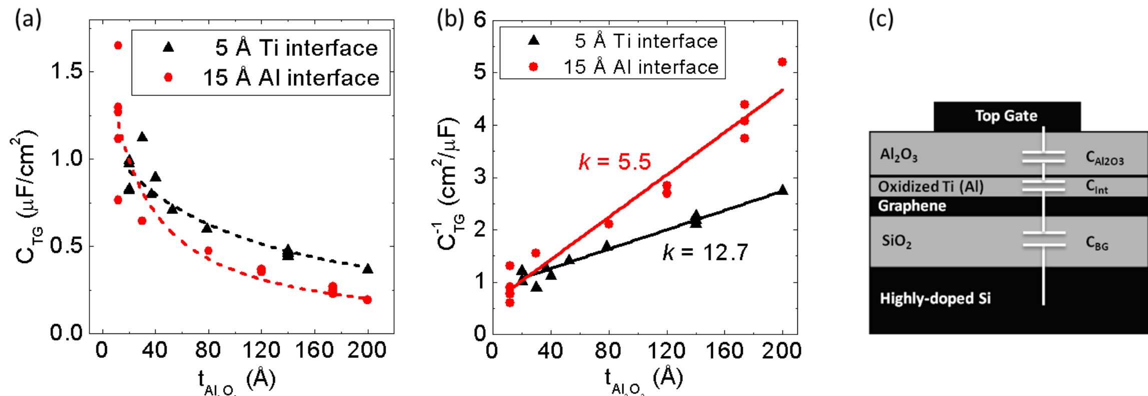

Figure 2.11: (a) C_{TG} vs. $t_{Al_2O_3}$ for dual-gated graphene FETs with Ti and Al nucleation layers (b) C_{TG}^{-1} vs. $t_{Al_2O_3}$ of same devices. For both interfacial layers, C_{TG}^{-1} has a linear dependence on $t_{Al_2O_3}$ The *k* values for ALD Al_2O_3 deposited on Ti and Al nucleation layers are 12.7 and 5.5, respectively (c) Dual-gated graphene FET schematic, with the top gate capacitance consisting of interface capacitance (C_{int}) and Al_2O_3 capacitance ($C_{Al_2O_3}$), in series.

Figure 2.12 shows the carrier mobility (μ) vs. the dielectric stack thickness (t_{Stack}) probed for three back-gated graphene FETs before and after the Ti deposition, and after the ALD Al_2O_3. The mobility is extracted from the slope of the four-point conductivity (σ) vs. V_{BG}, using eq. 2.1; and each data point is the average mobility for the two carrier types (the difference between the electron and hole mobilities is less than 10%). The data show that the nucleation layer has a smaller impact on the carrier mobility compared to the subsequent ALD Al_2O_3 which causes a more significant mobility decrease. This observation is in agreement with the data of Fig. 2.6 for HfO_2 deposited on graphene using oxidized Al as an interfacial layer. As discussed earlier, the mobility decrease is attributed to Coulomb scattering from charged point defects (e.g. oxygen vacancies) in the dielectric.

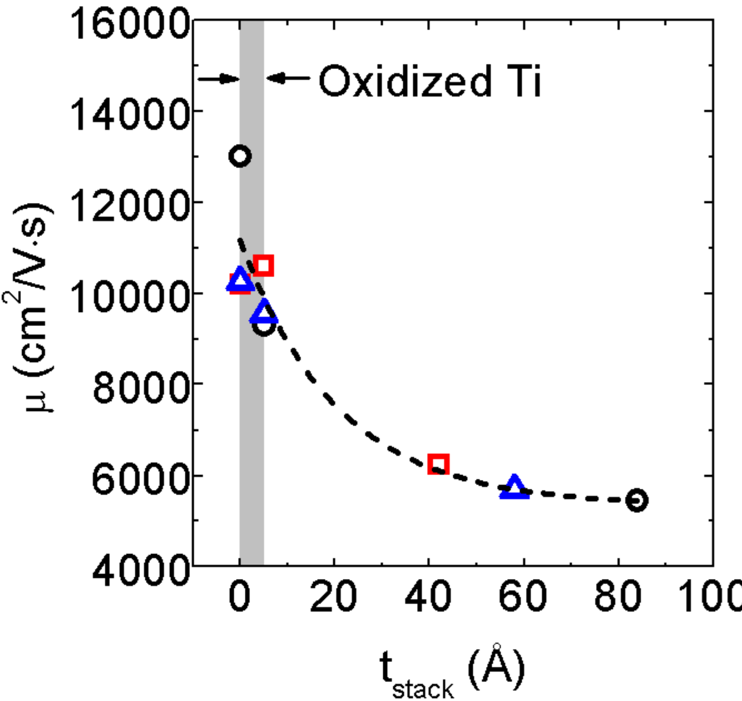

Figure 2.12: μ vs. t_{stack} for graphene FETs with the top ALD Al_2O_3 dielectric deposited on Ti. The shaded area represents the interfacial layer thickness. The dashed line is a guide to the eye.

2.5.4 Al_2O_3 structure

To explore the origin of the Al_2O_3 dielectric constant dependence on the nucleation layer, we analyzed the dielectric structure using TEM, and electron energy loss spectroscopy (EELS). Figure 2.13 shows the TEM cross section of two samples, consisting of the ALD Al_2O_3 deposited on graphene using Al [Fig. 2.13(a)] and Ti [Fig. 2.13(b)] nucleation layers. A comparison of the Al_2O_3 structure in Fig. 2.13(a) and Fig. 2.13 (b) reveals that the Al_2O_3 grown on Ti has crystalline regions. Although the Al_2O_3

film is not fully crystalline, it does show long range order by comparison to the Al_2O_3 grown on Al, which is amorphous. The inset of Fig. 2.13(b) shows the Fourier transform of an Al_2O_3 grain in film deposited on Ti nucleation layer, confirming the partially crystalline structure. Figures 2.13(c,d) show the composition maps [panel (c)] and line-scan [panel (d)] of O, C, Ti, and Al determined from EELS measurements for an Al_2O_3 film grown on graphene using a Ti interface. The data indicates that Ti does not diffuse into the ALD Al_2O_3 dielectric during the growth. Figure 2.13 data therefore suggests that the difference in the dielectric constants of Al_2O_3 deposited using Al and Ti nucleation layers, stems primarily from the dielectric crystal structure, with the Al_2O_3 being partially crystalline when grown on oxidized Ti, and amorphous when grown on oxidized Al. The higher dielectric constant of Al_2O_3 grown on oxidized Ti is in agreement with previous studies correlating the dielectric constant and crystal structure for Al_2O_3 [59]. Further studies are required to clarify crystallization mechanism for the ALD of Al_2O_3 on the oxidized Ti interfacial layer.

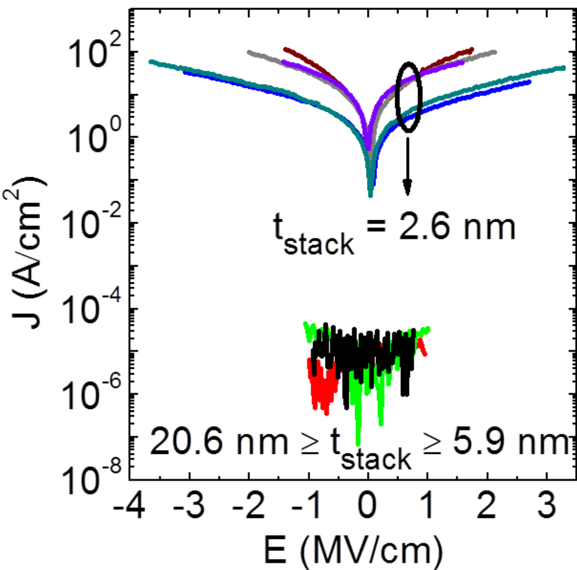

Figure 2.13: Leakage current density (J) as a function of vertical electric field (E) for different top dielectric thicknesses. The gate resistance for devices with 2.6 nm top dielectric stack is ~1 MΩ.

The top gate leakage current density (J) versus the electric field (E-field) is shown in Fig. 2.13, for different stack thicknesses. The measured gate resistance of devices with the thinnest top-gate dielectric, 0.6 nm oxidized Ti followed by 2 nm Al_2O_3 is ~1 MΩ. The leakage current density for devices with stack thicknesses of 6 nm or more are less than 10^{-5} A/cm^{-2}.

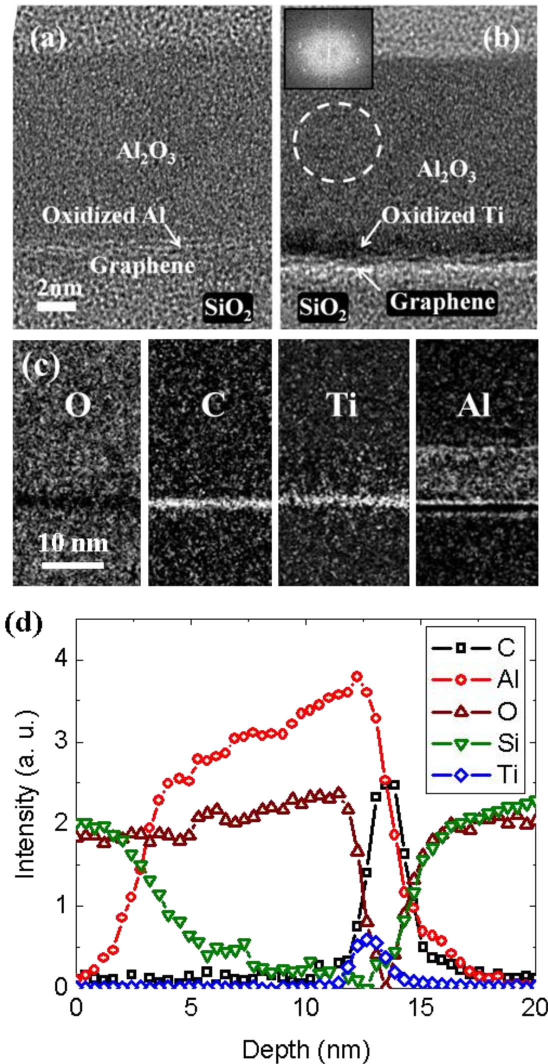

Figure 2.14: TEM cross section micrographs of ALD Al_2O_3 on graphene, grown using Al (a), and Ti (b) nucleation layers. Panel (b) inset: Fast Fourier Transform corresponding to the grain marked by the dashed line. (c) Compositional maps of oxygen, carbon, titanium, and aluminum determined from EELS measurements on an Al_2O_3/TiO_x/graphene stack. (d) Concentration profiles of C (K-edge), Al (L-edge), O (K-edge), Si (L-edge), and Ti (L-edge) obtained from EELS line scans of Al_2O_3/TiO_x/graphene stack.

2.6 SUMMARY

In summary, we studied the monolayer and bilayer graphene mobility dependence on the thickness of a top high-*k* metal-oxide dielectric as well as the thickness scaling of ALD Al_2O_3 dielectric in graphene FETs, using oxidized Al and Ti nucleation layers. We show graphene mobility decreases after 2-4nm metal-oxide dielectric deposition and remains constant if the dielectric thickness is further increased. The mobility temperature dependence suggests that phonons are not the dominant scattering mechanism in these devices, indicating that additional charged impurities located in close proximity to the graphene layer are introduced during dielectric deposition. We speculate that positively charged oxygen vacancies, ubiquitous in high-k dielectrics, are the mobility limiting factor in our devices.

We also show the smooth surface of thermally evaporated Ti on graphene provides excellent surface coverage at thicknesses as low as 0.6 nm which enables the realization of graphene FETs with ultra-thin top gate dielectrics. The nucleation layer has a significant impact on the dielectric constant and morphology of the subsequently grown ALD dielectric. TEM analysis reveals that the ALD of Al_2O_3 on graphene using an Al nucleation layer yields an amorphous film, whereas the Ti nucleation layer yields a partially crystalline film.

CHAPTER 3: RESONANT TUNNELING IN DOUBLE BILAYER GRAPHENE HETEROSTRUCTURES

In this chapter, we demonstrate gate-tunable resonant tunneling and negative differential resistance in the interlayer current-voltage characteristics of rotationally aligned double bilayer graphene heterostructures separated by hexagonal boron-nitride (hBN) dielectric. An analysis of the heterostructure band alignment using individual layer densities, along with experimentally determined layer chemical potentials indicates that the resonance occurs when the energy bands of the two bilayer graphene are aligned. We discuss the tunneling resistance and interlayer dielectric capacitance dependence on the interlayer hBN thickness, as well as the resonance width dependence on mobility, rotational alignment, and in-plane magnetic field.

3.1 2D-2D RESONANT TUNNELING

Tunneling between two distinct two-dimensional (2D) carrier systems, namely 2D-2D tunneling has been used in GaAs 2D electron [60], [61] and 2D hole systems [62]–[64] as a technique to probe the Fermi surface and quasi-particle lifetime. Figure 3.1(a) shows schematic view of a dual-gated GaAs/AlGaAs heterostructure with carriers being confined in two parallel 2D GaAs quantum wells [65]. In this device, carriers can move from one layer to another by tunneling through the AlGaAs tunnel barrier. The tunneling current is greatly enhanced when the energy and momentum of the carriers are conserved during the tunneling. Figures 3.1(b-d) illustrate various possible scenarios

regarding the relative alignment of the two GaAs quantum well energy bands and chemical potentials (μ) [66]. When the bottom of the energy bands of two quantum wells are not energetically aligned [Fig. 3.1(b)], the carrier tunneling between two layers is negligible because the energy and momentum conservation cannot be satisfied simultaneously. By applying a sufficiently large gate voltage, while two layers are at the same potential (e.g. grounded), one can bring the bottom of the conduction bands of two layers in alignment [Fig. 3.1(c)], however, the alignment of the chemical potentials leads to zero tunneling current between two layers. Fig. 3.1(d) shows the condition at which the bottom of conduction bands are brought in alignment by applying an interlayer voltage (V_{int}) between two layers at fixed gate voltages. Here, carriers at energy states between top and bottom layer chemical potentials (μ_T, μ_B) can tunnel between two layers while their energy and momentum are both conserved. Figure 3.1(e) shows the interlayer current-voltage characteristics of the device shown in Fig. 3.1(a) measured at T = 0.3 K. The momentum conserving tunneling between two layers leads to a gate-tunable resonantly enhanced tunneling conductivity and negative differential resistance (NDR).

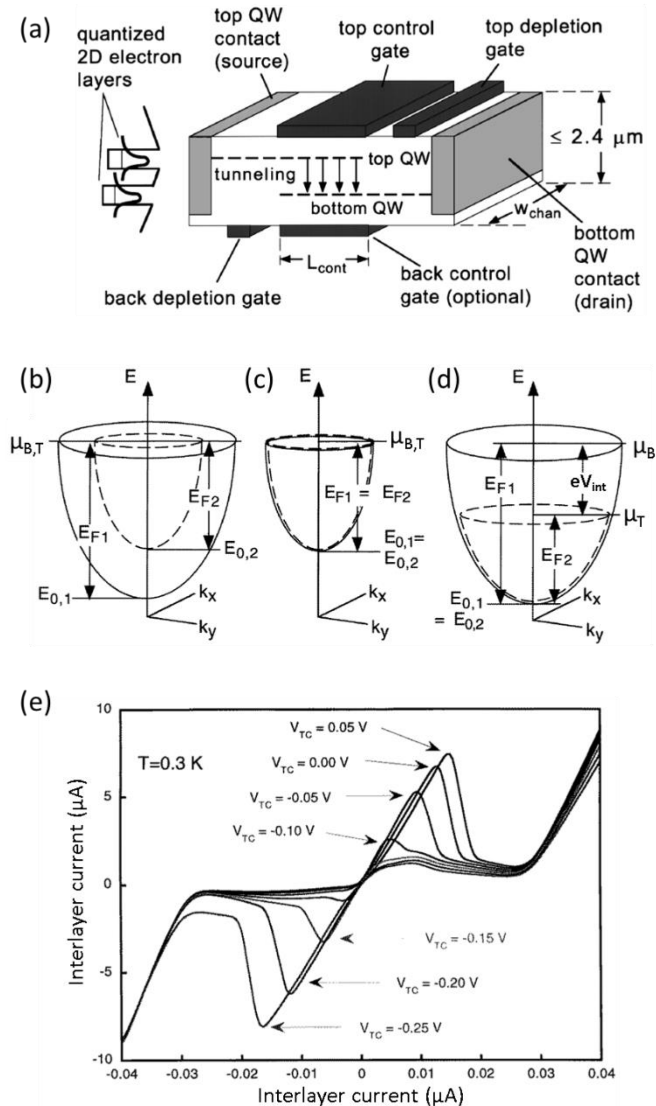

Figure 3.1: (a) Schematic of a dual-gated double quantum well tunneling transistor based on GaAs/AlGaAs heterostructure. The individual quantum wells are independently contacted. A sketch of the energy band diagram is shown at left. The energy-momentum dispersion of two layers when (b) energetically misaligned (c) energetically aligned with identical carrier density (d) energetically aligned with different carrier densities. (e) Interlayer current-voltage characteristics showing gate-tunable resonant tunneling and NDR (Figures and captions adapted from refs. [65], [66]).

3.1.1 2D-2D tunneling formalism

In this section, we consider a system of two parallel two-dimensional electron gases (2DEGs) vertically stacked on top of each other and separated by a tunnel barrier and derive expressions for its interlayer current (I_{int}) and differential conductance (G) as a function of interlayer voltage (V_{int}). We first go over the basics of the energy bands in a 2D-2D system. Figure 3.2 shows a simplified schematic view of the energy bands in a 2D-2D system where E_{B0} (E_{T0}) corresponds to the bottom of the first energy sub-band in bottom (top) layer, μ_B (μ_T) is the chemical potential in bottom (top) layer, and E_{FB} (E_{FT}) is bottom (top) Fermi energy:

$$E_{FB} = \mu_B - E_{B0} \qquad (3.1)$$

$$E_{FT} = \mu_T - E_{T0} \qquad (3.2)$$

Assuming the electrostatic potential drop across the dielectric layer is V_{ES} then:

$$E_{T0} - E_{B0} = e \cdot V_{ES} \qquad (3.3)$$

The separation of the chemical potentials in the two layers is defined by the applied interlayer voltage:

$$\mu_T - \mu_B = eV_{int} \qquad (3.4)$$

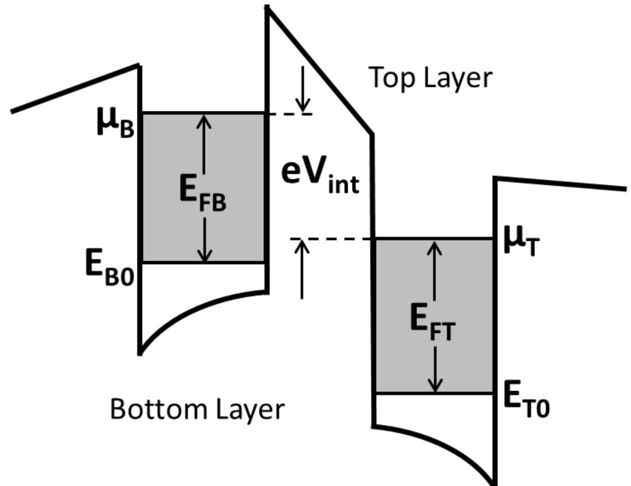

Figure 3.2: Conduction band of two 2DEGs. μ_B (μ_T) is the chemical potential in bottom (top) layer and E_{B0} (E_{T0}) is the conduction band edge energy of bottom (top) layer.

The Hamiltonian of a 2D-2D system (H) can be written as [67]:

$$H = H_T + H_B + H_T \qquad (3.5)$$

where H_T and H_B are the Hamiltonian for electrons in the top and bottom layers, respectively, and H_T is the tunneling Hamiltonian:

$$H_T = -\sum_{\boldsymbol{k},\boldsymbol{k}'}\left(t_{\boldsymbol{k},\boldsymbol{k}'}c^{\dagger}_{\boldsymbol{k},T}c_{\boldsymbol{k}',B} + H.c.\right) \qquad (3.6)$$

$t_{\boldsymbol{k},\boldsymbol{k}'}$ is the tunneling matrix element and c and $c^{\dagger}$ are the creation and annihilation operators, respectively. Term $t_{\boldsymbol{k},\boldsymbol{k}'}$ in a 2D-2D system with a tunneling barrier that is invariant under translations perpendicular to the barrier is zero for $\boldsymbol{k} \neq \boldsymbol{k}'$ therefore

$t_{\boldsymbol{k},\boldsymbol{k}'} = t\delta_{\boldsymbol{k},\boldsymbol{k}'}$. The tunneling current in a 2D-2D system calculated using Kobu formalism has the form:

$$I_{int} = \frac{2e}{\hbar} t^2 S \int \frac{d^2k}{(2\pi)^2} \int_{-E_F}^{\infty} \frac{dE}{2\pi} A(E, \boldsymbol{k}) A(E + eV_{int}, \boldsymbol{k})[f(E) - f(E + eV_{int})] \quad (3.7)$$

where S is the tunneling area, $f(E)$ is the Fermi distribution function, and $A(E, \boldsymbol{k})$ is the spectral function of electrons in top and bottom 2DEGs at zero magnetic field given by:

$$A(E, \boldsymbol{k}) = \frac{1}{\Gamma_{T,B}^2 + \left(\frac{\hbar^2 k^2}{2m^*} - E\right)^2} \quad (3.8)$$

here $\Gamma_{T,B} = \hbar/2\tau_{T,B}$ is the broadening associated with the scattering time $\tau_{T,B}$ in top and bottom layers and m^* is the carrier effective mass. The integral of eq. 3.7 with the assumptions of low temperature ($k_B T \ll \Gamma$) and weak disorder ($\Gamma \ll E_F$) yields:

$$I_{int} = St^2 \frac{2e}{\hbar} \frac{m^*}{\pi\hbar^2} \frac{\Gamma}{\Gamma^2 + (eV_{int} + \mu_T - \mu_B)^2} V_{int} \quad (3.9)$$

here $\Gamma = \Gamma_B + \Gamma_T$. It is customary to present the tunneling data in terms of differential conductance defined as $G = dI/dV_{int}$. The general form of the differential conductance valid for all V_{int} values is [67], [68]:

$$G\,(V_{int}) = St^2 \frac{2e}{\hbar} \frac{m^*}{\pi\hbar^2} \Gamma \frac{\Gamma^2 - (eV_{int})^2 + (\mu_T - \mu_B)^2}{[\Gamma^2 + (eV_{int} + \mu_T - \mu_B)^2]^2} \quad (3.10)$$

Figure 3.3 shows an example of G vs. V_{int} measured in a 2D-2D electron system at temperatures ranging between T = 0.47 K and T = 9.1 K and with equal carrier densities in both layers ($n = 1.6 \times 10^{11}$ cm^{-2}).

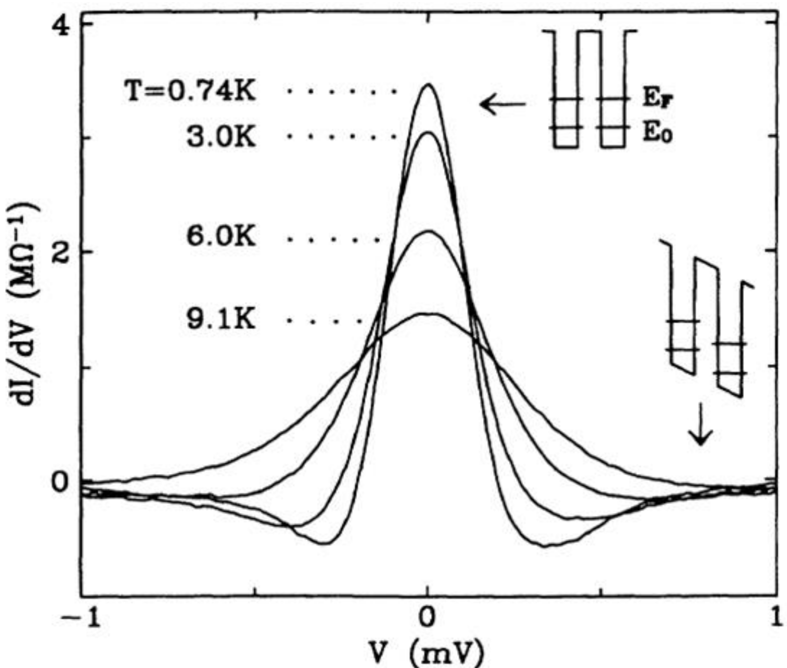

Figure 3.3: G vs. V_{int} of a 2D-2D electron system measured at various temperatures in a sample with equal carrier densities in both top and bottom layers ($n = 1.6 \times 10^{11}$ cm^{-2}). Insets show the energy band alignment at resonance and off resonance (Figure and caption adapted from Ref. [69]).

3.2 2D-2D TUNNELING IN DOUBLE BILAYER GRAPHENE HETEROSTRUCTURES

3.2.1 Van der Waals heterostructures

Recent progress in realization of atomically thin heterostructures by stacking 2D atomic crystals, such as graphene, hexagonal boron nitride (hBN), and transition metal

dichalcogenides (TMDs) has provided a versatile platform to probe new physical phenomena, and explore novel device functionalities [70], [71]. Combining such materials in vertical heterostructures may provide new insight into the electron physics in these materials through Coulomb drag [72], [73] or tunneling [74], [75].

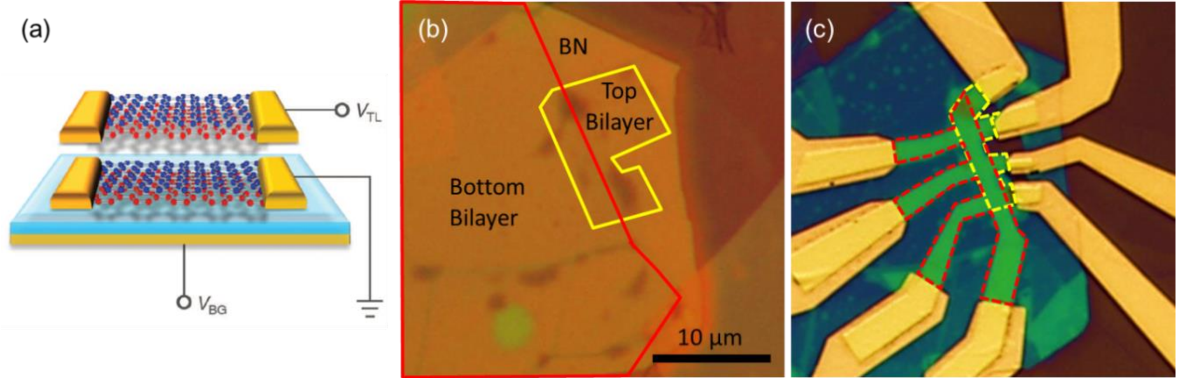

Figure 3.4: (a) Schematic of the double bilayer graphene device. (b) Optical micrograph of the top and bottom graphene flakes illustrating the alignment of straight edges. The red (yellow) lines mark the boundaries of the bottom (top) bilayer graphene. (c) Optical micrograph of the device. The red (yellow) dashed lines mark the bottom (top) bilayer graphene.

The emergence of single or few atom-thick semiconductors, such as graphene and TMDs can open new routes to probe 2D-2D tunneling in their heterostructures, which in turn may enable new device applications [74], [76], [77]. While fascinating, resonant tunneling between two graphene or TMD layers realized using a layer-by-layer transfer approach is experimentally challenging because the energy band minima are located at the K points in the first Brillouin zone, and the large K-point momenta coupled with small rotational misalignment between the layers can readily obscure resonant tunneling.

Bilayer graphene, as discussed in the first chapter, consists of two monolayer graphene in A-B stacking, and has a hyperbolic energy-momentum dispersion with a tunable bandgap [8], [78], [79]. Hexagonal boron-nitride is an insulator with an energy gap of 5.8 eV [80] and dielectric strength of 0.8 V/nm [81], which has emerged as the dielectric of choice for graphene [70] thanks to its atomically flat, and chemically inert surface. We demonstrate here resonant tunneling and NDR between two bilayer graphene flakes separated by an hBN dielectric. A detailed analysis of the band alignment in the heterostructure indicates that the NDR occurs when the charge neutrality points of the two layers are energetically aligned, suggesting momentum conserving tunneling is the mechanism responsible for the resonant tunneling.

3.2.2 Realization of double bilayer graphene heterostructures

Figure 3.4(a) shows a schematic representation of our double bilayer heterostructure devices, consisting of two bilayer graphene flakes separated by a thin hBN layer. The devices are fabricated through a sequence of bilayer graphene and hBN mechanical exfoliation, alignment, dry transfers/layer pick-ups, e-beam lithography, and plasma etching steps similar to the techniques reported in Refs. [70], [82]–[84].

3.2.2.1 *Fabrication: dry layer transfer method*

In this method, devices are fabricated using the dry transfer technique described in ref. [83]. The device fabrication starts with mechanical exfoliation of bilayer graphene and hBN on SiO_2/Si substrate. Then, we spin coat poly-propylene carbonate (PPC) on a 1

mm-thick Polydimethylsiloxane (PDMS) film bonded to a thin glass slide. The glass/PDMS/PPC stack is used to pick up the top bilayer graphene, the thin interlayer hBN (t_{hBN} = 1.2 nm), and the bottom bilayer graphene consecutively from SiO_2/Si substrates using the Van der Waals force between the two-dimensional crystals. The entire stack is transferred onto an hBN flake previously exfoliated on SiO_2/Si substrate. Figure 3.4(b) shows the transferred stack on top of bottom hBN/SiO_2/Si substrate. After dissolving the PPC, a sequence of EBL, O_2 and CHF_3 plasma etching is used to define the active area. Finally, the metal contacts are defined by EBL, e-beam evaporation of Ti-Au, and lift-off [Fig. 3.4(c)].

3.2.2.2 *Fabrication: layer pickup method*

In this method, similar to the dry layer transfer method, the fabrication starts with exfoliation of hBN on a silicon wafer covered with 285 nm-thick thermally grown SiO_2. Topography and thickness of the exfoliated hBN flakes are measured with atomic force microscopy (AFM), and flakes with minimum surface roughness and surface contamination are selected. On a separate silicon wafer covered with water soluble Polyvinyl Alchohol (PVA) and Poly(Methyl Methacrylate) (PMMA), bilayer graphene is mechanically exfoliated from natural graphite and identified using optical contrast and Raman spectroscopy. The PVA is dissolved in water, and the PMMA/bilayer graphene stack is transferred onto hBN flake using a thin glass slide [Fig. 3.5(a)]. The PMMA film is then dissolved in acetone and the bilayer graphene is trimmed using EBL and O_2 plasma etching [Fig. 3.5(b)]. Similarly, a thin hBN (t_{hBN} = 1.2-1.8 nm) flake exfoliated on

a PMMA/PVA/Si substrate is transferred onto the existing bilayer graphene [Fig. 3.5(c)]. A second bilayer graphene is transferred onto the stack [Fig. 3.5(d)], and trimmed on top of the bottom bilayer graphene using EBL and O_2 plasma etching [Fig. 3.5(e)]. Finally, metal contacts to both top and bottom bilayer graphene are defined through EBL, electron-beam evaporation of Ni and Au, and lift-off [Fig. 3.5(f)].

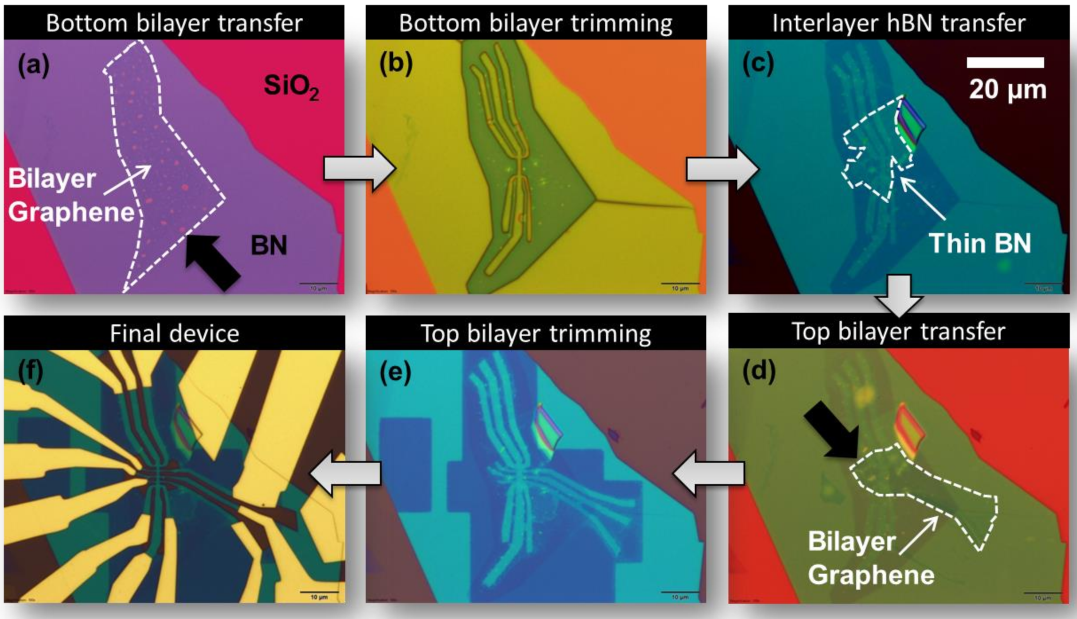

Figure 3.5: Fabrication of back-gated double bilayer graphene heterostructure using dry transfer technique. (a) Transfer of bottom bilayer graphene onto bottom hBN. (b) Trimming of bottom bilayer in O_2 plasma using PMMA mask. (c) transfer of thin interlayer hBN flake. (d) Transfer of top bilayer graphene. (e) Trimming of top bilayer in O_2 plasma using PMMA mask. (f) Final device after definition of metal contacts. The black arrows in panels (a) and (d) point to the reference straight edges used for the alignment of the two layers.

Device	Top bilayer mobility (cm^2/V·s)	Bottom bilayer mobility (cm^2/V·s)	Interlayer hBN thickness (# of monolayers)	C_{int} (μm/cm^2)	C_{BG} (nF/cm^2)	Optical image
#1	3,500	150,000-160,000	6	1.02	10.5	5 μm
#2	14,800	2,400	5	1.23	12.9	10 μm
#3	-	-	4	-	-	10 μm
#4	13,800	150,000	4	1.55	10.5	10 μm

Table 3.1: List of the key devices presented in this chapter.

3.2.2.3 *Rotational alignment*

The bilayer graphene flakes selected for the device fabrication have at least one straight edge which is used as a reference to align the crystalline orientation of the bottom and top bilayer graphene during the transfer [Figs. 3.4(b) and 3.5(a,d)]. The accuracy of the rotational alignment is mainly limited by the size of the flakes, and the resolution of the optical microscope. For a typical length of the bilayer graphene straight edge of 10 – 20 μm, we estimate the rotational misalignment between the two bilayers in our devices to be less than 3 degrees. The interlayer hBN straight edges are not intentionally aligned with either the top or bottom graphene layers during transfers.

3.2.2.4 *Tunnel junction uniformity*

The interface between various materials in an atomically thin heterostructure plays a key role in device quality and tunneling uniformity. Particularly, the presence of contaminants, such as tape or resist residues, and wrinkles in the tunneling region and in between the layers changes the interlayer spacing and the local carrier density, which in turn makes the tunneling current distribution non-uniform. To achieve an atomically flat interface with minimum contamination, the heterostructure is annealed either after each transfer or after the stack completion in high vacuum (10^{-6} Torr), at a temperature T = 340°C for 8 hours. Figures 3.4(c) and 3.5(f) depict the optical micrograph of the final devices. In Fig. 3.4(c) the bottom and top bilayer graphene boundaries are marked by red and yellow dashed lines; the interlayer hBN is not visible in this micrograph.

3.3 ELECTRICAL CHARACTERIZATION

The devices are characterized at temperatures ranging from T = 1.4 K to room temperature, using small signal, low frequency lock-in techniques to probe the individual layer resistivities, and a parameter analyzer for the interlayer current-voltage characteristics. Nine devices were fabricated and investigated in this study; we focus here on data from four devices, labelled #1, #2, #3, and #4. Device #1 consists of the double bilayer heterostructure separated by hBN where the top layer is exposed to ambient, while Devices #2 to #4 have the top layer capped with an additional hBN layer. Table 3.1 shows the optical images of the devices as well as a summary of their key parameters.

3.3.1 Layer resistivity measurement

To characterize the double bilayer system, it is instructive to start with the characteristics of the individual layers. The device layout allows us to independently probe the bottom and top–layer resistivites (ρ_B, ρ_T), and carrier densities (n_B, n_T) in the overlap (tunneling) region as a function of the back-gate (V_{BG}) and interlayer bias (V_{TL}) applied on the top layer; the bottom layer potential is kept at ground during all measurements. Figure 3.6 shows the bottom (panel a) and top (panel b) layer resistivity measured as a function of V_{BG} and V_{TL} in Device #1, at T = 1.4 K. The carrier mobility of Device #1 measured from the four-point conductivity is 150,000 - 160,000 $cm^2/V \cdot s$ for the bottom bilayer and 3,500 $cm^2/V \cdot s$ for the top bilayer at T = 1.4 K. The data of Fig. 3.6 indicate that the combination of gate biases at which both bilayer graphene are charge

neutral, namely the double charge neutrality point (DNP), is: V_{BG-DNP} = 20.2 V and V_{TL-DNP} = -0.235 V.

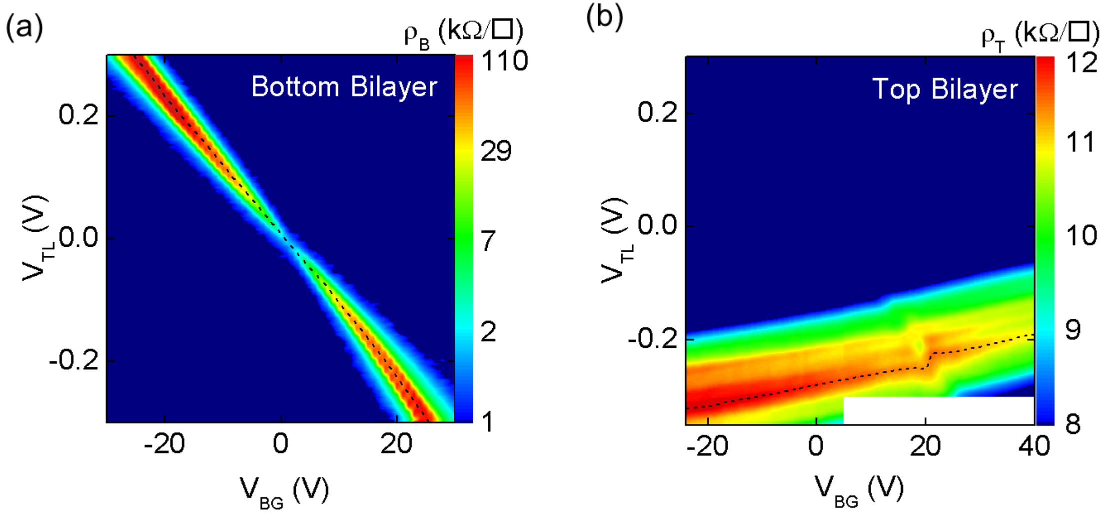

Figure 3.6: Device #1 bottom [panel (a)] and top [panel (b)] bilayer graphene resistivity contour plots measured as a function of V_{BG} and V_{TL} at T = 1.4 K. The charge neutrality points in both panels are marked by black dashed lines.

3.3.2 Capacitances and chemical potential measurement

At a given set of V_{BG} and V_{TL}, the values of n_B and n_T can be calculated using the following equations [85]:

$$e(V_{BG} - V_{BG-DNP}) = \frac{e^2(n_B + n_T)}{C_{BG}} + \mu_B \qquad (3.11)$$

$$e(V_{TL} - V_{TL-DNP}) = -\frac{e^2 n_T}{C_{int}} + \mu_B - \mu_T \qquad (3.12)$$

Here e is the electron charge, C_{BG} is the back-gate capacitance, C_{int} is the interlayer dielectric capacitance, μ_T and μ_B are the top and bottom bilayer graphene chemical potential measured with respect to the charge neutrality point, respectively. Solving eqs. 3.11 and 3.12 yields a one-to-one correspondence between the applied biases and the layer densities. Finding a self-consistent solution for eqs. 3.11 and 3.12 requires the C_{BG} and C_{int} values, and the layer chemical potential dependence on carrier density. We discuss in the following an experimental method to determine the capacitance values in a double bilayer graphene, along with the chemical potential dependence on the carrier density.

Along the charge neutrality line (CNL) of the top bilayer graphene [i.e. $n_T = \mu_T = 0$], eq. 3.12 reduces to $\mu_B = e(V_{TL} - V_{TL-DNP})$, thus the μ_B value at a given V_{BG} can be determined along the top layer CNL. To determine the value of the C_{BG}, we measure ρ_B and ρ_T of the device in a perpendicular magnetic field. Figure 3.7(a) presents the ρ_T contour plot of Device #1 measured as a function of V_{BG} and V_{TL}, in a perpendicular magnetic field B = 13 T, and at T = 1.5 K. The charge neutrality line of the top bilayer graphene [dashed line in Fig. 3.7(a)] shows a staircase behavior, which stems from the bottom bilayer graphene chemical potential crossing the Landau levels (LLs) [82]. At a given LL filling factor (ν), marked in Fig. 3.7(a), the bottom bilayer graphene carrier density is $n_B = \nu eB/h$; h is the Planck constant. Writing eqs. 3.11 and 3.12 along the top bilayer CNL, combined with $n_B = \nu eB/h$ yields:

$$C_{BG} = \frac{e^2 B}{h}\left(\frac{\Delta(V_{BG} - V_{TL})}{\Delta\nu}\right)^{-1} \qquad (3.13)$$

Where $\Delta(V_{BG} - V_{TL})$ is the change in $V_{BG} - V_{TL}$ corresponding to a bottom bilayer filling factor change $\Delta\nu$ along the top layer CNL [dashed line in Fig. 3.7(a)]. Figure 3.7(b) shows a clear linear dependence of $V_{BG} - V_{TL}$ vs. ν, marked by circles in Fig. 3.7(a). The slope of $V_{BG} - V_{TL}$ vs. ν data along with eq. 3.13 yields C_{BG} = 10.5 nF/cm^2 for Device #1, corresponding to 285 nm-thick SiO_2 in series with 40 nm-thick hBN dielectric.

The n_B value along the top bilayer CNL can be calculated using eqs. 3.11 and 3.12:

$$n_B = \frac{C_{BG}}{e} \cdot [(V_{BG} - V_{BG-DNP}) - (V_{TL} - V_{TL-DNP})] \qquad (3.14)$$

Combining the μ_B values determined along the top layer CNL of Fig. 3.6(b), with eq. 3.14 yields μ_B vs. n_B. Figure 3.8 shows μ_B vs. n_B for Devices #1 and #4. We note that in addition to the layer densities the applied V_{BG} and V_{TL} also change the transverse electric fields across the two layers (discussed later in this chapter). The chemical potential of the two devices match well at high carrier densities, but differ near $n_B = 0$ thanks to different transverse electric fields values across the bottom layer near the DNP [8]. Because the experimental data show the bilayer graphene chemical potential is weakly dependent on the transverse electric fields away from the neutrality point, and to simplify the solution of eqs. 3.11 and 3.12 we neglect the μ_T and μ_B dependence on the transverse electric field across the individual layers. By fitting a polynomial of degree five to the

experimental μ_B vs. n_B data of Fig. 3.8 we find an expression for the μ vs. n that will be subsequently used to solve eqs. 3.11 and 3.12. Table 3.2 shows the coefficients of the fitted polynomial:

$$\mu(n) = a_0 + a_1 \cdot n + a_2 \cdot n^2 + a_3 \cdot n^3 + a_4 \cdot n^4 + a_5 \cdot n^5 \qquad (3.11)$$

Coefficient	Value
a_0	-0.0006213 eV
a_1	3.660×10^{-2} eV·cm^2
a_2	1.513×10^{-3} eV·cm^2
a_3	-1.187×10^{-3} eV·cm^2
a_4	-3.093×10^{-5} eV·cm^2
a_5	3.999×10^{-5} eV·cm^2

Table 3.2: Fitting parameter values obtained by fitting a polynomial of degree five to the μ vs. n data of Fig. 3.8.

In eq. 3.11, n is in units of 10^{12} cm^{-2}. The dashed line in the Fig. 3.8 depicts the polynomial fit to the experimental μ_B vs. n data, which will be subsequently used to solve eqs. 3.11 and 3.12.

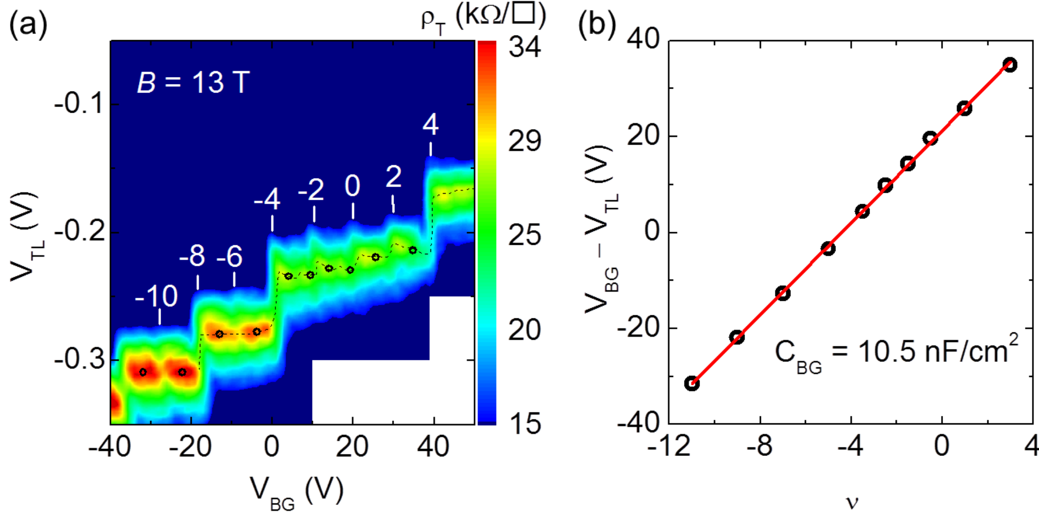

Figure 3.7: Capacitance and chemical potential measurement in device #1 (a) Contour plot of ρ_T measured as a function of V_{BG} and V_{TL}, at B = 13 T and T = 1.5 K in Device #1. The bottom bilayer graphene LL filling factors are marked. (b) $V_{BG} - V_{TL}$ vs. ν of the bottom bilayer showing a linear dependence; the C_{BG} value is determined from the slope.

We now turn to the extraction of the C_{int} value. Let us consider the bottom bilayer graphene CNL, marked by a dashed line in Fig. 3.6(a). In a dual gated graphene device with metallic gates, the value of the top-gate capacitance can be readily extracted from the linear shift of the bottom graphene charge neutrality point with back-gate and top-gate voltages [37], which yields the top-gate to back-gate capacitance ratio. Because the top layer is not a perfect metal, using the slope of the bottom bilayer CNL of Fig. 3.6(a) to calculate C_{int} neglects the contribution of the top bilayer quantum capacitance. Combining eqs. 3.11 and 3.12 along the bottom bilayer CNL, i.e. $n_B = \mu_B = 0$, we obtain the following expression that includes the quantum capacitance:

$$C_{int} = -\frac{eC_{BG}\cdot(V_{BG}-V_{BG-DNP})}{e(V_{TL}-V_{TL-DNP})+\mu_T(C_{BG}\cdot(V_{BG}-V_{BG-DNP})/e)} \qquad (3.15)$$

Using eq. 3.15 and the μ_T vs. n dependence of Fig. 3.8, we determine an interlayer dielectric capacitance of C_{int} = 1.02 μF/cm^2 for Device #1. The C_{int} values for Devices #2, and #4 are 1.23 μF/cm^2, and 1.55 μF/cm^2, respectively.

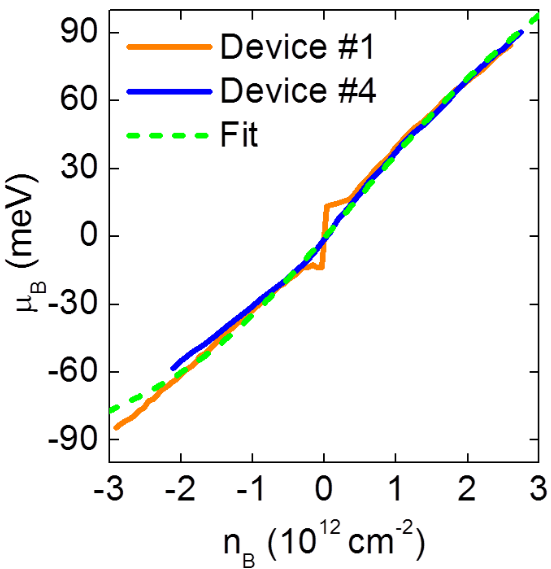

Figure 3.8: μ_B vs. n_B for Devices #1 and #4. The dashed line is the polynomial fit to the experimental data.

3.3.3 Interlayer current-voltage characteristics

Now we turn to the interlayer current (I_{int}) - voltage characteristics of our devices. Figure 3.9(a) shows the I_{int} vs. V_{TL} for Device #1 measured at various V_{BG}

values, and at T = 10 K. For small bias values, I_{int} increases monotonically with V_{TL}, corresponding to an interlayer resistance of 39 GΩ·μm^2. For V_{BG} values ranging from 10 V to 30 V, the interlayer current-voltage traces show a marked resonance and NDR, which depend on the applied V_{BG}. Figure 3.9(b,c) present the I_{int} vs. V_{TL} of Devices #2 and #3 measured at room temperature. The normalized interlayer resistance of Devices #2 and #3 at the limit of V_{TL} = 0 V is 1 GΩ·μm^2 and 0.3 GΩ·μm^2, respectively. Similar to the Device #1 data, we observe resonant tunneling and NDR in the interlayer current-voltage characteristics of Devices #2 and #3. A distinct difference between Devices #2 and #3 and the first device is that the resonance is centered around V_{TL} = 0 V in Devices #2 and #3 by comparison to Device #1. As we discuss below, the NDR position can be explained quantitatively by considering the electrostatic potential across the double bilayer heterostructures.

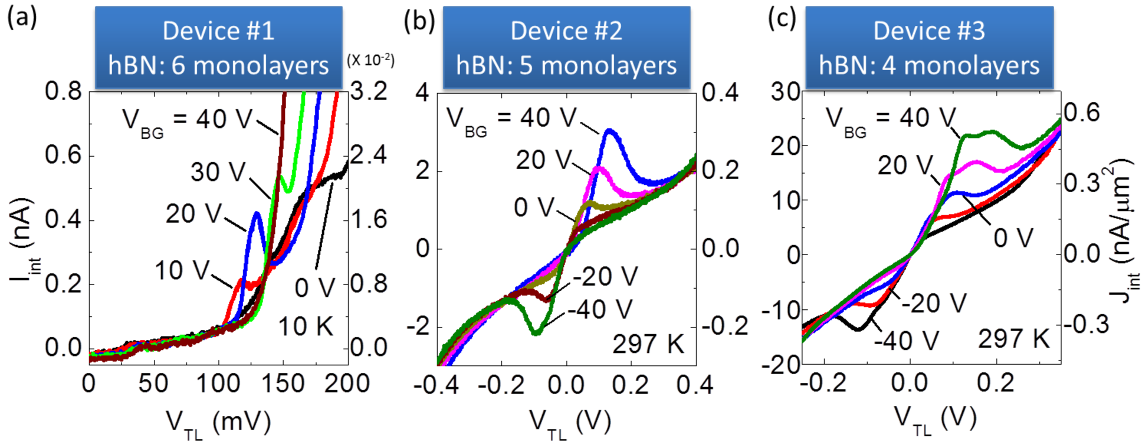

Figure 3.9: Interlayer current-voltage characteristics and resonant tunneling. I_{int} vs. V_{TL} of (a) Device #1 measured at T = 10 K, and (b) Device #2 measured at room temperature. (c) Device #3 measured at room temperature. The right axes show the interlayer current normalized by the active area.

3.3.4 Thickness dependence of interlayer resistance and capacitance

Figure 3.10(a) shows the normalized interlayer resistance (R_c) in double bilayer graphene devices as a function of interlayer hBN thickness, from 4 to 8 monolayers, measured at zero interlayer bias, and at either low T = 1.4 - 20 K temperatures, or at room temperature. Data are included from both devices with and without resonant tunneling. The data show an exponential dependence on thickness of the tunneling barrier, similar to experimental tunneling data through hBN using graphite and gold electrodes [86]. These data indicate that the R_c value is largely determined by the interlayer hBN thickness.

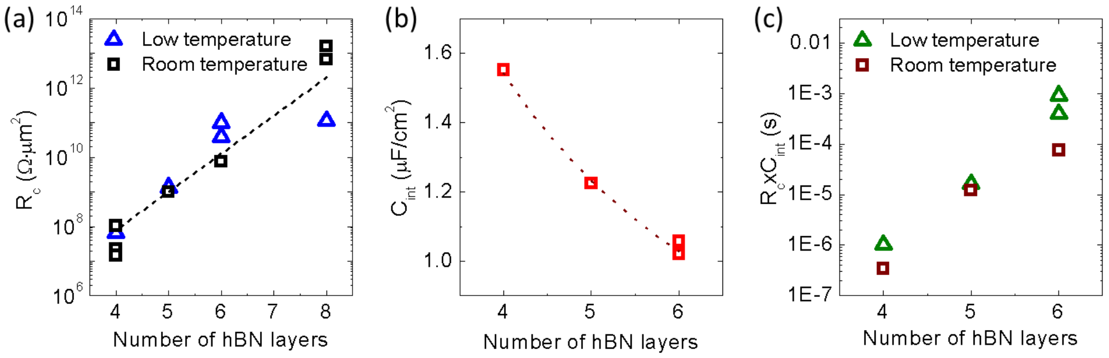

Figure 3.10: (a) Normalized interlayer resistance vs. number of hBN layers measured in multiple devices and at a low temperature of T = 1.4 – 20 K and at room temperature. (b) C_{int} vs. number of hBN layers. (c) $R_c \times C_{int}$ (delay time) vs. number of hBN layers. The dashed lines in panels (a) and (b) are guides to the eye.

Figure 3.10(b) shows the C_{int} vs. number of hBN. The C_{int} data show the expected 1/thickness dependence. The number of hBN layers can be converted to hBN

thickness (t_{hBN}) using the interlayer spacing of 2.67 Å. We use Fig. 3.10(b) data to calculate the dielectric constant of hBN, by first plotting C_{int}^{-1} vs. t_{hBN}, calculating the slope of C_{int}^{-1} vs. t_{hBN} and finally using the slope value in $k = (dC_{int}^{-1}/dt_{hBN})^{-1} \cdot (1/\epsilon_0)$. The experimentally measured dielectric constant of the hBN is $k = 1.8$.

An important figure of merit often used for benchmarking of CMOS devices is the delay time. For interlayer tunneling field-effect transistors (ITFET), the relevant delay time is defined by product of normalized interlayer resistance and interlayer capacitance. Figure 3.10(c) shows $R_c \times C_{int}$ (in units of second) vs. number of hBN layers. The fastest device, with 4 layers-thick interlayer hBN, possesses a delay time of about 1 μs indicating the maximum achievable operation frequency for this device is relatively low. To reduce the delay time, smaller R_c and C_{int} values are desired. Lower R_c values can be achieved by reducing t_{hBN}, however, the two bilayer graphene are likely to be shorted when the thickness of the interlayer dielectric is three atoms or less. A more feasible solution to achieve lower interlayer resistance is to replace hBN by a dielectric with a smaller band gap. The interlayer tunneling current $I_{int} \propto \exp(-\sqrt{\Delta})$ where Δ is the band gap of the dielectric, therefore, a dielectric with a band gap smaller than that of hBN yields a smaller R_c and hence a smaller delay time. On the other hand, reducing C_{int} can be achieved by using a thicker dielectric, not desired because of increasing R_c, or by using a dielectric with smaller dielectric constant.

3.3.5 Energy band alignment at resonant tunneling

To better understand the origin of the observed NDR in Figs. 3.9, it is instructive to examine the energy band alignment in the double bilayer graphene heterostructure. To determine if the NDR occurrence stems from momentum conserving tunneling, we examine the biasing conditions at which the charge neutrality points of the two bilayer graphene are aligned and the electrostatic potential drop across the interlayer dielectric is zero:

$$eV_{TL} + \mu_T(n_T) - \mu_B(n_B) = 0 \qquad (3.16)$$

Figure 3.11 illustrates the energy band alignment of a double bilayer graphene device at biasing conditions where the charge neutrality points of top and bottom bilayers are aligned, the condition most favorable for momentum conserving tunneling. The schematic ignores the band-gap induced in the two layers as a result of finite transverse electric fields, as the layer chemical potentials are controlled mainly by the carrier densities (Fig. 3.8).

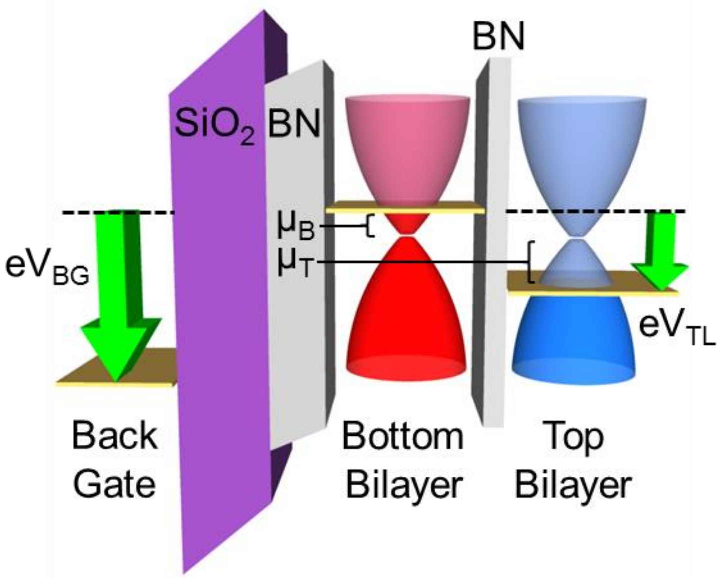

Figure 3.11: Energy band diagram of the double bilayer graphene device when charge neutrality points of top and bottom bilayers are aligned.

The symbols in Fig. 3.12 show the experimental values of the tunneling resonance as a function of V_{TL} and V_{BG} for Devices #1 and #2, defined as the maximum conductivity point in Figs. 3.9(a,b) data. The solid lines show the calculated V_{TL} vs. V_{BG} values corresponding to layer densities and chemical potential that satisfy eq. 3.16, corresponding to the charge neutrality points of the two layers being aligned. The good agreement between the experimental values and calculations in Fig. 3.12 strongly suggests that the tunneling resonance occurs when the charge neutrality points of the two bilayer graphene are aligned, which in turn maximizes momentum (**k**) conserving tunneling between the two layers [87]–[89]. This observation is also in agreement with

the findings in other 2D-2D systems where resonant tunneling occurs when the energy bands of the two quantum wells are aligned [61]–[64].

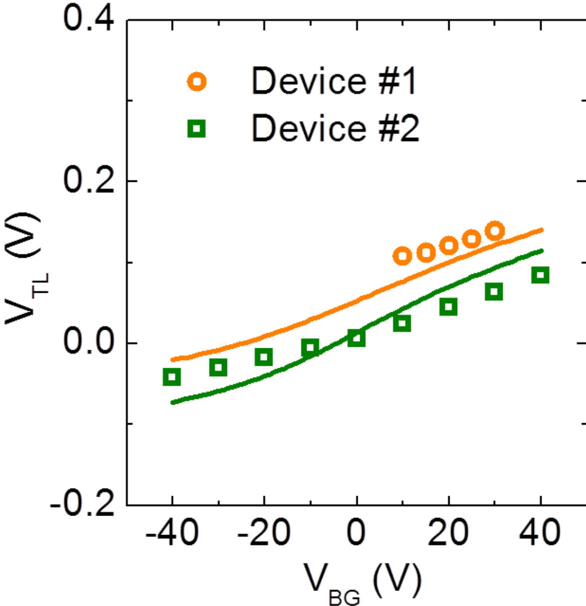

Figure 3.12: V_{TL} vs. V_{BG} of Devices #1 and #2 at tunneling resonance (circles) and when charge neutrality points are aligned (solid line)

3.3.6 Carrier densities at resonant tunneling

Figure 3.13 shows the layer densities n_T vs. n_B calculated in Devices #1 and #2 at the tunneling resonance position corresponding to Figs. 3.9(a,b) data. In Device #1 the top (bottom) bilayer is populated with holes (electrons) at the tunneling resonance. In Device #2 the top bilayer is close to neutrality, while the bottom bilayer carrier type can be either hole or electron depending on the applied V_{BG}. Most notably, in both devices the tunneling resonance occurs at a fixed top layer density value. This observation can be

understood using eq. 3.13 and eq. 3.16, which yield a fixed top layer density $n_T = e/(V_{TL-DNP} \cdot C_{int})$ when the charge neutrality points are aligned, independent of V_{BG}.

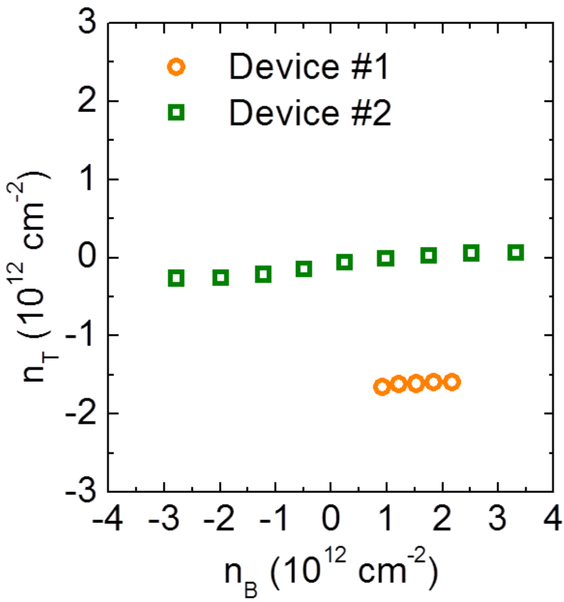

Figure 3.13: n_T vs. n_B of Devices #1 and #2 at tunneling resonance.

3.3.7 Resonant tunneling at large interlayer bias

We have so far presented I_{int} vs. V_{TL} of three double bilayer graphene devices possessing gate-tunable resonant tunneling in the vicinity of V_{TL} = 0 V. In this section, we focus on the interlayer current-voltage characteristics of double bilayer devices at large V_{TL} values beyond the range presented in Fig 3.9. Figure 3.14(a) shows I_{int} vs. V_{TL} of Device #2 measured in the range -0.9 V ≤ V_{TL} ≤ 0.9 V at room temperature and at V_{BG} = -40, 0, 40 V. Figure 3.14(a) data reveals three sets of gate-tunable resonant tunneling, one set centered around V_{TL} = 0 V and two sets at $|V_{TL}| \cong$ 0.5 - 0.7 V. The first set of gate-tunable resonant tunneling, is extensively discussed in the previous sections where it is

associated to the energy and momentum conserving tunneling when the charge neutrality points of the two bilayer graphene are energetically aligned. The additional two sets of resonant tunneling, at larger V_{TL}, are equally interesting, however, the origin of them needs to be clarified.

To better understand the origin of the resonant tunneling at $|V_{TL}| \cong$ 0.5 - 0.7 V, Fig. 3.14(b) shows the differential conductance (dI_{int}/dV_{TL}) vs. electrostatic potential drop (V_{ES}) defined as $V_{ES} = V_{TL} + [\mu_T(n_T) - \mu_B(n_B)]/e$ for Device #2. The maximum differential conductance in Fig. 3.14(b) occur either at V_{ES} = 0 V or V_{ES} = ± 0.4 V independent of the applied V_{BG}. The 0.4 V spacing between the differential conductance peaks is similar to the reported energy difference between the first and second sub-bands of bilayer graphene at **K**-point [90] which suggests the resonant tunneling at $|V_{TL}| \cong$ 0.5 - 0.7 V occurs when the lower conduction band of one layer is aligned with the upper conduction band of the opposite layer. Figures 3.14(c-e) illustrate the energy band alignment in double bilayer graphene heterostructure at V_{ES} = - 0.4 V, V_{ES} = 0 V, V_{ES} = 0.4 V, respectively.

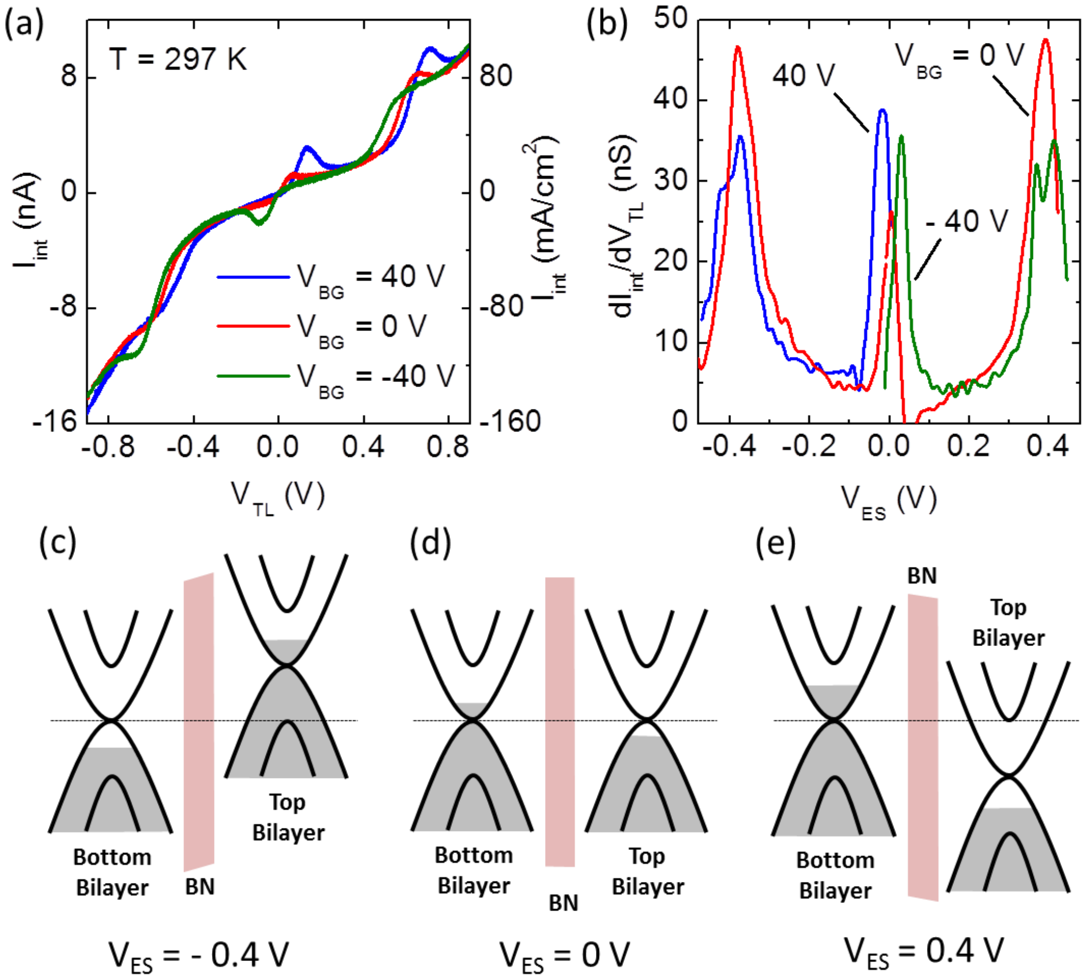

Figure 3.14: (a) I_{int} vs. V_{TL} of Devices #2 measured at room temperature, and at V_{BG} = -40, 0, 40 V. In addition to the resonant tunneling centered around V_{TL} = 0 V, there are two additional sets of resonant tunneling occurr at $|V_{TL}|$ = 0.5 - 0.6 V. (b) dI_{int}/dV_{TL} vs. V_{ES} corresponding to the data of panel (a) measured at room temperature, and at V_{BG} = -40, 0, 40 V. (c-e) The schematic presentation of the energy band alignment in double bilayer graphene at (a) V_{ES} = - 0.4 V (b) V_{ES} = 0 V (c) V_{ES} = 0.4 V. In panels (c) and (e) the lower conduction band of one bilayer is aligned with the upper conduction band of the opposite bilayer. In panel (b), the charge neutrality points of the two bilayers are aligned (Figure and caption adopted from ref. [91]).

3.3.8 Temperature dependence

Figures 3.15(a-c) show the temperature dependence of I_{int} vs. V_{TL} measured in Device #2 and at V_{BG} = -40, 0, 40 V, respectively. At lower temperatures and at the resonant tunneling, the slope of I_{int} vs. V_{TL}, i.e. differential conductance, increases. In addition to the resonant tunneling, Figs. 3.15(a-c) data exhibit a non-resonant tunneling current background that increases with V_{TL} and it is associated with non-momentum-conserving tunneling. Fig. 3.15 data shows the non-resonant tunneling component has a weak temperature dependence.

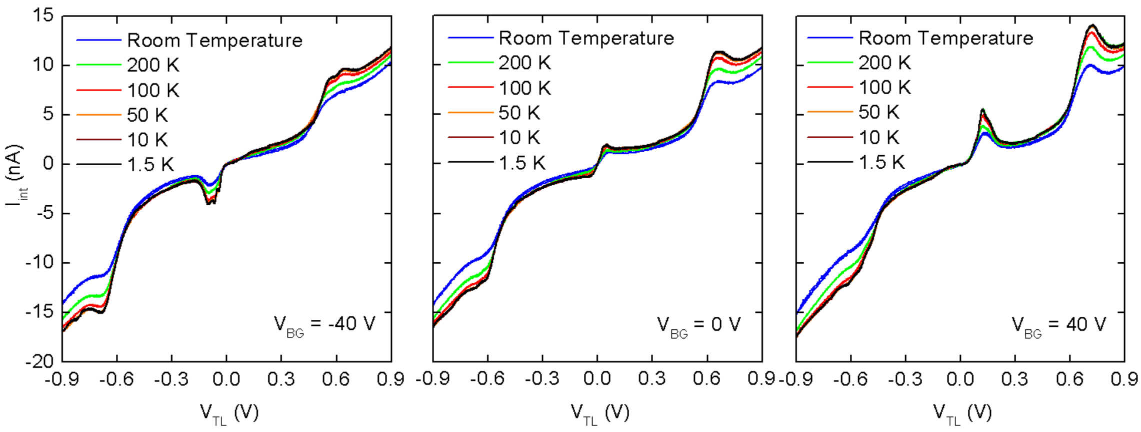

Figure 3.15: I_{int} vs. V_{TL} of device #2 measured at V_{BG} = -40, 0, 40 V and at temperatures ranging between T = 1.5 K and room temperature. The temperature dependence of the background tunneling current is relatively weak.

A recent theoretical study [92] suggests the background tunneling current in graphene/hBN/graphene heterostructures is due to the inelastic electron-phonon

scattering. In fact, the best fit to the experimentally measured background tunneling current is achieved by taking into account the emission of optical flexural (ZO) phonons in hBN.

3.3.9 Transverse electric field across the individual bilayers

The momentum-conserving tunneling between two bilayer graphene depends on their energy-momentum dispersion, and density of states. The band structure of bilayer graphene, particularly close to the CNP, can be tuned by an applied transverse electric (E) field, as a result of the applied V_{BG} and V_{TL}. In the previous section, we showed resonant tunneling peaks occur when the charge neutrality points of the two bilayers are energetically aligned. A recent theoretical study suggests an additional set of resonant tunneling peaks in a double bilayer graphene heterostructure originating from the alignment of the density of state features close to the band edge when the two bilayers possess a band gap [93]. The additional set of resonant peaks, characterized by sharp peaks, is expected primarily at low temperatures. At high temperatures the sharp peaks become weaker when due to the more significant contribution of the thermally occupied adjacent states. It is therefore instructive to examine the E-field value for the two bilayers in a double bilayer graphene heterostructure. The general expressions for transverse E-field across the top (E_T) and bottom (E_B) bilayers in a double bilayer graphene device are:

$$E_B = \frac{en_B}{2\varepsilon_0} + \frac{en_T}{\varepsilon_0} + E_{B0} \quad (3.17)$$

$$E_T = \frac{e n_T}{2\varepsilon_0} + E_{T0} \qquad (3.18)$$

here n_T and n_B are the top and bottom layer densities, respectively, and ε_0 is the vacuum permittivity. E_{T0} and E_{B0} are the transverse E-fields across the top and bottom bilayer at the DNP, as a result of unintentional layer doping. At a given V_{BG} and V_{TL}, the n_B and n_T values can be calculated from eqs. 3.11 and 3.12. The E_{B0} value can be calculated as following. We first determine $E_B = 0$ point, marked by minimum ρ_B along the CNL of the bottom bilayer resistivity contour plot [Fig. 3.16(a)]. At $E_B = 0$, eq. 3.11 and 3.17 yield:

$$E_{B0} = \frac{C_{BG} \Delta V_{BG}}{\varepsilon_0} \qquad (3.19)$$

Here $\Delta V_{BG} = V_{BG-DNP} - V_{BG-E_B=0}$.

Finding the value of the E_{T0} in a back-gated double bilayer device requires an assumption about the dopant position that cause the device DNP to shift from $V_{BG} = V_{TL} = 0$ V. To calculate the E_{T0} in our devices assume the dopants are placed on the top bilayer graphene, an assumption most plausible when the top bilayer is uncapped, as in Device #1. Equation 3.17 combined with the Gauss law yield:

$$E_{T0} = \frac{C_{BG} V_{BG-DNP}}{\varepsilon_0} \qquad (3.20)$$

Figures 3.16(b,c) show the calculated E_T and E_B in Device #1 and #2 along the locus of aligned neutrality points in the two bilayers, i.e. at the tunneling resonance, as a function of V_{BG}. At the tunneling resonance E_B shows a linear dependence on V_{BG}, while E_T remains constant. For Device #1, the condition $E_T = E_B$, desirable for identical energy-

momentum dispersion in the two bilayers occurs at $V_{BG} = 24\ V$, and a finite E-field. For Device #2, $E_T = E_B$ is closer to zero, and at $V_{BG} = -7\ V$. Figures 3.9(a) and 3.16(b) data combined suggest the tunneling resonance in Device #1 is strongest in the vicinity of the $E_T = E_B$ point, where the band structures are closely similar for both top and bottom bilayers. The tunneling resonance in Device #2 occurs over a wider range of V_{BG} where the difference between the E_T and E_B can be as large as 0.34 V/nm.

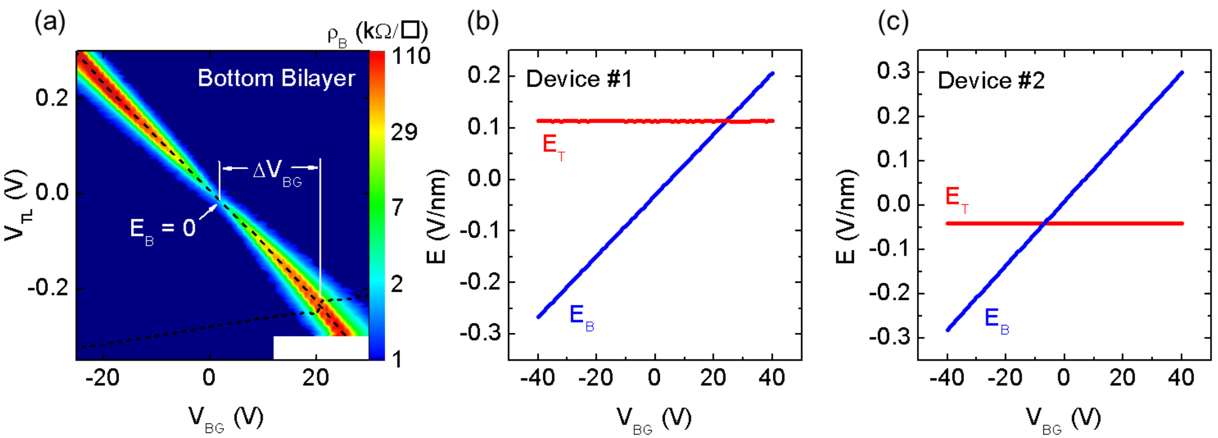

Figure 3.16: (a) Device #1 ρ_B contour plot vs. V_{BG} and V_{TL}, measured at T = 1.4 K. The CNL of the top bilayer graphene is added to mark the DNP. E_T and E_B in (b) Device #1, and (c) Device #2, calculated at the tunneling resonance.

3.4 BROADENING OF THE RESONANT TUNNELING PEAKS

In addition to the location of the resonances, we also considered their broadening. Potential sources of broadening include finite initial and final state lifetimes τ due to scattering, rotational misalignment θ, or the non-uniformity of tunneling associated with

spatial inhomogeneities. While a detailed theoretical description of the tunneling in double bilayers is outside the scope of this study, in the following we provide estimates for the broadening associated with these mechanisms gauges in terms of the alignment of the band structures, i.e., the electrostatic potential difference between bilayers $V_{ES} = V_{TL} + [\mu_T(n_T) - \mu_B(n_B)]/e$.

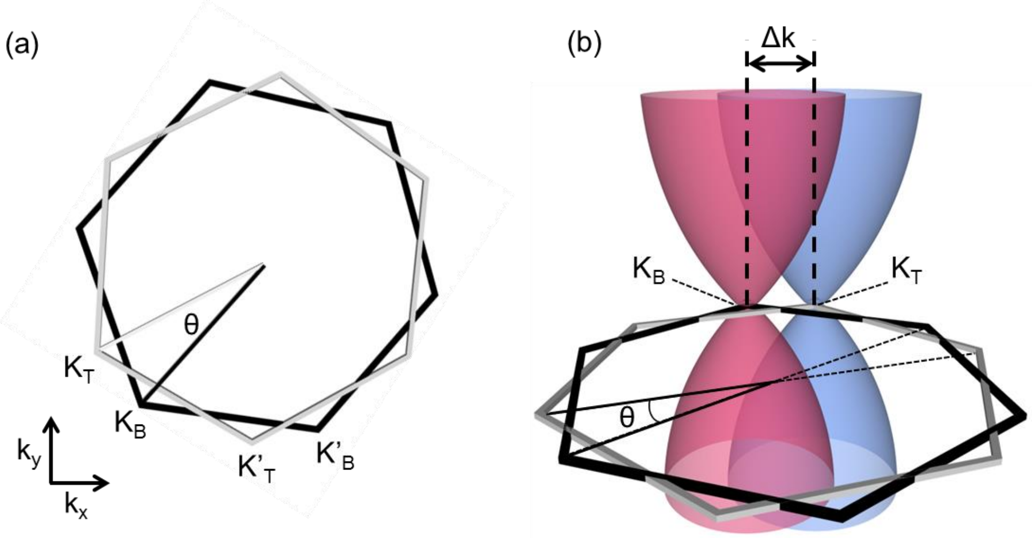

Figure 3.17: Energy band diagram of rotationally misaligned bilayers. (a) Brillouin zone boundaries of two hexagonal lattices rotationally misaligned by θ° in real space. K_B (K_T) is the valley minimum the bottom (top) bilayer graphene. (b) A rotational misalignment by a small angle θ translates into valley separation in momentum space by $\Delta k \cong |K|\theta$.

The contribution from the carrier scattering lifetime (τ) in either layer to the broadening width in units of volts is $\Delta V_{\tau} \cong \hbar/(e\tau)$, where $\hbar$ is the reduced Planck constant. Using the momentum relaxation time τ_m obtained from the carrier mobility $\mu = e\tau_m/m^*$, where m^* is the effective mass, a lower limit of the broadening can be

estimated to be $\Delta V_\tau \cong \hbar/(\mu m^*)$. The broadening width associated with rotational misalignment can be estimated using the wave-vector difference $\Delta k = |\mathbf{K}|\theta$ illustrated in Fig. 3.17(b), which translates into a broadening $\Delta V_\theta \approx \hbar\bar{v}|\mathbf{K}|\theta/e$, where $\bar{v}$ is an average velocity of the tunneling carriers, and $|\mathbf{K}| = 1.7 \times 10^{-10}$ m^{-1} is the wave-vector magnitude at the valley minima. Using the Fermi velocity of monolayer graphene v_F = 1.1×10^8 cm/s as reference leads to a numerical expression $\Delta V_\theta \approx (180\ \mathrm{m}V)(\bar{v}/v_F)(\theta/1^\circ)$. The lower carrier velocity in bilayer by comparison to monolayer graphene leads to a reduced resonance broadening at a given rotational misalignment angle θ. However, a notable difference between tunneling in bilayer vs. monolayer graphene is that rotational misalignment can be compensated in double monolayer by applying a larger interlayer bias to bring into coincidence states with equal momenta and energies in the two layers [74], [87].

The effective mass of bilayer graphene is both density and transverse electric field dependent [8], [82]. Using an average effective mass value m^* = 0.05 m_e [82], where m_e is the bare electron mass, the lower layer mobility value in Device #1 of 3,500 $cm^2/V\cdot s$ corresponds to a broadening ΔV_τ = 6 mV. For Device #2 the corresponding broadening is ΔV_τ = 11 mV, using the top and bottom layer mobility values of 14,800 and 2,400 $cm^2/V\cdot s$ measured at room temperature. The experimental values for the tunneling resonance width are $\Gamma \cong 12$ mV and $\Gamma \cong 68$ mV for Devices #1 and #2, measured at T = 10 K, and room temperature respectively. These values are determined by fitting

Lorentzian peaks to the I_{int}/V_{TL} data of Figs. 3.9(a,b) data plotted as a function of V_{ES}; an example is shown in Fig. 3.18(a).

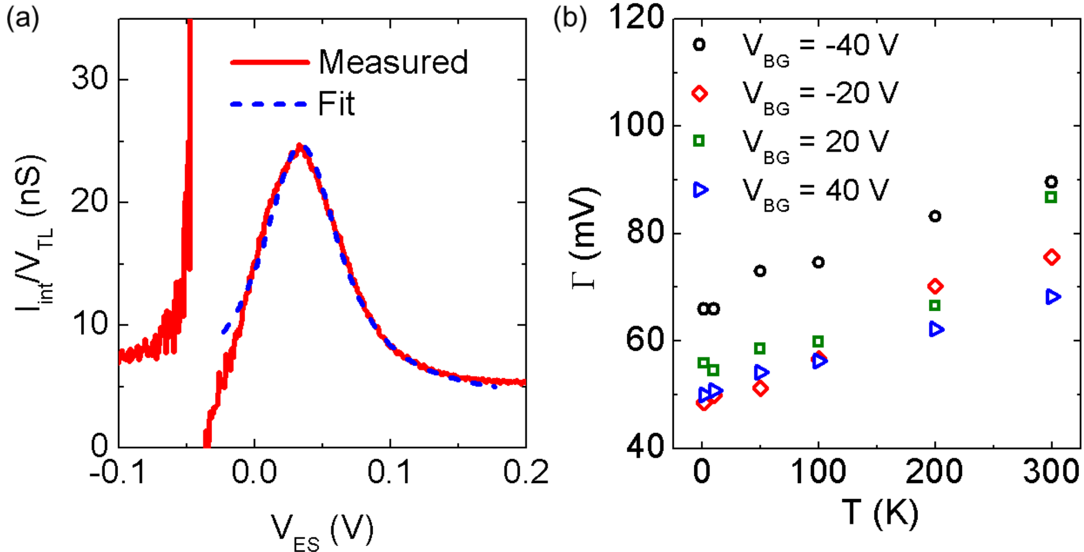

Figure 3.18: (a) I_{int}/V_{TL} vs. V_{ES} for Device #2 at V_{BG} = 40 V and at T = 297 K (solid line), along with a Lorentzian fit to the experimental data (dashed line). (b) Temperature dependence of Γ measured in Device #2 and at V_{BG} = -40, -20, 20, 40 V. (Right panel adapted from Ref. [91])

3.4.1 Temperature dependence

Figure 3.18(b) shows the temperature dependence of Γ measured in Device #2 and at V_{BG} = -40, -20, 20, 40 V. The data of Fig. 3.17(b) shows Γ has a weak dependence on temperature in the range 1.5 K ≤ T ≤ 300 K suggesting acoustic phonon scattering is not the primary source of broadening. As the ΔV_{τ} values calculated above are lower than the experimental values ΔV_{ES}, we conclude that the broadening is mainly limited by

rotational alignment in our devices, with Device #1 having a better alignment than Device #2. Although we cannot quantify experimentally the rotational misalignment in the two devices, we note that during fabrication Device #1 was annealed after each graphene and hBN layer transfer, while Device #2 was annealed after the double bilayer stack was completed. We speculate that multiple annealing steps may improve the rotational alignment between the layers.

3.4.2 Interlayer tunneling with an in-plane magnetic field

In rotationally misaligned bilayer graphene when the rotational angle θ is small, the separation of the charge neutrality points in the k-space can be written as $\Delta\boldsymbol{K}_i = \boldsymbol{l}_z \times \theta\boldsymbol{K}_i$ where i = 1 to 6 corresponds to the 6 valleys and $\boldsymbol{l}_z$ = (0,0,1). Tunneling carriers in a double bilayer graphene heterostructure gain an in-plane momentum $et_{hBN}\boldsymbol{l}_z \times \boldsymbol{B}_{||}$ when an external in-plane magnetic field ($\boldsymbol{B}_{||}$) is applied. Thus, for a rotationally misaligned bilayer graphene in an external in-plane magnetic field, the momentum transfer is written as $\hbar\Delta\boldsymbol{K}_i = \boldsymbol{l}_z \times [\theta\boldsymbol{K}_i + et_{hBN}\boldsymbol{B}_{||}]$. Depending on the relative alignment of the in-plane magnetic field and the bilayer crystal orientations the momentum transfer at each valley could be different [74].

The resonant tunneling in double bilayer graphene heterostructures occurs when the energy and momentum of the carriers are conserved while tunneling. Applying an external in-plane magnetic field, not can changes the in plane momentum of the tunneling carriers but also shifts the Brillion zones of the layers with respect to each other.

Consequently, an in-plane magnetic field is expected to change the resonant tunneling characteristics. Figure 3.19 shows I_{int} vs. V_{TL} of Device #2 measured in $B_{||}$ = 0, 14 T and at V_{BG} = -40 [panel (a)] and V_{BG} = 40 V [panel (b)].

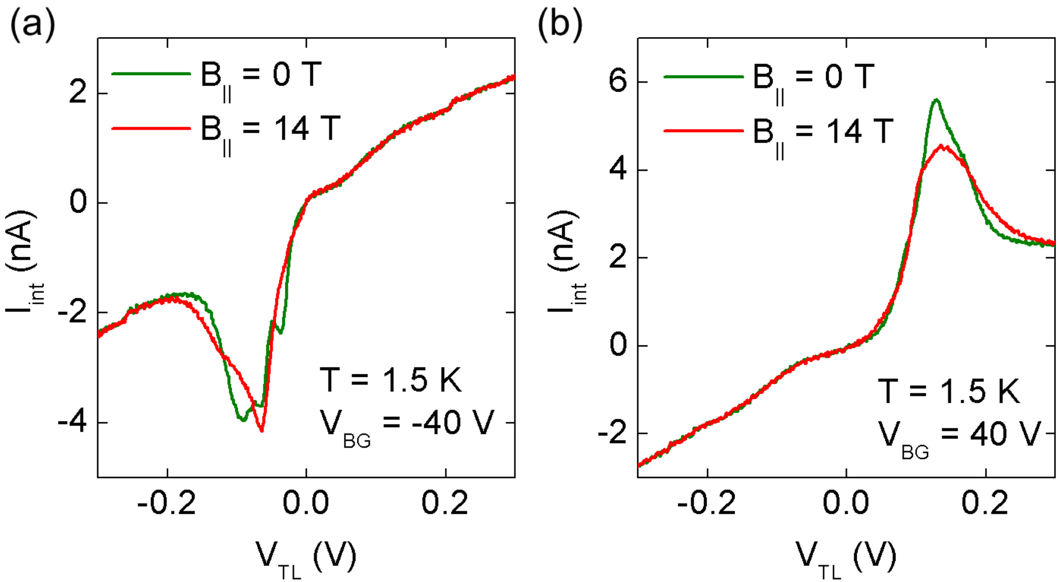

Figure 3.19: I_{int} vs. V_{TL} of Device #2 measured at in-plane magnetic fields $B_{||}$ = 0, 14 T and at (a) V_{BG} = -40 V and (b) V_{BG} = -40 V.

There are a few noteworthy features in Fig. 3.19. In both panels, the in-plane magnetic field changes I_{int} vs. V_{TL} only in the vicinity of the resonant tunneling bias confirming the resonant tunneling is a momentum conserving process. In addition, in Fig 3.19(a), the small features superimposed on the local I_{int} minima (centered at $V_{TL} \cong$ - 0.1 V) in $B_{||}$ = 0 T trace disappear at $B_{||}$ = 14 T. These small features in zero magnetic field I_{int} vs. V_{TL} are associated with the alignment of the bilayer graphene band edge features when bilayer graphene possesses a band gap [93]. Another noteworthy effect of the in-

plane magnetic field is on the broadening of the resonant peaks. As an example, at V_{BG} = 40 V, the broadening of the resonant peaks at $B_{||}$ = 0 T is Γ = 50 mV, while in the presence of an in-plane magnetic field $B_{||}$ = 14 T, the width of the broadening increases to Γ = 98 mV.

3.5 SUMMARY

In summary, we present a study of interlayer electron transport in double bilayer graphene. In devices where the bilayers straight edges were rotationally aligned during the fabrication we observe marked resonances in interlayer tunneling. Using individual layer densities and experimental values of the layer chemical potential we show that the resonances occur when the charge neutrality points of the two layers are energetically aligned, consistent with momentum-conserving tunneling. The interlayer conductivity values show an exponential dependence of the interlayer hBN thickness, and can serve to benchmark switching speed for potential device applications.

CHAPTER 4: QUANTUM HALL EFFECT IN BERNAL STACKED AND ROTATIONALLY MISALIGNED CVD BILAYER GRAPHENE

In this chapter, we examine the quantum Hall effect in bilayer graphene grown on Cu substrates by chemical vapor deposition. Spatially resolved Raman spectroscopy suggests a mixture of A-B (Bernal) stacked and rotationally misaligned (twisted) domains. Magnetotransport measurements performed on bilayer domains with a wide 2D band reveal quantum Hall states (QHSs) at filling factors ν = 4, 8, 12, consistent with an A-B stacked bilayer, while magnetotransport measurements in bilayer domains defined by a narrow 2D band show a superposition of QHSs of two independent monolayers. The analysis of the Shubnikov–de Haas oscillations measured in rotationally misaligned graphene bilayers provides the carrier density in each layer as a function of the gate bias and the interlayer capacitance.

4.1 INTRODUCTION

A-B stacked bilayer graphene, as discussed in the first chapter, possesses parabolic energy-momentum dispersion close to the charge neutrality point as well as a tunable bandgap in the presence of a transverse electric field (E-field). When the stacking order of two layers is not A-B, i.e. two layers are rotationally misaligned, the electronic properties of bilayer graphene deviates from that of A-B stacked bilayer graphene. Theoretical calculations show the electronic properties of commensurate, rotationally misaligned bilayer depend on the degree of rotational misalignment angle θ [5]–[7], [94],

[95]. The fundamental differences between A-B stacked and rotationally misaligned bilayer graphene can be summarized as (i) the energy-momentum dispersion of rotationally misaligned bilayer graphene is linear similar to that of monolayer graphene yet with a smaller Fermi velocity that depends on the rotational misalignment angle θ [5], [6]; (ii) applying a transverse E-field across rotationally misaligned bilayer does not lead to a band gap opening [5]; (iii) the emergence of two low-energy van Hove peaks in DOS of the rotationally misaligned bilayer originating from the mixing of the linear energy bands of the two monolayers [96].

Monolayer graphene, as described in the first chapter, is a Bravais lattice with two sub-lattices A and B and primitive lattice vectors:

$$\boldsymbol{a}_1 = a\left(\frac{1}{2},\frac{\sqrt{3}}{2}\right), \boldsymbol{a}_2 = a\left(-\frac{1}{2},\frac{\sqrt{3}}{2}\right)$$

where $a = 2.46$ Å is the lattice constant. In the A-B stacked bilayer graphene, sub-lattice A of one layer (namely A_1) is aligned with the sub-lattice B of the opposite layer (namely B_2). In rotationally misaligned bilayer graphene, one layer is rotated with respect to the other layer with a rotational angle θ. Here, for simplicity, we assume the origin of the rotation is an A_1-B_2 site. The rotationally misaligned bilayer is commensurate if an A_1-B_2 site, besides the one at the origin, occurs elsewhere. Fig. 4.1 shows the lattice of a commensurate, rotationally misaligned bilayer graphene with $\theta = 3.89°$. The superimposed honeycomb lattices of the two monolayers in a commensurate, rotationally misaligned bilayer, form a supper-lattice with a periodicity that depends on θ.

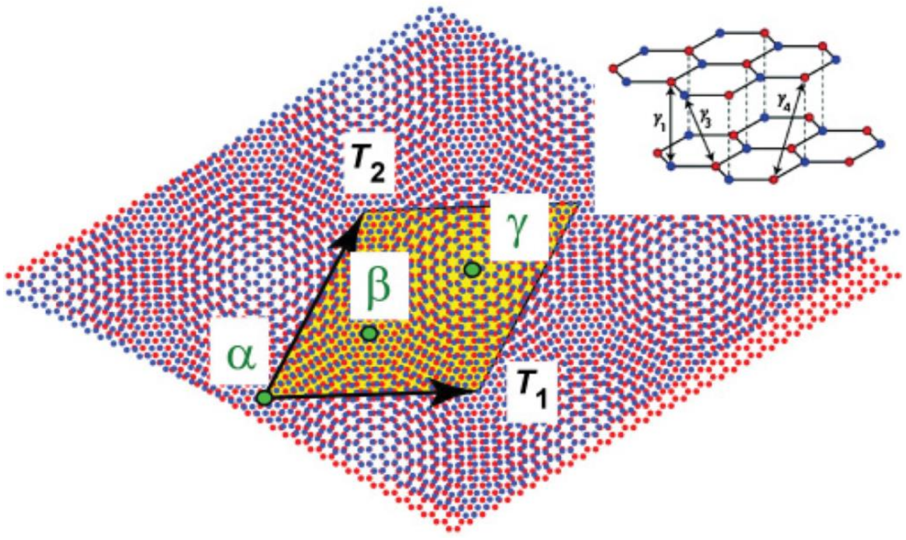

Figure 4.1: Lattice structure of rotationally misaligned bilayer graphene at θ = 3.89°, with super-lattice primitive vectors $\boldsymbol{T}_1$ and $\boldsymbol{T}_2$. The points α, β, and γ correspond to A-B, B-A, and A-A stacked sites respectively. The unit cell of the super-lattice is marked with the yellow rhombus. The inset illustrates three hopping processes in the interlayer Hamiltonian (Figure and caption adapted from Ref. [94]).

A commensurate bilayer graphene is obtained when a B_2 site is rotated to a spot formerly occupied by a similar sub-lattice atom. Using this condition, an expression is derived for the rotational angles leading to a commensurate structure [5]:

$$\theta_i = cos^{-1}\left(\frac{3i^2 + 3i + 1/2}{3i^2 + 3i + 1}\right) \qquad i = 1,2,\ldots \qquad (4.1)$$

The primitive lattice vectors associated with the supper-lattice of commensurate, rotationally misaligned bilayer graphene are [5]:

$$\boldsymbol{T}_1 = i\boldsymbol{a}_1 + (i+1)\boldsymbol{a}_2, \quad \boldsymbol{T}_2 = -(i+1)\boldsymbol{a}_1 + (2i+1)\boldsymbol{a}_2 \qquad (4.2)$$

The lattice constant Figure 4.1 shows the primitive lattice vectors $\boldsymbol{T}_1$ and $\boldsymbol{T}_2$, and sites with the highest symmetry in the unit cell: α (A-B stacked), β (B-A stacked), and γ (A-A stacked). The lattice constant of the supper-lattice is:

$$|\boldsymbol{T}_1| = \sqrt{3i^2 + 3i + 1}a_0 \qquad (4.3)$$

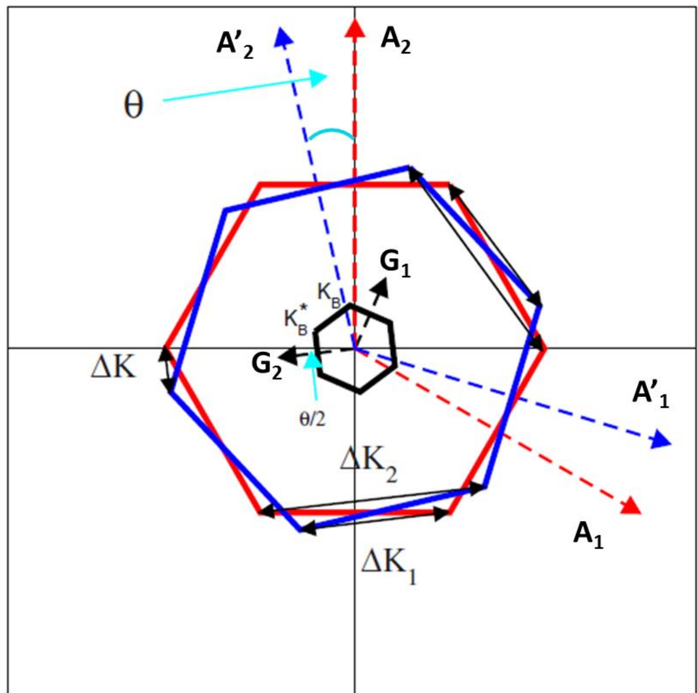

Figure 4.2: Brillouin zones of the fixed and rotated monolayer graphene, as well as the Brillouin zone of the commensurate, rotationally misaligned bilayer graphene for θ = 13.17°. In this Figure $\boldsymbol{A}_1$ and $\boldsymbol{A}_2$are the reciprocal lattice vectors of the fixed layer, $\boldsymbol{A}_1'$ and $\boldsymbol{A}_2'$ the reciprocal lattice vectors of the rotated layer, and $\boldsymbol{G}_1$, $\boldsymbol{G}_1$ the reciprocal lattice vectors of the super-lattice (Figure and caption adapted from ref. [94]).

Finally, the reciprocal lattice vectors associated with the supper-lattice of commensurate, rotationally misaligned bilayer graphene are:

$$\boldsymbol{G}_1 = \frac{4\pi}{3(3i^2 + 3i + 1)} [(3i + 1)\boldsymbol{a}_1 + \boldsymbol{a}_2] \quad (4.4)$$

$$\boldsymbol{G}_2 = \frac{4\pi}{3(3i^2 + 3i + 1)} [-(3i + 2)\boldsymbol{a}_1 + (3i + 1)\boldsymbol{a}_2] \quad (4.5)$$

Figure 4.2 shows the reciprocal lattice vectors of the individual layers (**A**$_1$, **A**$_2$, **A'**$_1$ **A'**$_2$) and the supper-lattice (**G**$_1$, **G**$_2$).

Figure 4.3(a) shows the first Brillion zone of commensurate, rotationally misaligned bilayer graphene, centered at midpoint between the charge neutrality points of the two layers. G_1 and G_2 represent reciprocal lattice vectors of the super-lattice and $\otimes$ marks the charge neutrality points of the two layers at $\pm\Delta K/2$ on the y-axis.

Figure 4.1(b) shows an example of the energy-momentum dispersion of commensurate rotationally misaligned bilayer graphene with a rotational misalignment angle $\theta = 3.9°$ along the line passing through the charge neutrality points of the two monolayers [Fig. 4.1(a)] calculated in a continuum approximation [5]. Here, the energy-momentum dispersion close to the charge neutrality points of the two layers ($k/\Delta K = \pm 0.5$) is linear and there is no energy gap at the charge neutrality points. The Fermi velocity of the rotationally misaligned bilayer graphene ($\tilde{v}_F$) is [5], [6]:

$$\frac{\tilde{v}_F}{v_F} = 1 - 9\left[\frac{\tilde{t}_\perp}{\hbar v_F \Delta K}\right]^2$$

where v_F is the Fermi velocity in monolayer graphene, $\hbar$ is the reduced Planck constant, ΔK is the amplitude of the wavevector at the corner of the Brillion zone [marked in Fig 4.1(a)], and $\tilde{t}_\perp$ is the coupling energy between zero energy doublet of one layer and six states from opposite layer with energies $\pm v_F \Delta K$. Figure 4.1(c) presents the normalized

Fermi velocity of rotationally misaligned bilayer ($\tilde{v}_F/v_F$) as a function of the misalignment angle calculated by perturbation theory and the continuum model. At large rotational angles, $\tilde{v}_F$ is nearly constant with a value close to v_F while at small rotational angles, $\tilde{v}_F$ is smaller than v_F and shows strong θ dependence.

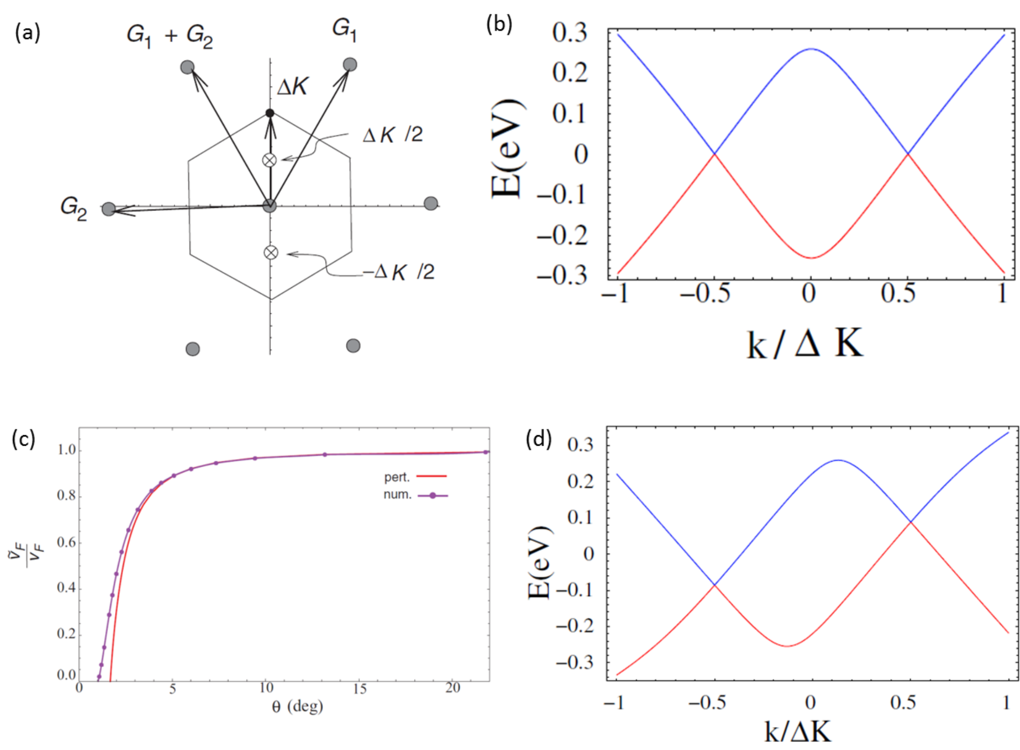

Figure 4.3: (a) The first Brillion zone of rotationally misaligned bilayer centered midpoint between the charge neutrality points of the two monolayers (marked with ⊗). G_1 and G_2 are the reciprocal lattice vectors of the super-lattice. (b) Energy-momentum dispersion of rotationally misaligned bilayer graphene with rotational misalignment $\theta = 3.9°$ (c) Rotationally misaligned bilayer Fermi velocity normalized by monolayer Fermi velocity vs. θ calculated by continuum model. (d) Same as panel (b) but in the presence of a potential difference $V = 0.3$ V. The potential difference between two layers does not lead to band gap opening (Figures and caption adapted from Refs. [5], [6]).

Figure 4.1(d) shows the energy-momentum dispersion of the rotationally misaligned bilayer graphene of Fig. 4.1(b) with a potential difference V = 0.3 V between the two layers. Unlike A-B stacked bilayer graphene where a potential difference leads to opening of an energy gap at the charge neutrality point, the energy-momentum dispersion of the rotationally misaligned bilayer does not show bandgap at either charge neutrality points, a finding similar to that of monolayer graphene.

Raman spectroscopy, as discussed in the first chapter, is a powerful non-destructive characterization method widely used to determine the number of graphene layers. Bilayer graphene can be identified and differentiated from monolayer or thicker graphene based on the width and the shape of its 2D band. This method is relevant particularly when the stacking order of the layers is A-B. When the two layers are rotationally misaligned, the weak coupling between the layers leads to θ-dependent features in Raman spectrum [97], [98]. Figure 4.4(a) shows examples of rotationally misaligned bilayer graphene and monolayer graphene Raman spectra with rotational angles between 3° and 27° measured with a λ = 633 nm laser [97]. The Rama spectra of Fig. 4.2(a) reveals the position, width, and intensity of the 2D band (at $\cong 2700\ cm^{-1}$) as well as the intensity of the G band (at $\cong 1580\ cm^{-1}$) depend on the rotational misalignment angle θ. Figure 4.2(b) shows the energy dispersion relation of the rotationally misaligned bilayer graphene close to the charge neutrality points of the two layers (located at $\mathbf{K}_1$ and $\mathbf{K}_2$). The charge neutrality points are separated from each other in the momentum space as a result of the rotational misalignment. In addition, the overlap of the two energy bands, between charge neutrality points, induces Van Hove

singularities. Figure 4.4(c) shows the energy dependence of the rotationally misaligned bilayer graphene DOS (red trace) compared to that of monolayer graphene (blue trace). The interaction of the two layers in the rotationally misaligned bilayer graphene leads to the Von Hove singularity.

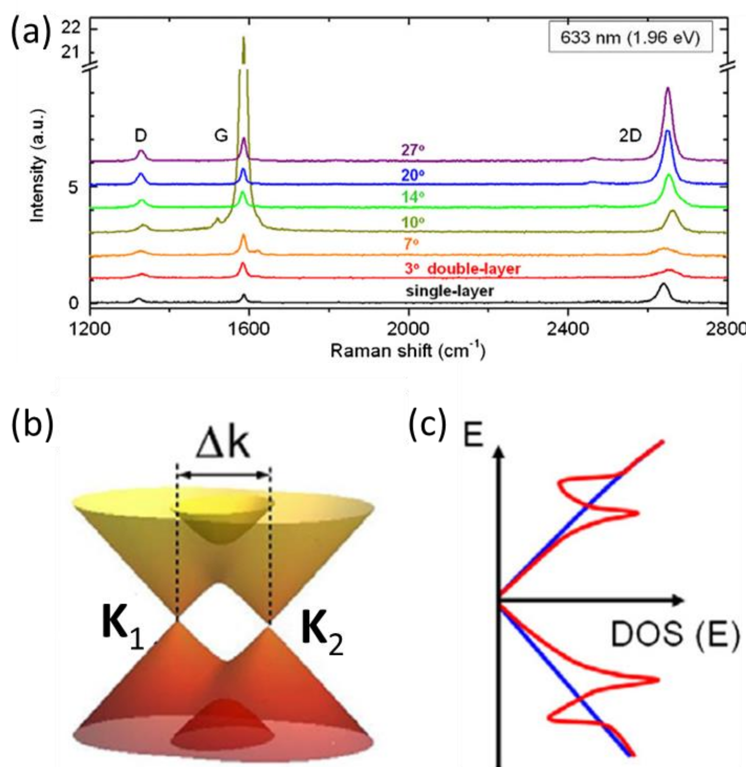

Figure 4.4: (a) Raman spectra of rotationally misaligned bilayer graphene and monolayer graphene measured with a λ = 633 nm laser. (b) Energy bands of rotationally misaligned bilayer graphene. Van Hove singularities are induced by overlap of individual layer energy bands. (c) The energy dependence of rotationally misaligned bilayer graphene density of states (DOS) without (blue) and with (red) interlayer interactions. DOS exhibit distortions from the interlayer interactions showing Van Hove singularities [97].

A notable feature in Fig. 4.2(a) is the intensity of the G band at $\theta = 10°$ which is significantly larger than others. At this rotational angle, the incident photon energy matches the energy difference between conduction and valance band Van Hove singularities so the large intensity of the G band stems from the large density of states at Van Hove singularity points. Consequently, this observation shows the Raman spectrum of rotationally misaligned bilayer not only depends on the rotation angle θ but also depends on the excitation wavelength.

A-B stacked bilayer graphene, as discussed in the first chapter, possesses a 2D band consisting of four Lorentzian components and a full width at half maximum (FWHM) of 50 cm^{-1}. The distinctive 2D band characteristics of A-B stacked bilayer graphene are often used to distinguish bilayer from monolayer graphene. In comparison, the 2D FWHM of rotationally misaligned bilayer depends on θ. Figure 4.5(a) shows the 2D band FWHM of rotationally misaligned bilayer graphene vs. θ measured using a λ = 633 nm laser [97]. At large θ, the 2D band FWHM of rotationally misaligned bilayer is similar to that of monolayer graphene (30 cm^{-1}) while at smaller θ, the 2D band FWHM increases and shows a local peak at $\theta \cong 10°$, where the excitation wavelength matches the Van Hove singularity point energy difference. Figure 4.5(b) shows the intervalley scattering mechanisms associated with the 2D band of rotationally misaligned bilayer graphene. The blue (black) arrows correspond to the condition at which laser excitation energy is smaller (larger) than energy difference between conduction and valance band Van Hove singularities. The increment of the 2D band FWHM at small rotational angles, $\theta < 5°$, can be explained by complex constructive/destructive interferences of Raman

scattering modes at small rotational angles where the interaction between two layers is stronger [97].

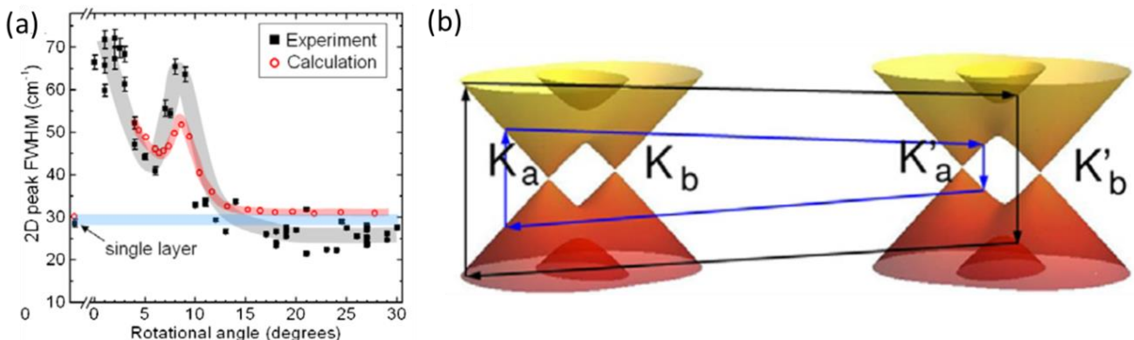

Figure 4.5: (a) Experimental (black symbols) and theoretically calculated (red symbol) rotationally misaligned bilayer graphene 2D band FWHM vs. rotational misalignment angle θ. The horizontal line represents the 2D band FWHM of monolayer graphene. The grey and red lines are guides to the eye. (b) Intervalley 2D Raman scattering processes for rotationally misaligned bilayer graphene in which the laser excitation energy is smaller (blue lines) or larger (black lines) than the energy difference between conduction and valence Van Hove singularities (Figure and caption adapted from Ref. [97]).

While electron transport in natural bilayer graphene has been explored to a large extent, the transport properties of grown graphene bilayers remain to be fully explored. Recent studies have reported the growth of bilayer graphene on SiC and metal substrates by chemical vapor deposition (CVD). Bilayer graphene grown on SiC substrates has been shown to be Bernal stacked when grown on the Si-face [99], [100] and rotationally misaligned when grown on the C-face [101]. While several recent studies suggest the growth of A-B stacked bilayer on metal substrates based on Raman spectroscopy [102]–[105], evidence of stacking from electron transport data in grown bilayer graphene has

been scant. It is therefore interesting to probe the electronic properties of CVD-grown graphene bilayers, which in turn can shed light on the growth mechanism and help assess its potential for device applications.

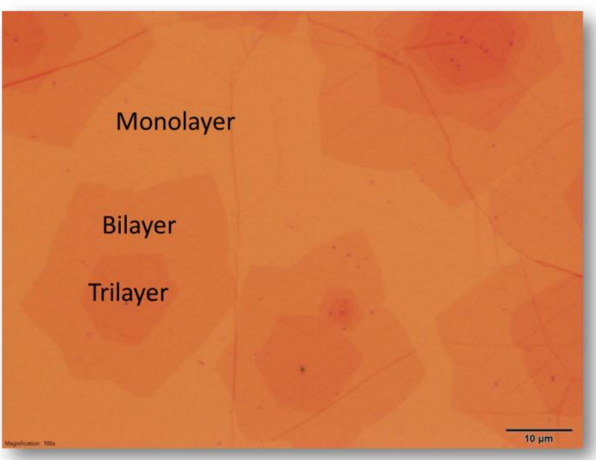

Figure 4.6: Optical micrograph of a CVD-grown multi-layer graphene sample after transfer onto a 285-nm thick SiO_2 on Si substrate. Monolayer, bilayer, and trilayer regions are marked.

In this chapter, we provide a systematic investigation of the quantum Hall effect in bilayer graphene grown on Cu substrates by chemical vapor deposition. Our data show that such bilayers consist of a mixture of domains which are either Bernal stacked or are rotationally misaligned.

4.2 REALIZATION OF BACK-GATED BILAYER GRAPHENE FIELD EFFECT TRANSISTOR

4.2.1 Chemical vapor deposition of bilayer graphene

The graphene samples studied here are grown on a 25 μm-thick Cu foil at a temperature of 1035ºC by CVD, using a mixture of methane and hydrogen at the partial pressures of 0.02 mbar and 0.03 mbar, respectively. After the growth, the graphene film on one side of the Cu foil is coated with PMMA and placed in an aqueous solution of ammonia persulfate ($(NH_4)_2S_2O_8$) to dissolve the Cu on the unprotected side. The PMMA film that carries the graphene flake is rinsed several times with deionized water to minimize the chemical contamination, and then transferred onto a silicon substrate covered with 285 nm-thick thermally grown SiO_2. After the transfer, the sample is allowed to dry and the PMMA is dissolved in acetone.

Figure 4.6 shows an optical micrograph of a graphene film transferred on the SiO_2 substrate. The optical inspection indicates the presence of monolayer, bilayer, and trilayer regions.

4.2.2 Raman spectra

To probe the number of graphene layers, and obtain an initial assessment of the layer stacking, the sample is characterized by Raman spectroscopy acquired using a 488 nm excitation wavelength, 300 nm spot size, and a power lower than 0.1 mW. Figure 4.7(a) presents a representative mapping of the Raman 2D band FWHM acquired over a

30×30 μm^2 area superimposed on the optical image of the graphene film. These data reveal the presence of distinct domains on the bilayer area with either a narrow 2D band, with FWHM values between 27 and 33 cm^{-1}, or a wide 2D band, with FWHM values between 45 and 54 cm^{-1}. By comparison, the Raman 2D band FWHM measured in monolayer graphene is 28 - 30 cm^{-1} while in A-B stacked bilayer graphene it is 50 cm^{-1} [24], [51], [106]–[108]. Figure 4.7(a) data therefore suggest that the bilayer domains with narrow 2D band consist of two graphene monolayers which are rotationally misaligned (twisted bilayer), while the domains characterized by a wider 2D band consist of two A-B stacked monolayers. We note the two types of bilayer domains of Fig. 4.7(a) show no obvious differences in optical contrast. Figure 4.7(b) shows samples of Raman spectra acquired on the same sample of Fig. 4.7(b), at different positions on the monolayer, the rotationally misaligned bilayer, and the A-B stacked bilayer regions, as indicated. The 2D band FWHM of these Raman spectra are 28 cm^{-1}, 30 cm^{-1}, and 50 cm^{-1}, respectively. The 2D band intensity (I_{2D}) is larger than the G band intensity (I_G) on the monolayer and bilayer domains with narrow 2D band, an observation which agrees with Raman spectroscopy results for exfoliated graphene [51], [106]. In contrast, the bilayer domain with a wide 2D band shows an I_{2D}/I_G ratio lower than 1. The D band, located at a Raman shift of 1350 cm^{-1} is either absent or very weak, indicating that the defect density of the CVD-grown and transferred graphene is low. Figure 4.7(c) shows a histogram of the 2D band FWHM values acquired over a 15×20 μm^2 bilayer graphene grain characterized by a wide 2D band. The data points range between 45 cm^{-1} and 65 cm^{-1}, with a maximum at 53 cm^{-1}. Figure 4.7(d) presents a typical spectrum of the 2D band

selected from the bilayer graphene region with a wide 2D band. The 2D band spectrum of Fig. 4.7(d) could not be fitted with a single Lorentzian function, but an excellent fit is obtained using four Lorentzian functions. The combined data of Fig. 4.7(a-d) therefore suggest that bilayer domains with narrow 2D band consist of rotationally misaligned graphene monolayers, while the bilayer domains with wide 2D band are two A-B stacked monolayers. We next focus on the electron transport and quantum Hall effect in these two types of bilayers.

4.2.3 Device fabrication

After the graphene is characterized by Raman spectroscopy, we fabricate back-gated Hall bar devices on selected bilayer domains with a uniform 2D band FWHM, which is either narrow (27 - 33 cm^{-1}) or wide (45 – 65 cm^{-1}). The active region of the Hall bar is defined by electron-beam (e-beam) lithography and isolated from the rest of the film using oxygen plasma etching. Metal (Ni) contacts are defined by a second e-beam lithography, metal deposition, and lift-off. An example of a Hall bar device made on a bilayer graphene is shown in Fig. 4.8(a).

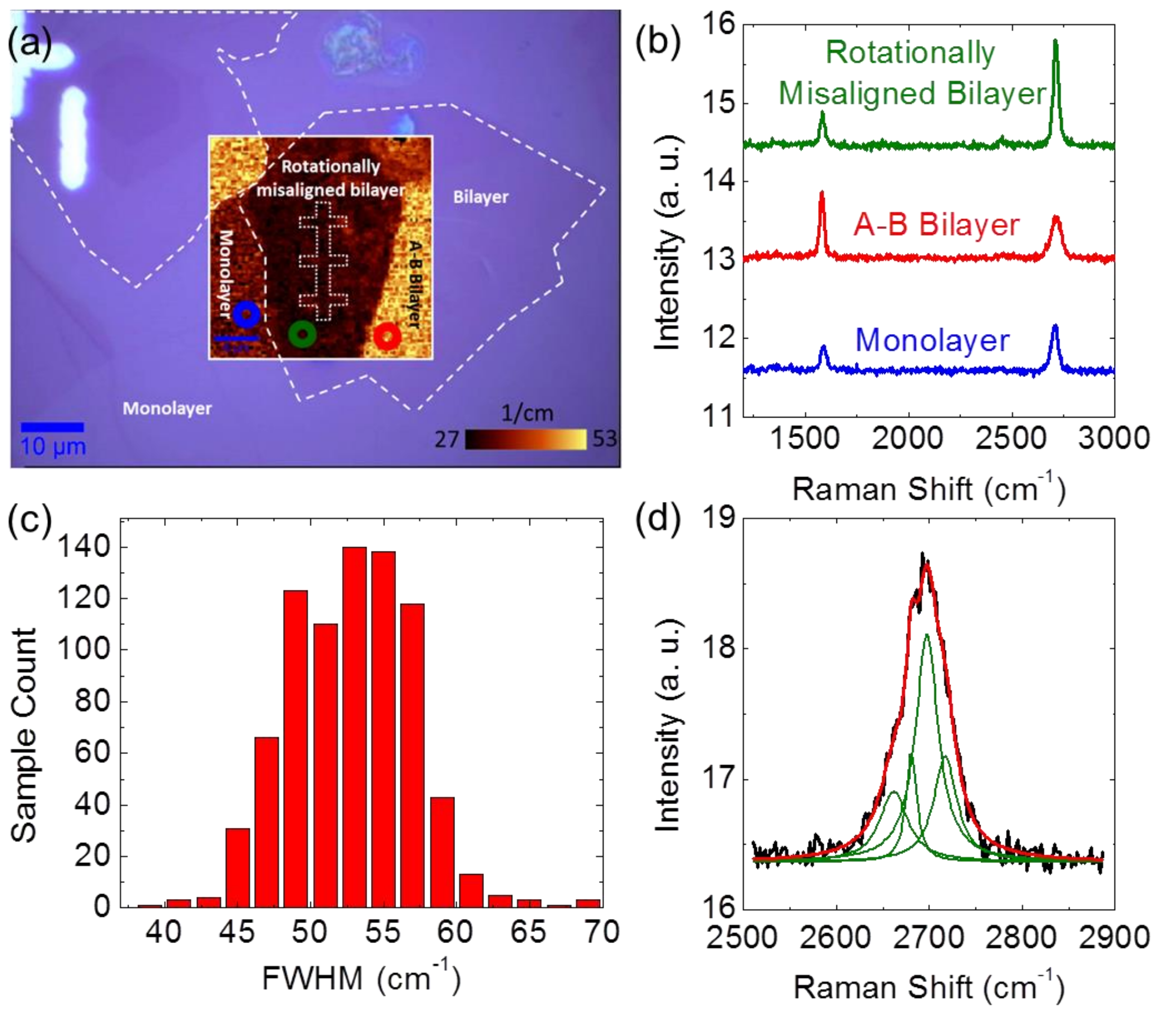

Figure 4.7: (a) 2D band FWHM spatial map reveals the bilayer is a mixture of domains with either wide (45 - 54 cm^{-1}) or narrow (27 – 33 cm^{-1}) 2D band. Dashed lines mark the boundaries of the bilayer domains and the dotted line marks a Hall bar subsequently fabricated to probe electron transport in individual bilayer regions. (b) Raman spectra acquired at three different positions, as marked in panel (a) show the G ($\simeq$ 1580 cm^{-1}) and 2D ($\simeq$ 2700 cm^{-1}) bands. (c) Histogram of the 2D band FWHM on a bilayer domain with wide 2D band. The average 2D FWHM is 53 $\pm$ 2 cm^{-1}. (d) Example of a 2D band spectrum (black line) acquired on a A-B stacked bilayer domain. A fit (red) using four Lorentzian functions (green) provide a very good match to the experimental data.

4.3 CHARACTERIZATION

4.3.1 Conductivity measurement and carrier mobility

Figures 4.8(b,c) show the four-point conductivity (σ) vs. back-gate voltage (V_{BG}) of A-B stacked [panel (b)] and rotationally misaligned [panel (c)] bilayer graphene measured at room temperature and under vacuum. The carrier mobility (μ) of each sample is determined from the four-point conductivity dependence on back-gate bias, $\mu = 1/C_{BG} \times d\sigma/dV_{BG}$; C_{BG} is the back-gate capacitance per unit area. For the samples examined in this study C_{BG} = 14.4 nFcm^{-2}, a value which is measured on 100×100 μm^2 metal pads deposited in close proximity of the Hall bar devices, and also confirmed by Hall measurements.

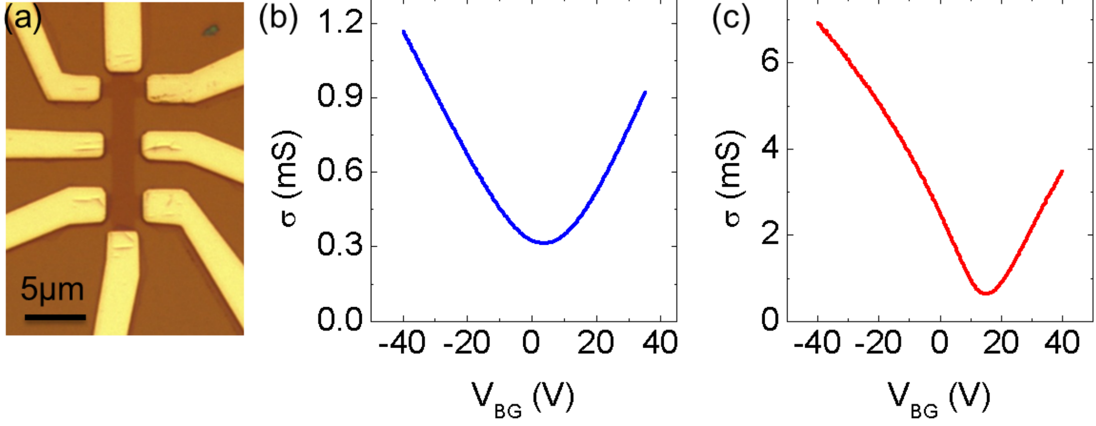

Figure 4.8: (a) Optical micrograph of a back-gated Hall bar fabricated on bilayer graphene. An example of conductivity vs. V_{BG} of (b) A-B stacked bilayer (c) rotationally misaligned bilayer graphene measured at room temperature.

The extracted mobility of the A-B stacked bilayer graphene devices are in the 700 - 1,800 $cm^2V^{-1}s^{-1}$ range, and rotationally misaligned bilayers exhibit mobility values in the 3,400 - 3,700 $cm^2V^{-1}s^{-1}$ range. The higher mobility in rotationally misaligned bilayers by comparison to A-B stacked bilayers can be explained by differences in their bandstructure, which forbid electron back-scattering in monolayer graphene, and hence in rotationally misaligned bilayer graphene, but allow back-scattering in A-B stacked bilayer graphene [109].

4.3.2 Quantum Hall effect in CVD-grown bilayer graphene

4.3.2.1 *A-B stacked bilayer graphene*

To establish the layer stacking of the CVD-grown graphene bilayers and explore their electronic properties, in the following we discuss quantum Hall effect measurements in this system. Magnetotransport measurements were carried out in perpendicular magnetic fields (B) up to 31 T, using a pumped ^{3}He refrigerator with a base temperature T = 0.3 K, and small signal, low frequency lock-in techniques. Figure 4.9(a) shows the longitudinal (ρ_{xx}) and Hall resistivity (ρ_{xy}) as a function of V_{BG} measured at a perpendicular magnetic field B = 25 T and T = 0.3 K in a graphene bilayer that displays a Raman signature consistent with A-B stacking, i.e. wide 2D band. The data shows clear quantum Hall states (QHSs), marked by vanishing ρ_{xx} and quantized ρ_{xy} at filling factors $\nu = \pm 4$ and $\nu = -8$. The filling factors are determined from the ρ_{xy} plateau values,

which are equal to $h/\nu e^2$; h is Planck's constant and e the electron charge. Alternatively, the filling factor can be calculated using $\nu = nh/eB$, where n is the total carrier density calculated by $n = C_{BG}(V_{BG} - V_{BG-CNP})/e$; V_{BG-CNP} is the gate bias at the charge neutrality point.

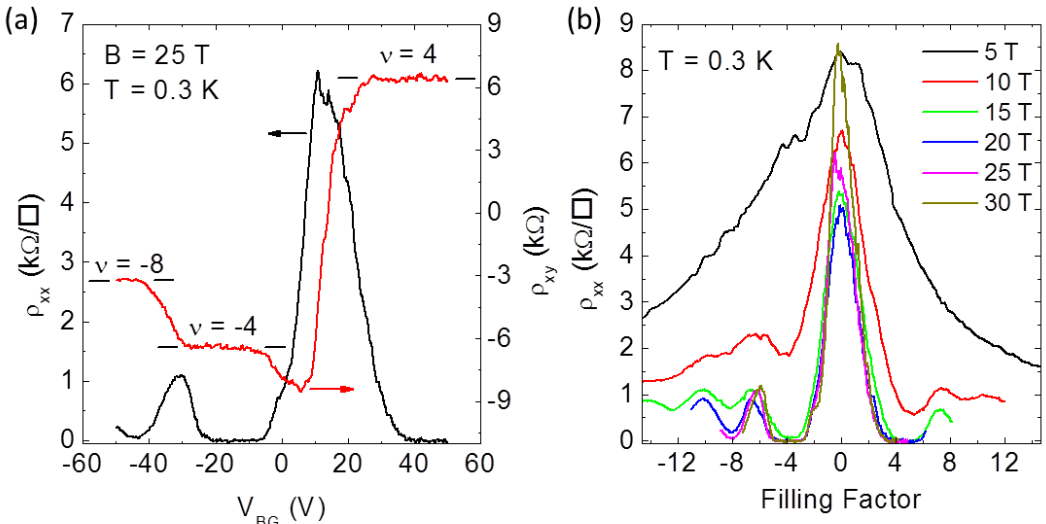

Figure 4.9: (a) ρ_{xx} and ρ_{xy} vs. V_{BG}, measured at $B = 25\,T$, and $T = 0.3\,K$. The data shows QHSs, marked by vanishing ρ_{xx} and quantized ρ_{xy} at filling factors $\nu = \pm 4$ and $\nu = -8$. (b) ρ_{xx} vs. ν measured at $T = 0.3\,K$, and at different B-field values, illustrating the emergence of QHSs at integer filling factors multiple of four with increasing the B-field.

Figure 4.9(b) shows the ρ_{xx} vs. ν measured in the same sample at different B values, and at T = 0.3 K. The data show the emergence of QHSs at integer filling factors that are multiples of four, i.e. $\nu = \pm 4, -8, -12$, thanks to the fourfold degeneracy of each Landau level (LL) associated with the spin and valley degrees of freedom [8]. The

QHSs filling factors of Fig. 4.9(a,b) are consistent with the expected values in natural bilayer graphene [8], [25], in effect fingerprinting A-B stacked bilayer.

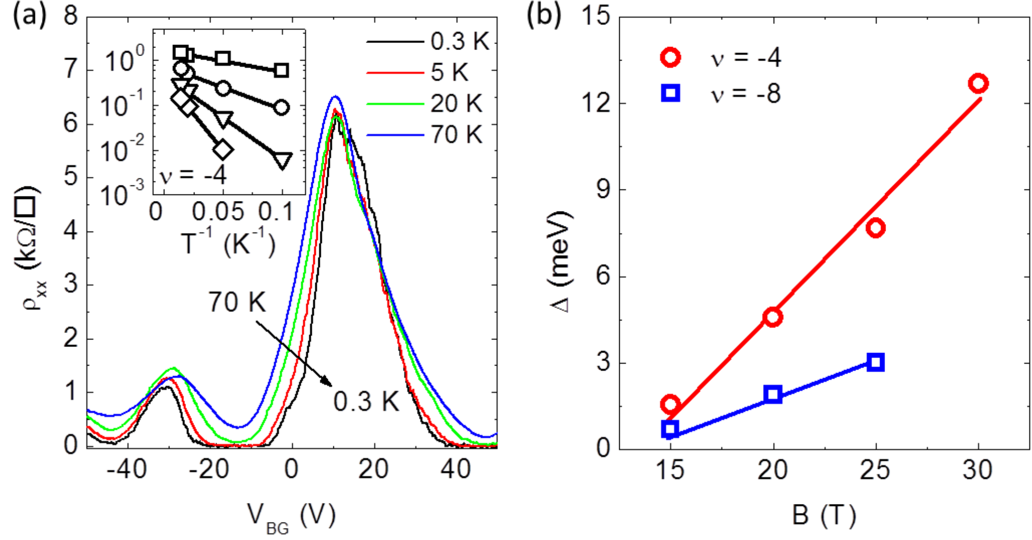

Figure 4.10: (a) ρ_{xx} vs. V_{BG} measured at different temperatures, and at $B = 25\,T$. Inset: ρ_{xx} vs. T^{-1} at $\nu = -4$ on a log-lin scale, measured at $B = 15\,T$ (□), $20\,T$ (○), $25\,T$ (▿), $30\,T$ (◇). (b) Δ vs. B, for $\nu = -4$ and $\nu = -8$ QHSs. The solid lines are guide to the eye.

Figure 4.10(a) shows ρ_{xx} vs. V_{BG} measured at B = 25 T, and at different temperatures. Although the $\nu = \pm 4, -8$ QHSs weaken with increasing T, these QHSs remain clearly visible at the highest temperature, T = 70 K. The inset of Fig. 4.10(a) shows the Arrhenius plot of ρ_{xx} measured at $\nu = -4$, and at B = 15, 20, 25, 30 T. These data follow a thermally activated behavior, $\rho_{xx} \propto e^{-\Delta/(2k_BT)}$, where Δ is the energy gap and k_B is Boltzmann's constant. Figure 4.10(b) shows the extracted $\nu = -4, -8$ QHSs

energy gaps vs. B. The data follow a linear dependence of Δ as a function of B, with the Δ values approaching 0 at $B \simeq 13$ T. The QHS energy gaps of Fig. 4.10(b) are considerably smaller than theoretical values [110]. For example, the theoretically expected energy gap of $\nu = -4$ at B = 30 T is 108 meV, a value roughly eight times larger than the experimental value. The $\nu = -4$ and $\nu = -8$ QHSs energy gaps probed in CVD-grown bilayer graphene are also approximately fivefold smaller than values typically measured in exfoliated bilayer graphene on SiO_2 substrates [111], [112].

4.3.2.2 *Rotationally misaligned bilayer graphene*

We now turn to the magneto-transport properties of the rotationally misaligned bilayer graphene samples, fabricated on bilayer graphene domains with a narrow Raman 2D band. Figure 4.11(a) shows an example of ρ_{xx} and ρ_{xy} vs. B data, measured in a rotationally misaligned bilayer device at V_{BG} = -40 V, corresponding to n = -9.7×10^{12} cm^{-2}, and at T = 0.3 K; the sample mobility is μ = 6,500 $cm^2V^{-1}s^{-1}$. These data possess several noteworthy features. First, the ρ_{xx} vs. B data display Shubnikov-de Haas (SdH) oscillations present down to magnetic fields as low as $B \simeq 3$ T, which contrast Fig. 4.9(b) data, where QHSs are not visible at B-fields lower than 10 T. This observation can be explained by the larger monolayer graphene LL energies by comparison to bilayer graphene. Moreover, the ρ_{xx} vs. B data do not follow a QHS sequence which can be readily attributed to either monolayer ($\nu = \pm 2, 6, 10 ...$) or bilayer ($\nu = \pm 4, 8, 12 ...$),

and instead shows a beating pattern similar to the QHSs superposition of a multisubband system, consistent with parallel electron transport in two independent graphene monolayers.

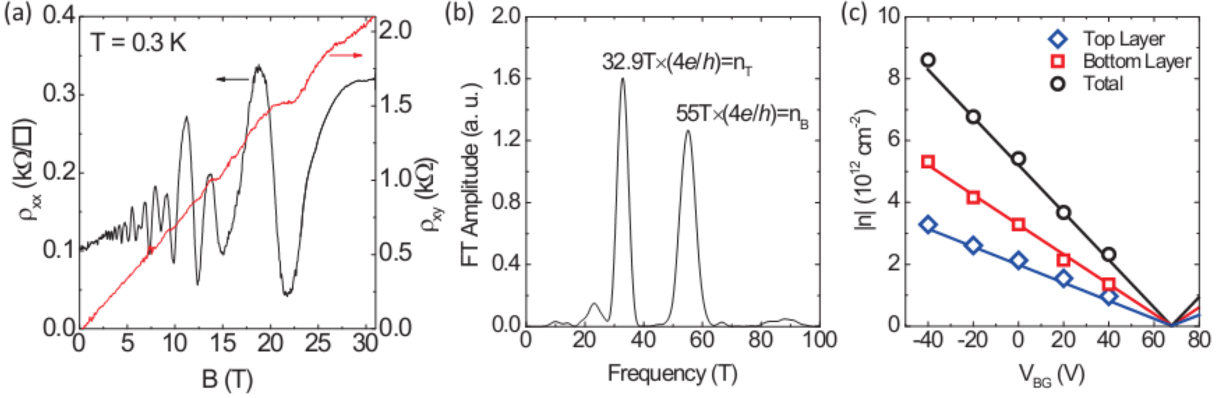

Figure 4.11: (a) ρ_{xx} and ρ_{xy} vs. B measured at $n = -9.7 \times 10^{12}\ cm^{-2}$ and at $T = 0.3\,K$. The SdH oscillations stem from a QHSs superposition of the two decoupled graphene monolayers. (b) Fourier transform of ρ_{xx} vs. B^{-1} data. The two peaks represent the layer densities, up to a factor 4e/h. (c) Top layer, bottom layer, and total carrier densities of the rotationally misaligned bilayer graphene vs. V_{BG}. The symbols (lines) represent experimental data (calculations).

To determine the subband (layer) density in a rotationally misaligned bilayer, we examined the Fourier transform (FT) of ρ_{xx} vs. B^{-1} data, calculated by first re-plotting the ρ_{xx} vs. B data, subtracting a linear fit background to center the ρ_{xx} vs. B^{-1} data around zero, and then applying a fast Fourier transform algorithm. Figure 4.11(b) shows the FT amplitude vs. B corresponding to Fig. 4.11(a) data. These data show two prominent peaks, which yield the two layer densities, up to a factor 4(e/h) = 9.67×10^{10}

cm^{-2}T^{-1}. Figure 4.8(c) summarizes the layer and total densities as a function of V_{BG}. We attribute the higher (lower) density to the bottom (top) layer, as it lies closer (farther) with respect to the back-gate. Both layer densities go to zero at V_{BG-CNP} = 68 V.

To understand the top (n_T) and bottom (n_B) layer density dependence on V_{BG} in rotationally misaligned bilayer graphene, we employ the model introduced in chapter 3. The applied V_{BG} is distributed partly across the SiO_2 dielectric and partly on the chemical potential of the bottom layer:

$$e(V_{BG} - V_{BG-CNP}) = e^2(n_B + n_T)/C_{BG} + \mu_B(n_B) \qquad (4.6)$$

here $\mu_B(n) = sgn(n)\hbar v_F\sqrt{\pi|n|}$ is the bottom layer chemical potential (Fermi energy) relative to the charge neutrality point in monolayer graphene at a carrier density n; sgn represents the sign function. Similarly, the bottom layer chemical potential is the sum of the electrostatic potential difference between the layers and the chemical potential of the top layer:

$$\mu_B(n_B) = e^2 n_T/C_{int} + \mu_T(n_T) \qquad (4.7)$$

where C_{int} is the interlayer capacitance and $\mu_T(n)$ is the top layer chemical potential relative to the charge neutrality point. Using eqs. 4.6 and 4.7 and C_{int} as a fitting parameter, we calculate n_T and n_B as a function of V_{BG}. An excellent fit to the experimental data is obtained for C_{int} = 6.9 μFcm^{-2} [solid lines in Fig. 4.9(c)].

Remarkably, this value is in good agreement with the interlayer capacitance expected theoretically for A-B stacked bilayer [79] suggesting that the separation of the two layers in rotationally misaligned bilayer graphene is close to that of A-B stacked bilayer. Two previous experimental studies [113], [114] which examined electron transport in rotationally misaligned bilayer graphene consisting of two exfoliated graphene monolayers reported C_{int} values of 0.6 μFcm^{-2} [113], and 6.8 μFcm^{-2} [114].

Figure 4.12(a) shows the ρ_{xx} contour plot as a function of V_{BG} and B probed in the rotationally misaligned bilayer sample of Fig. 4.11. The charge neutrality point is reached at back-gate bias V_{Bg-CNP} = 68 V. The data show a QHS pattern which stems from the QHSs superposition of the two decoupled monolayers. To map the position of the observed QHSs, we use eqs. 4.6 and 4.7 to calculate the layers densities as a function of V_{BG} and B, with the only difference that the chemical potential depends on both density and magnetic field as $\mu(n) = E_N$, where $E_N = sgn(N)v_F\sqrt{2e\hbar B|N|}$is the energy of the Nth LL in monolayer graphene, and $N = Int[nh/4eB]$ is the LL index; Int is the nearest integer function. Using C_{int} = 6.9 μFcm^{-2} extracted from Fig. 4.8 data analysis, we calculate n_B and n_T at fixed B and V_{BG} values, which are then converted into layer filling factors $\nu_{T,B} = n_{T,B}h/eB$. The black (red) lines in Fig. 4.12(a) represent the calculated position of half-filled LLs, i.e. $\nu_{T,B} = \pm 0, 4, 8, 12 \ldots$ for the bottom (top) layer. The ρ_{xx} maxima are in excellent agreement with the calculations, quantitatively confirming that the QHS sequence of rotationally misaligned bilayer graphene is a superposition of the QHSs of the two graphene monolayers.

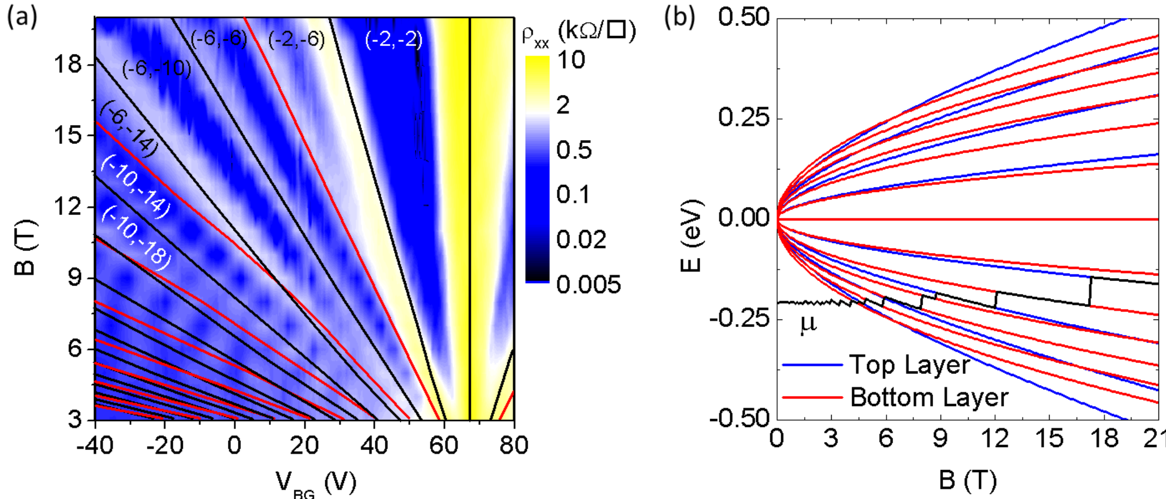

Figure 4.12: (a) rotationally misaligned bilayer ρ_{xx} contour plot as a function of V_{BG} and B. The red (black) lines are the calculated position of $\nu = \pm 0, 4, 8, 12 \ldots$ LLs of the top (bottom) layer. The layer filling factors (ν_T, ν_B) are indicated for each QHS (b) Landau level fan diagram of the top (blue), and bottom (red) graphene layers as a function of B. The black line shows the chemical potential of the bilayer device at $V_{BG} - V_{BG-CNP} = -50\,V$. Each step in the chemical potential marks a quantum Hall state.

Figure 4.12(b) shows the Landau level fan out diagram of a rotationally misaligned bilayer graphene and the calculated chemical potential of the device (relative to the Dirac point of the bottom layer) as a function of B, at a fixed back gate bias $V_{BG} =$ 18 V ($V_{BG} - V_{BG-CNP} = -50\,V$). At a constant back-gate voltage the number of occupied LLs decreases with increasing the B-field, and the chemical potential follows a zigzag trajectory between the individual LLs of the two graphene layers.

4.4 Summary

In summary, using a combination of Raman spectroscopy and magnetotransport measurements we established that CVD-grown bilayer graphene on Cu consists of a mixture of A-B stacked and rotationally misaligned monolayer domains. The A-B stacked domains show QHSs at filling factors $\nu = 4, 8, 12$ in agreement with data in exfoliated bilayer graphene. The rotationally misaligned bilayer graphene domains display a superposition of the individual QHSs of two grapehene monolayers, which allows us to extract the layer densities and inter-layer capacitance. The layer stacking determined from magnetotransport data correlates with the FWHM of the Raman 2D band.

APPENDIX: LIST OF PUBLICATIONS

1. K. Kim, S. Larentis, B. Fallahazad, K. Lee, J. Xue, D. C. Dillen, C. M. Corbet, E. Tutuc, "Band Alignment in WSe2-Graphene Heterostructures," *ACS Nano*, in press (DOI: 0.1021/acsnano.5b01114).
2. S. Kang, B. Fallahazad, K. Lee, H. Movva, K. Kim, C. Corbet, T. Taniguchi, K. Watanabe, L. Colombo, L. Register, E. Tutuc, S. Banerjee, "Bilayer Graphene-Hexagonal Boron Nitride Heterostructure Negative Differential Resistance Interlayer Tunnel FETs," *IEEE Elec. Devi. Lett.,* 36, 405 (2015).
3. B. Fallahazad, K. Lee, S. Kang, J. Xue, S. Larentis, C. Corbet, K. Kim, H. C. P. Movva, T. Taniguchi, K. Watanabe, L. F. Register, S. K. Banerjee, E. Tutuc, "Gate-Tunable Resonant Tunneling in Double Bilayer Graphene Heterostructures," *Nano Lett.* 15, 428 (2015).
4. K. Lee, B. Fallahazad, J. Xue, D. C. Dillen, K. Kim, T. Taniguchi, K. Watanabe, E. Tutuc, "Chemical Potential and Quantum Hall Ferromagnetism in Bilayer Graphene," *Science,* 345, 58 (2014).
5. S. Larentis, J. R. Tolsma, B. Fallahazad, D. C. Dillen, K. Kim, A. H. Macdonald, E. Tutuc, "Band Offset and Negative Compressibility in Graphene-MoS_2 Heterostructures," *Nano Lett.* 14, 2039 (2014).
6. Y. Hao, M. S. Bharathi, L. Wang, Y. Liu, H. Chen, S. Nie, X. Wang, H. Chou, C. Tan, B. Fallahazad, H. Ramanarayan, E. Tutuc, B. I. Yakobson, K. F. McCarty, Y.-W. Zhang, P. Kim, J. Hone, L. Colombo, and R. S. Ruoff, "The Role of Surface Oxygen in the Growth of Large Single-Crystal Graphene on Copper," *Science*, 342, 720 (2013).
7. E.-S. Liu, D. C. Dillen, J. Nah, B. Fallahazad, K. Kim, and E. Tutuc, "Realization and Scaling of Ge-$Si_{1-x}Ge_x$ Core-Shell Nanowire n-FETs," *IEEE Trans. on Elec. Dev.*, 60, 4027 (2013).
8. K. Lee, B. Fallahazad, H. Min, and E. Tutuc, "Transport Gap in Dual-Gated Graphene Bilayers Using Oxides as Dielectrics," *IEEE Trans. on Elec. Dev.*, 60, 103 (2013).
9. S. Larentis, B. Fallahazad, and E. Tutuc, "Field-Effect Transistors and Intrinsic Mobility in Ultra-Thin $MoSe_2$ Layers," *Appl. Phys. Lett.*, 101, 223104 (2012).
10. B. Fallahazad, Y. Hao, K. Lee, S. Kim, R. S. Ruoff, and E. Tutuc, "Quantum Hall effect in Bernal Stacked and Twisted Bilayer Graphene Grown on Cu by Chemical Vapor Deposition," *Phys. Rev. B*, 85, 201408 (2012).

11. S. Kim, I. Jo, D. C. Dillen, D. A. Ferrer, B. Fallahazad, Z. Yao, S. K. Banerjee, and E. Tutuc, “Direct Measurement of the Fermi Energy in Graphene Using a Double-Layer Heterostructure,” *Phys. Rev. Lett.*, 108, 116404 (2012).
12. B. Fallahazad, K. Lee, G. Lian, S. Kim, C. M. Corbet, D. A. Ferrer, L. Colombo, and E. Tutuc, “Scaling of Al_2O_3 dielectric for graphene field-effect transistors,” *Appl. Phys. Lett.*, 100, 093112 (2012).
13. O. Gunawan, K. Wang, B. Fallahazad, Y. Zhang, E. Tutuc, S. Guha, "High Performance Wire-Array Silicon Solar Cells," *Progress in Photovoltaics: Research and Applications*, 19, 307 (2011).
14. B. Fallahazad, S. Kim, L. Colombo, and E. Tutuc, “Dielectric Thickness Dependence of Carrier Mobility in Graphene with HfO_2 Top Dielectric,” *Appl. Phys. Lett.*, 97, 123105 (2010).
15. K. Wang, O. Gunawan, N. Moumen, G. Tulevski, H. Mohamed, B. Fallahazad, E. Tutuc, and S. Guha, "Wire Textured, Multi-Crystalline Si Solar Cells Created Using Self-Assembled Masks," *Optics Express*, 18, A568 (2010).
16. Hosseini, D. Kwong, Y. Zhang, S. A. Chandorkar, F. Crnogorac, A. Carlson, B. Fallah, S. Bank, E. Tutuc, J. Rogers, R. Fabian W. Pease, and R. T. Chen, "On the Fabrication of Three-Dimensional Silicon-on-Insulator Based Optical Phased Array for Agile and Large Angle Laser Beam Steering System," *J. Vac. Sci. Technol. B*, 28, C6O1 (2010).

REFRENCES

[1] K. S. Novoselov, A. K. Geim, S. V. Morozov, D. Jiang, Y. Zhang, S. V. Dubonos, I. V. Grigorieva, and A. A. Firsov, “Electric Field Effect in Atomically Thin Carbon Films,” *Science*, vol. 306, no. 5696, pp. 666–669, Oct. 2004.

[2] R. Peierls, “Quelques propriétés typiques des corps solides,” *Ann. Inst. Henri Poincaré*, vol. 5, no. 3, pp. 177–222, 1935.

[3] P. Ehrenfreund and B. H. Foing, “Fullerenes and Cosmic Carbon,” *Science*, vol. 329, no. 5996, pp. 1159–1160, Sep. 2010.

[4] A. H. Castro Neto, F. Guinea, N. M. R. Peres, K. S. Novoselov, and A. K. Geim, “The electronic properties of graphene,” *Rev. Mod. Phys.*, vol. 81, no. 1, pp. 109–162, Jan. 2009.

[5] J. M. B. Lopes dos Santos, N. M. R. Peres, and A. H. Castro Neto, “Graphene Bilayer with a Twist: Electronic Structure,” *Phys. Rev. Lett.*, vol. 99, no. 25, p. 256802, Dec. 2007.

[6] J. M. B. Lopes dos Santos, N. M. R. Peres, and A. H. Castro Neto, “Continuum model of the twisted graphene bilayer,” *Phys. Rev. B*, vol. 86, no. 15, p. 155449, Oct. 2012.

[7] E. J. Mele, “Commensuration and interlayer coherence in twisted bilayer graphene,” *Phys. Rev. B*, vol. 81, no. 16, p. 161405, Apr. 2010.

[8] E. McCann and V. I. Fal’ko, “Landau-Level Degeneracy and Quantum Hall Effect in a Graphite Bilayer,” *Phys. Rev. Lett.*, vol. 96, no. 8, p. 086805, Mar. 2006.

[9] E. McCann, “Asymmetry gap in the electronic band structure of bilayer graphene,” *Phys. Rev. B*, vol. 74, no. 16, p. 161403, Oct. 2006.

[10] K. S. Novoselov, A. K. Geim, S. V. Morozov, D. Jiang, M. I. Katsnelson, I. V. Grigorieva, S. V. Dubonos, and A. A. Firsov, “Two-dimensional gas of massless Dirac fermions in graphene,” *Nature*, vol. 438, no. 7065, pp. 197–200, Nov. 2005.

[11] K. Nomura and A. H. MacDonald, “Quantum Transport of Massless Dirac Fermions,” *Phys. Rev. Lett.*, vol. 98, no. 7, p. 076602, Feb. 2007.

[12] K. Ziegler, “Robust Transport Properties in Graphene,” *Phys. Rev. Lett.*, vol. 97, no. 26, p. 266802, Dec. 2006.

[13] I. L. Aleiner and K. B. Efetov, “Effect of Disorder on Transport in Graphene,” *Phys. Rev. Lett.*, vol. 97, no. 23, p. 236801, Dec. 2006.

[14] A. Altland, “Low-Energy Theory of Disordered Graphene,” *Phys. Rev. Lett.*, vol. 97, no. 23, p. 236802, Dec. 2006.

[15] P. M. Ostrovsky, I. V. Gornyi, and A. D. Mirlin, “Electron transport in disordered graphene,” *Phys. Rev. B*, vol. 74, no. 23, p. 235443, Dec. 2006.

[16] S. Adam, E. H. Hwang, V. M. Galitski, and S. D. Sarma, “A self-consistent theory for graphene transport,” *Proc. Natl. Acad. Sci.*, vol. 104, no. 47, pp. 18392–18397, Nov. 2007.

[17] E. H. Hwang, S. Adam, and S. D. Sarma, “Carrier Transport in Two-Dimensional Graphene Layers,” *Phys. Rev. Lett.*, vol. 98, no. 18, p. 186806, May 2007.

[18] S. Adam, E. H. Hwang, E. Rossi, and S. Das Sarma, “Theory of charged impurity scattering in two-dimensional graphene,” *Solid State Commun.*, vol. 149, no. 27–28, pp. 1072–1079, Jul. 2009.
[19] S. Adam, E. H. Hwang, and S. Das Sarma, “Scattering mechanisms and Boltzmann transport in graphene,” *Phys. E Low-Dimens. Syst. Nanostructures*, vol. 40, no. 5, pp. 1022–1025, Mar. 2008.
[20] S. Das Sarma, S. Adam, E. H. Hwang, and E. Rossi, “Electronic transport in two-dimensional graphene,” *Rev. Mod. Phys.*, vol. 83, no. 2, pp. 407–470, May 2011.
[21] E. H. Hwang and S. Das Sarma, “Dielectric function, screening, and plasmons in two-dimensional graphene,” *Phys. Rev. B*, vol. 75, no. 20, p. 205418, May 2007.
[22] F. Tuinstra and J. L. Koenig, “Raman Spectrum of Graphite,” *J. Chem. Phys.*, vol. 53, no. 3, pp. 1126–1130, Aug. 1970.
[23] M. Lazzeri, C. Attaccalite, L. Wirtz, and F. Mauri, “Impact of the electron-electron correlation on phonon dispersion: Failure of LDA and GGA DFT functionals in graphene and graphite,” *Phys. Rev. B*, vol. 78, no. 8, p. 081406, Aug. 2008.
[24] L. M. Malard, M. A. Pimenta, G. Dresselhaus, and M. S. Dresselhaus, “Raman spectroscopy in graphene,” *Phys. Rep.*, vol. 473, no. 5–6, pp. 51–87, Apr. 2009.
[25] K. S. Novoselov, E. McCann, S. V. Morozov, V. I. Fal’ko, M. I. Katsnelson, U. Zeitler, D. Jiang, F. Schedin, and A. K. Geim, “Unconventional quantum Hall effect and Berry’s phase of 2π in bilayer graphene,” *Nat. Phys.*, vol. 2, no. 3, pp. 177–180, Mar. 2006.
[26] R. Chau, S. Datta, M. Doczy, B. Doyle, J. Kavalieros, and M. Metz, “High-kappa;/metal-gate stack and its MOSFET characteristics,” *IEEE Electron Device Lett.*, vol. 25, no. 6, pp. 408–410, Jun. 2004.
[27] C. Berger, Z. Song, T. Li, X. Li, A. Y. Ogbazghi, R. Feng, Z. Dai, A. N. Marchenkov, E. H. Conrad, P. N. First, and W. A. de Heer, “Ultrathin Epitaxial Graphite: 2D Electron Gas Properties and a Route toward Graphene-based Nanoelectronics,” *J. Phys. Chem. B*, vol. 108, no. 52, pp. 19912–19916, Dec. 2004.
[28] D. Gunlycke, H. M. Lawler, and C. T. White, “Room-temperature ballistic transport in narrow graphene strips,” *Phys. Rev. B*, vol. 75, no. 8, p. 085418, Feb. 2007.
[29] T. J. Booth, P. Blake, R. R. Nair, D. Jiang, E. W. Hill, U. Bangert, A. Bleloch, M. Gass, K. S. Novoselov, M. I. Katsnelson, and A. K. Geim, “Macroscopic Graphene Membranes and Their Extraordinary Stiffness,” *Nano Lett.*, vol. 8, no. 8, pp. 2442–2446, Aug. 2008.
[30] K. I. Bolotin, K. J. Sikes, Z. Jiang, M. Klima, G. Fudenberg, J. Hone, P. Kim, and H. L. Stormer, “Ultrahigh electron mobility in suspended graphene,” *Solid State Commun.*, vol. 146, no. 9–10, pp. 351–355, Jun. 2008.
[31] J.-H. Chen, C. Jang, S. Adam, M. S. Fuhrer, E. D. Williams, and M. Ishigami, “Charged-impurity scattering in graphene,” *Nat. Phys.*, vol. 4, no. 5, pp. 377–381, May 2008.

[32] M. I. Katsnelson and A. K. Geim, "Electron scattering on microscopic corrugations in graphene," *Philos. Trans. R. Soc. Lond. Math. Phys. Eng. Sci.*, vol. 366, no. 1863, pp. 195–204, Jan. 2008.
[33] J.-H. Chen, C. Jang, S. Xiao, M. Ishigami, and M. S. Fuhrer, "Intrinsic and extrinsic performance limits of graphene devices on SiO2," *Nat. Nanotechnol.*, vol. 3, no. 4, pp. 206–209, Apr. 2008.
[34] C. Jang, S. Adam, J.-H. Chen, E. D. Williams, S. Das Sarma, and M. S. Fuhrer, "Tuning the Effective Fine Structure Constant in Graphene: Opposing Effects of Dielectric Screening on Short- and Long-Range Potential Scattering," *Phys. Rev. Lett.*, vol. 101, no. 14, p. 146805, Oct. 2008.
[35] F. Chen, J. Xia, D. K. Ferry, and N. Tao, "Dielectric Screening Enhanced Performance in Graphene FET," *Nano Lett.*, vol. 9, no. 7, pp. 2571–2574, Jul. 2009.
[36] L. A. Ponomarenko, R. Yang, T. M. Mohiuddin, M. I. Katsnelson, K. S. Novoselov, S. V. Morozov, A. A. Zhukov, F. Schedin, E. W. Hill, and A. K. Geim, "Effect of a High-$$\kappa${}$ Environment on Charge Carrier Mobility in Graphene," *Phys. Rev. Lett.*, vol. 102, no. 20, p. 206603, May 2009.
[37] S. Kim, J. Nah, I. Jo, D. Shahrjerdi, L. Colombo, Z. Yao, E. Tutuc, and S. K. Banerjee, "Realization of a high mobility dual-gated graphene field-effect transistor with Al2O3 dielectric," *Appl. Phys. Lett.*, vol. 94, no. 6, p. 062107, Feb. 2009.
[38] J. Kedzierski, P.-L. Hsu, P. Healey, P. W. Wyatt, C. L. Keast, M. Sprinkle, C. Berger, and W. A. de Heer, "Epitaxial Graphene Transistors on SiC Substrates," *IEEE Trans. Electron Devices*, vol. 55, no. 8, pp. 2078–2085, Aug. 2008.
[39] M. C. Lemme, T. J. Echtermeyer, M. Baus, and H. Kurz, "A Graphene Field-Effect Device," *IEEE Electron Device Lett.*, vol. 28, no. 4, pp. 282–284, Apr. 2007.
[40] Z. Jin, Y. Su, J. Chen, X. Liu, and D. Wu, "Study of AlN dielectric film on graphene by Raman microscopy," *Appl. Phys. Lett.*, vol. 95, no. 23, p. 233110, Dec. 2009.
[41] Z. H. Ni, H. M. Wang, Y. Ma, J. Kasim, Y. H. Wu, and Z. X. Shen, "Tunable Stress and Controlled Thickness Modification in Graphene by Annealing," *ACS Nano*, vol. 2, no. 5, pp. 1033–1039, May 2008.
[42] S. M. George, A. W. Ott, and J. W. Klaus, "Surface Chemistry for Atomic Layer Growth," *J. Phys. Chem.*, vol. 100, no. 31, pp. 13121–13131, Jan. 1996.
[43] R. L. Puurunen, "Surface chemistry of atomic layer deposition: A case study for the trimethylaluminum/water process," *J. Appl. Phys.*, vol. 97, no. 12, p. 121301, Jun. 2005.
[44] Y. Xuan, Y. Q. Wu, T. Shen, M. Qi, M. A. Capano, J. A. Cooper, and P. D. Ye, "Atomic-layer-deposited nanostructures for graphene-based nanoelectronics," *Appl. Phys. Lett.*, vol. 92, no. 1, p. 013101, Jan. 2008.

[45] F. H. Yang and R. T. Yang, "Ab initio molecular orbital study of adsorption of atomic hydrogen on graphite:: Insight into hydrogen storage in carbon nanotubes," *Carbon*, vol. 40, no. 3, pp. 437–444, Mar. 2002.
[46] J. R. Williams, L. DiCarlo, and C. M. Marcus, "Quantum Hall Effect in a Gate-Controlled p-n Junction of Graphene," *Science*, vol. 317, no. 5838, pp. 638–641, Aug. 2007.
[47] Y.-M. Lin, K. A. Jenkins, A. Valdes-Garcia, J. P. Small, D. B. Farmer, and P. Avouris, "Operation of Graphene Transistors at Gigahertz Frequencies," *Nano Lett.*, vol. 9, no. 1, pp. 422–426, Jan. 2009.
[48] B. Lee, S.-Y. Park, H.-C. Kim, K. Cho, E. M. Vogel, M. J. Kim, R. M. Wallace, and J. Kim, "Conformal Al2O3 dielectric layer deposited by atomic layer deposition for graphene-based nanoelectronics," *Appl. Phys. Lett.*, vol. 92, no. 20, p. 203102, May 2008.
[49] I. Meric, C. R. Dean, A. F. Young, N. Baklitskaya, N. J. Tremblay, C. Nuckolls, P. Kim, and K. L. Shepard, "Channel Length Scaling in Graphene Field-Effect Transistors Studied with Pulsed Current−Voltage Measurements," *Nano Lett.*, vol. 11, no. 3, pp. 1093–1097, Mar. 2011.
[50] X. Wang, S. M. Tabakman, and H. Dai, "Atomic Layer Deposition of Metal Oxides on Pristine and Functionalized Graphene," *J. Am. Chem. Soc.*, vol. 130, no. 26, pp. 8152–8153, Jul. 2008.
[51] A. C. Ferrari, J. C. Meyer, V. Scardaci, C. Casiraghi, M. Lazzeri, F. Mauri, S. Piscanec, D. Jiang, K. S. Novoselov, S. Roth, and A. K. Geim, "Raman Spectrum of Graphene and Graphene Layers," *Phys. Rev. Lett.*, vol. 97, no. 18, p. 187401, Oct. 2006.
[52] P. Blake, E. W. Hill, A. H. C. Neto, K. S. Novoselov, D. Jiang, R. Yang, T. J. Booth, and A. K. Geim, "Making graphene visible," *Appl. Phys. Lett.*, vol. 91, no. 6, p. 063124, Aug. 2007.
[53] M. J. Dignam, W. R. Fawcett, and H. Böhni, "The Kinetics and Mechanism of Oxidation of Superpurity Aluminum in Dry Oxygen I . Apparatus Description and the Growth of 'Amorphous' Oxide," *J. Electrochem. Soc.*, vol. 113, no. 7, pp. 656–662, Jul. 1966.
[54] I. Vaquila, M. C. G. Passeggi Jr., and J. Ferrón, "Oxide stoichiometry in the early stages of titanium oxidation," *Surf. Sci.*, vol. 292, no. 1–2, pp. L795–L800, Jul. 1993.
[55] S. Guha and P. Solomon, "Band bending and the thermochemistry of oxygen vacancies in ionic metal oxide thin films," *Appl. Phys. Lett.*, vol. 92, no. 1, p. 012909, Jan. 2008.
[56] S. Guha and V. Narayanan, "Oxygen Vacancies in High Dielectric Constant Oxide-Semiconductor Films," *Phys. Rev. Lett.*, vol. 98, no. 19, p. 196101, May 2007.
[57] L. L. Levenson, A. B. Swartzlander, A. Yahashi, H. Usui, and I. Yamada, "Aluminum surface mobility on silicon nitride and on several silicon oxides," *J. Vac. Sci. Technol. A*, vol. 8, no. 3, pp. 1447–1452, May 1990.

[58] A. Pirkle, R. M. Wallace, and L. Colombo, "In situ studies of Al2O3 and HfO2 dielectrics on graphite," *Appl. Phys. Lett.*, vol. 95, no. 13, p. 133106, Sep. 2009.
[59] S. Jakschik, U. Schroeder, T. Hecht, M. Gutsche, H. Seidl, and J. W. Bartha, "Crystallization behavior of thin ALD-Al2O3 films," *Thin Solid Films*, vol. 425, no. 1–2, pp. 216–220, Feb. 2003.
[60] J. P. Eisenstein, L. N. Pfeiffer, and K. W. West, "Field-induced resonant tunneling between parallel two-dimensional electron systems," *Appl. Phys. Lett.*, vol. 58, no. 14, pp. 1497–1499, Apr. 1991.
[61] N. Turner, J. T. Nicholls, E. H. Linfield, K. M. Brown, G. A. C. Jones, and D. A. Ritchie, "Tunneling between parallel two-dimensional electron gases," *Phys. Rev. B*, vol. 54, no. 15, pp. 10614–10624, Oct. 1996.
[62] R. K. Hayden, D. K. Maude, L. Eaves, E. C. Valadares, M. Henini, F. W. Sheard, O. H. Hughes, J. C. Portal, and L. Cury, "Probing the hole dispersion curves of a quantum well using resonant magnetotunneling spectroscopy," *Phys. Rev. Lett.*, vol. 66, no. 13, pp. 1749–1752, Apr. 1991.
[63] J. P. Eisenstein, D. Syphers, L. N. Pfeiffer, and K. W. West, "Quantum lifetime of two-dimensional holes," *Solid State Commun.*, vol. 143, no. 8–9, pp. 365–368, Aug. 2007.
[64] S. Misra, N. C. Bishop, E. Tutuc, and M. Shayegan, "Tunneling between dilute GaAs hole layers," *Phys. Rev. B*, vol. 77, no. 16, p. 161301, Apr. 2008.
[65] J. A. Simmons, M. A. Blount, J. S. Moon, S. K. Lyo, W. E. Baca, J. R. Wendt, J. L. Reno, and M. J. Hafich, "Planar quantum transistor based on 2D–2D tunneling in double quantum well heterostructures," *J. Appl. Phys.*, vol. 84, no. 10, pp. 5626–5634, Nov. 1998.
[66] M. A. Blount, J. A. Simmons, J. S. Moon, W. E. Baca, J. L. Reno, and M. J. Hafich, "Double electron layer tunnelling transistor (DELTT)," *Semicond. Sci. Technol.*, vol. 13, no. 8A, p. A180, Aug. 1998.
[67] T. Jungwirth and A. H. MacDonald, "Electron-electron interactions and two-dimensional\char21{}two-dimensional tunneling," *Phys. Rev. B*, vol. 53, no. 11, pp. 7403–7412, Mar. 1996.
[68] L. Zheng and A. H. MacDonald, "Tunneling conductance between parallel two-dimensional electron systems," *Phys. Rev. B*, vol. 47, no. 16, pp. 10619–10624, Apr. 1993.
[69] S. Q. Murphy, J. P. Eisenstein, L. N. Pfeiffer, and K. W. West, "Lifetime of two-dimensional electrons measured by tunneling spectroscopy," *Phys. Rev. B*, vol. 52, no. 20, pp. 14825–14828, Nov. 1995.
[70] C. R. Dean, A. F. Young, I. Meric, C. Lee, L. Wang, S. Sorgenfrei, K. Watanabe, T. Taniguchi, P. Kim, K. L. Shepard, and J. Hone, "Boron nitride substrates for high-quality graphene electronics," *Nat. Nanotechnol.*, vol. 5, no. 10, pp. 722–726, Oct. 2010.
[71] A. K. Geim and I. V. Grigorieva, "Van der Waals heterostructures," *Nature*, vol. 499, no. 7459, pp. 419–425, Jul. 2013.

[72] S. Kim and E. Tutuc, “Coulomb drag and magnetotransport in graphene double layers,” *Solid State Commun.*, vol. 152, no. 15, pp. 1283–1288, Aug. 2012.

[73] R. V. Gorbachev, A. K. Geim, M. I. Katsnelson, K. S. Novoselov, T. Tudorovskiy, I. V. Grigorieva, A. H. MacDonald, S. V. Morozov, K. Watanabe, T. Taniguchi, and L. A. Ponomarenko, “Strong Coulomb drag and broken symmetry in double-layer graphene,” *Nat. Phys.*, vol. 8, no. 12, pp. 896–901, Dec. 2012.

[74] A. Mishchenko, J. S. Tu, Y. Cao, R. V. Gorbachev, J. R. Wallbank, M. T. Greenaway, V. E. Morozov, S. V. Morozov, M. J. Zhu, S. L. Wong, F. Withers, C. R. Woods, Y.-J. Kim, K. Watanabe, T. Taniguchi, E. E. Vdovin, O. Makarovsky, T. M. Fromhold, V. I. Fal’ko, A. K. Geim, L. Eaves, and K. S. Novoselov, “Twist-controlled resonant tunnelling in graphene/boron nitride/graphene heterostructures,” *Nat. Nanotechnol.*, vol. 9, pp. 808–813, Sep. 2014.

[75] L. Britnell, R. V. Gorbachev, R. Jalil, B. D. Belle, F. Schedin, A. Mishchenko, T. Georgiou, M. I. Katsnelson, L. Eaves, S. V. Morozov, N. M. R. Peres, J. Leist, A. K. Geim, K. S. Novoselov, and L. A. Ponomarenko, “Field-Effect Tunneling Transistor Based on Vertical Graphene Heterostructures,” *Science*, vol. 335, no. 6071, pp. 947–950, Feb. 2012.

[76] S. K. Banerjee, L. F. Register, E. Tutuc, D. Reddy, and A. MacDonald, “Bilayer PseudoSpin Field-Effect Transistor (BiSFET): A Proposed New Logic Device,” *IEEE Electron Device Lett.*, vol. 30, no. 2, pp. 158–160, Feb. 2009.

[77] P. Zhao, R. M. Feenstra, G. Gu, and D. Jena, “SymFET: A Proposed Symmetric Graphene Tunneling Field-Effect Transistor,” *IEEE Trans. Electron Devices*, vol. 60, no. 3, pp. 951–957, Mar. 2013.

[78] Y. Zhang, T.-T. Tang, C. Girit, Z. Hao, M. C. Martin, A. Zettl, M. F. Crommie, Y. R. Shen, and F. Wang, “Direct observation of a widely tunable bandgap in bilayer graphene,” *Nature*, vol. 459, no. 7248, pp. 820–823, Jun. 2009.

[79] H. Min, B. Sahu, S. K. Banerjee, and A. H. MacDonald, “Ab initio theory of gate induced gaps in graphene bilayers,” *Phys. Rev. B*, vol. 75, no. 15, p. 155115, Apr. 2007.

[80] K. Watanabe, T. Taniguchi, and H. Kanda, “Direct-bandgap properties and evidence for ultraviolet lasing of hexagonal boron nitride single crystal,” *Nat. Mater.*, vol. 3, no. 6, pp. 404–409, Jun. 2004.

[81] G.-H. Lee, Y.-J. Yu, C. Lee, C. Dean, K. L. Shepard, P. Kim, and J. Hone, “Electron tunneling through atomically flat and ultrathin hexagonal boron nitride,” *Appl. Phys. Lett.*, vol. 99, no. 24, p. 243114, Dec. 2011.

[82] K. Lee, B. Fallahazad, J. Xue, D. C. Dillen, K. Kim, T. Taniguchi, K. Watanabe, and E. Tutuc, “Chemical potential and quantum Hall ferromagnetism in bilayer graphene,” *Science*, vol. 345, no. 6192, pp. 58–61, Jul. 2014.

[83] L. Wang, I. Meric, P. Y. Huang, Q. Gao, Y. Gao, H. Tran, T. Taniguchi, K. Watanabe, L. M. Campos, D. A. Muller, J. Guo, P. Kim, J. Hone, K. L. Shepard, and C. R. Dean, “One-Dimensional Electrical Contact to a Two-Dimensional Material,” *Science*, vol. 342, no. 6158, pp. 614–617, Nov. 2013.

[84] A. S. Mayorov, R. V. Gorbachev, S. V. Morozov, L. Britnell, R. Jalil, L. A. Ponomarenko, P. Blake, K. S. Novoselov, K. Watanabe, T. Taniguchi, and A. K. Geim, "Micrometer-Scale Ballistic Transport in Encapsulated Graphene at Room Temperature," *Nano Lett.*, vol. 11, no. 6, pp. 2396–2399, Jun. 2011.

[85] S. Kim, I. Jo, D. C. Dillen, D. A. Ferrer, B. Fallahazad, Z. Yao, S. K. Banerjee, and E. Tutuc, "Direct Measurement of the Fermi Energy in Graphene Using a Double-Layer Heterostructure," *Phys. Rev. Lett.*, vol. 108, no. 11, p. 116404, Mar. 2012.

[86] L. Britnell, R. V. Gorbachev, R. Jalil, B. D. Belle, F. Schedin, M. I. Katsnelson, L. Eaves, S. V. Morozov, A. S. Mayorov, N. M. R. Peres, A. H. Castro Neto, J. Leist, A. K. Geim, L. A. Ponomarenko, and K. S. Novoselov, "Electron Tunneling through Ultrathin Boron Nitride Crystalline Barriers," *Nano Lett.*, vol. 12, no. 3, pp. 1707–1710, Mar. 2012.

[87] D. Reddy, L. F. Register, and S. K. Banerjee, "Bilayer graphene vertical tunneling field effect transistor," in *Device Research Conference (DRC), 2012 70th Annual*, 2012, pp. 73–74.

[88] L. Brey, "Coherent Tunneling and Negative Differential Conductivity in a Graphene/h-BN/Graphene Heterostructure," *Phys. Rev. Appl.*, vol. 2, no. 1, p. 014003, Jul. 2014.

[89] R. M. Feenstra, D. Jena, and G. Gu, "Single-particle tunneling in doped graphene-insulator-graphene junctions," *J. Appl. Phys.*, vol. 111, no. 4, p. 043711, Feb. 2012.

[90] L. M. Zhang, Z. Q. Li, D. N. Basov, M. M. Fogler, Z. Hao, and M. C. Martin, "Determination of the electronic structure of bilayer graphene from infrared spectroscopy," *Phys. Rev. B*, vol. 78, no. 23, p. 235408, Dec. 2008.

[91] S. Kang, B. Fallahazad, K. Lee, H. Movva, K. Kim, C. M. Corbet, T. Taniguchi, K. Watanabe, L. Colombo, L. F. Register, E. Tutuc, and S. K. Banerjee, "Bilayer Graphene-Hexagonal Boron Nitride Heterostructure Negative Differential Resistance Interlayer Tunnel FET," *IEEE Electron Device Lett.*, vol. 36, no. 4, pp. 405–407, Apr. 2015.

[92] Sergio de la Barrera and Randall Feenstra, "Inelastic vertical tunneling in graphene-based heterostructures," presented at the APS March Meeting, San Antonio, 2015.

[93] S. C. de la Barrera and R. M. Feenstra, "Theory of resonant tunneling in bilayer-graphene/hexagonal-boron-nitride heterostructures," *Appl. Phys. Lett.*, vol. 106, no. 9, p. 093115, Mar. 2015.

[94] E. J. Mele, "Band symmetries and singularities in twisted multilayer graphene," *Phys. Rev. B*, vol. 84, no. 23, p. 235439, Dec. 2011.

[95] E. J. Mele, "Interlayer coupling in rotationally faulted multilayer graphenes," *J. Phys. Appl. Phys.*, vol. 45, no. 15, p. 154004, Apr. 2012.

[96] G. Li, A. Luican, J. M. B. Lopes dos Santos, A. H. Castro Neto, A. Reina, J. Kong, and E. Y. Andrei, "Observation of Van Hove singularities in twisted graphene layers," *Nat. Phys.*, vol. 6, no. 2, pp. 109–113, Feb. 2010.

[97] K. Kim, S. Coh, L. Z. Tan, W. Regan, J. M. Yuk, E. Chatterjee, M. F. Crommie, M. L. Cohen, S. G. Louie, and A. Zettl, “Raman Spectroscopy Study of Rotated Double-Layer Graphene: Misorientation-Angle Dependence of Electronic Structure,” *Phys. Rev. Lett.*, vol. 108, no. 24, p. 246103, Jun. 2012.
[98] R. W. Havener, H. Zhuang, L. Brown, R. G. Hennig, and J. Park, “Angle-Resolved Raman Imaging of Interlayer Rotations and Interactions in Twisted Bilayer Graphene,” *Nano Lett.*, vol. 12, no. 6, pp. 3162–3167, Jun. 2012.
[99] C. Riedl, C. Coletti, T. Iwasaki, A. A. Zakharov, and U. Starke, “Quasi-Free-Standing Epitaxial Graphene on SiC Obtained by Hydrogen Intercalation,” *Phys. Rev. Lett.*, vol. 103, no. 24, p. 246804, Dec. 2009.
[100] K. Lee, S. Kim, M. S. Points, T. E. Beechem, T. Ohta, and E. Tutuc, “Magnetotransport Properties of Quasi-Free-Standing Epitaxial Graphene Bilayer on SiC: Evidence for Bernal Stacking,” *Nano Lett.*, vol. 11, no. 9, pp. 3624–3628, Sep. 2011.
[101] J. Hicks, M. Sprinkle, K. Shepperd, F. Wang, A. Tejeda, A. Taleb-Ibrahimi, F. Bertran, P. Le Fèvre, W. A. de Heer, C. Berger, and E. H. Conrad, “Symmetry breaking in commensurate graphene rotational stacking: Comparison of theory and experiment,” *Phys. Rev. B*, vol. 83, no. 20, p. 205403, May 2011.
[102] S. Lee, K. Lee, and Z. Zhong, “Wafer Scale Homogeneous Bilayer Graphene Films by Chemical Vapor Deposition,” *Nano Lett.*, vol. 10, no. 11, pp. 4702–4707, Nov. 2010.
[103] K. Yan, H. Peng, Y. Zhou, H. Li, and Z. Liu, “Formation of Bilayer Bernal Graphene: Layer-by-Layer Epitaxy via Chemical Vapor Deposition,” *Nano Lett.*, vol. 11, no. 3, pp. 1106–1110, Mar. 2011.
[104] Z. Yan, Z. Peng, Z. Sun, J. Yao, Y. Zhu, Z. Liu, P. M. Ajayan, and J. M. Tour, “Growth of Bilayer Graphene on Insulating Substrates,” *ACS Nano*, vol. 5, no. 10, pp. 8187–8192, Oct. 2011.
[105] Z. Luo, T. Yu, J. Shang, Y. Wang, S. Lim, L. Liu, G. G. Gurzadyan, Z. Shen, and J. Lin, “Large-Scale Synthesis of Bi-layer Graphene in Strongly Coupled Stacking Order,” *Adv. Funct. Mater.*, vol. 21, no. 5, pp. 911–917, Mar. 2011.
[106] C. Casiraghi, S. Pisana, K. S. Novoselov, A. K. Geim, and A. C. Ferrari, “Raman fingerprint of charged impurities in graphene,” *Appl. Phys. Lett.*, vol. 91, no. 23, p. 233108, Dec. 2007.
[107] A. C. Ferrari, “Raman spectroscopy of graphene and graphite: Disorder, electron–phonon coupling, doping and nonadiabatic effects,” *Solid State Commun.*, vol. 143, no. 1–2, pp. 47–57, Jul. 2007.
[108] Y. Hao, Y. Wang, L. Wang, Z. Ni, Z. Wang, R. Wang, C. K. Koo, Z. Shen, and J. T. L. Thong, “Probing Layer Number and Stacking Order of Few-Layer Graphene by Raman Spectroscopy,” *Small*, vol. 6, no. 2, pp. 195–200, Jan. 2010.
[109] S. Adam and S. Das Sarma, “Boltzmann transport and residual conductivity in bilayer graphene,” *Phys. Rev. B*, vol. 77, no. 11, p. 115436, Mar. 2008.

[110] J. M. Pereira, F. M. Peeters, and P. Vasilopoulos, “Landau levels and oscillator strength in a biased bilayer of graphene,” *Phys. Rev. B*, vol. 76, no. 11, p. 115419, Sep. 2007.
[111] U. Zeitler, A. J. M. Giesbers, A. McCollam, E. V. Kurganova, H. J. van Elferen, and J. C. Maan, “High-Field Electronic Properties of Graphene,” *J. Low Temp. Phys.*, vol. 159, no. 1–2, pp. 238–244, Jan. 2010.
[112] E. V. Kurganova, A. J. M. Giesbers, R. V. Gorbachev, A. K. Geim, K. S. Novoselov, J. C. Maan, and U. Zeitler, “Quantum Hall activation gaps in bilayer graphene,” *Solid State Commun.*, vol. 150, no. 45–46, pp. 2209–2211, Dec. 2010.
[113] H. Schmidt, T. Lüdtke, P. Barthold, E. McCann, V. I. Fal’ko, and R. J. Haug, “Tunable graphene system with two decoupled monolayers,” *Appl. Phys. Lett.*, vol. 93, no. 17, p. 172108, Oct. 2008.
[114] J. D. Sanchez-Yamagishi, T. Taychatanapat, K. Watanabe, T. Taniguchi, A. Yacoby, and P. Jarillo-Herrero, “Quantum Hall Effect, Screening, and Layer-Polarized Insulating States in Twisted Bilayer Graphene,” *Phys. Rev. Lett.*, vol. 108, no. 7, p. 076601, Feb. 2012.